Numerical and Physical Modelling of Tundish Slag Entrainment in the Steelmaking Process

by:

Arthur Mabentsela

Thesis presented in partial fulfilment

of the requirements for the degree

of

MASTER IN ENGINEERING

(EXTRACTIVE METALLURGICAL ENGINEERING)

in the Faculty of Engineering

at Stellenbosch University

Supervisor

Professor Guven Akdogan

Co-Supervisor

Professor Steven M. Bradshaw

December 2015

Declaration

By submitting this thesis electronically, I declare that the entirety of the work contained therein is my own, original work, that I am the sole author thereof (save to the extent explicitly otherwise stated), that reproduction and publication thereof by Stellenbosch University will not infringe any third party rights and that I have not previously in its entirety or in part submitted it for obtaining any qualification.

02 September 2015

……..

Date

ABSTRACT

Extensive work has been published in the open literature concerning the flow patterns in bare tundishes and tundishes furnished with flow control devices. However, very little work has been published on the entrainment of tundish slag.

The aim of this research was to study (physically and numerically) tundish slag behaviour in a bare tundish and a tundish furnished with a flow control device (FCD). Furthermore, to identify, if any, the mechanisms for tundish slag entrainment in a bare tundish and a tundish fitted with a flow control device and to make recommendations based on the findings of this study.

The physical modelling was done in a 1:2 reduced scale model of an industrial tundish such as was studied by Kumar *et al.* (2008). In the physical model, water was used to model the steel phase while paraffin was used to model tundish slag. The numerical modelling was done in ANSYS Fluent 14.5. The Volume of Fluid (VOF) model was used to model the interface between the two phases (paraffin and water). Turbulence was modelling by making use of the Realizable k- ε model.

Observations made whilst the model was running showed that the steel-slag interface remains immobile even in the FCD case. Furthermore entrained paraffin formed small droplets, approximately 1 mm in diameter. These droplets could be seen in small numbers throughout the tundish.

Results from the physical model showed that in both the bare tundish and tundish with a FCD, areas of high concentrations of entrained slag exist near the inlet region. The entrained slag concentration decreases towards the tundish end walls.

A numerical model that can be used to model tundish slag behaviour was developed using the VOF model with a mesh size of 1.4 mm at a time step of 0.125 s for the bare tundish and a tundish fitted with a FCD. The model predicted similar entrained slag patterns as those of the physical model.

Analysis of flow patterns and velocity magnitudes tangential to the steel-slag interface showed that slag entrainment in both the bare tundish and tundish with a flow control device possibly takes place via two mechanisms. First the slag moves across the steel-slag interface via mass transfer, secondly small velocities tangential to the interface, 3×10^{-3} m/s for the bare tundish and 1.5×10^{-2} m/s for the FCD case, at depth of greater than 10 mm below the interface carry the already “entrained” slag into the bulk steel phase. These tangential flow patterns are dominant in the inlet shroud and are to be found in both the bare tundish and in the tundish with a FCD, hence the high concentration of entrained slag in this region.

OPSOMMING

Baie studies is al in die literatuur publiseer omtrent die vloeipatrone in eenvoudige verdeeltrog en in verdeeltrog met vloei-beheer toestelle (VBT). Min werk is egter al gedoen oor die saamsleep van die metaalskuim in verdeeltrog.

Die doel met hierdie studie is om die fisiese en numeriese gedrag van die metaalskuim in eenvoudige verdeeltrog en in verdeeltrog met VBT te bestudeer en om die meganismes, as hulle wel bestaan, vir die saamsleping van metaalskuim in eenvoudige verdeeltrogs, asook in verdeeltrogs met VBT te identifiseer en om dan aanbevelings te maak.

Die fisiese modellering is met ’n 1:2 skaalmodel van die industriële skottel wat deur Kumar *et al.*(2008) bestudeer is, gedoen. In die fisiese model is water gebruik om die staalfase te modelleer terwyl paraffien gebruik is om die verdeeltrog se metaalskuim te modelleer. Die numeriese modellering is in ANSYS Fluent 14.5 gedoen. Die volume van vloei (VOF) model is gebruik om die twee fases (paraffien and water) te modelleer. Die standaard massa en momentum vergelykings is met die gebruik van die Realizable k- ε model opgelos.

Deur waarneming terwyl die model aan die loop was, is vasgestel dat die staal-metaalskuim koppelvlak immobiel bly selfs in die geval van VTB. Verder het die saamgeleepte paraffien klein druppeltjies van 1 mm gevorm.

Resultate van die fisiese model toon dat daar beide in die geval van die eenvoudige verdeeltrog en die verdeeltrog met VTB areas met hoë konsentrasies by die inlope is, Die saamgesleepte metaalskuim neem naby die skottel se eindwande af.

’n Numeriese model wat gebruik kan word vir die modellering van die metaalskuim gedrag is ontwikkel. Hiervoor is die VOF model met ’n sel grootte van 1.4 mm teen ’n tydstap van 0.125 s vir beide die eenvoudige verdeeltrog en die verdeeltrog met ’n VBT gebruik . Hierdie model het dieselfde saamgesleepte metaalskuim patrone as die fisiese model voorspel.

Ontleding van die vloeipatrone en spoed tangensiaal tot die staal-metaalskuim koppelvlak toon dat die samesleeping van metaalskuim in beide die eenvoudige skottel en die verdeeltrog met VBT op twee maniere plaasvind. Eerstens vloei die metaalskuim deur middel van massa oordrag oor die staal-metaalskuim koppelvlak, dan dra klein bewegende, 3 $x10^{-3}$ m/s vir die eenvoudige verdeeltrog en 1.5 $x10^{-2}$ m/s vir die verdeeltrog met ’n VBT stroompies tangensiaal tot die koppelvlak op ’n diepte van 10 mm onder die koppelvlak die reeds saamgesleepte metaalskuim in die massa staal fase in. Hierdie tangensiale vloeipatrone is in die inloop area in beide die eenvoudige verdeeltrog en die verdeeltrog met die VBT dominant. Daarom is daar ’n hoë konsentrasi saamgesleepte metaalskuim in hierdie oppervlakte.

Table of Contents

1. INTRODUCTION

1.1 Background

In modern steel making, steel is either produced via a basic oxygen furnace (BOF) or an electric arc furnace (EAF). In a BOF, hot metal and scrap are blown with oxygen gas and fluxed with lime to remove carbon, phosphorous, sulphur and silicon. An EAF uses steel scrap and other raw material. The process also includes the use of oxygen gas injection and the addition of lime. The steel melt with dissolved oxygen produced from such furnaces is tapped into a ladle where it is deoxidised with ferroalloys such as Fe-Si, Fe-Si-Mn and/or metallic aluminium. The deoxidation products also known as non-metallic inclusions such as silica, alumina, manganosilicates, aluminosilicates and their composites are removed in the ladle by floatation. After the removal of these non-metallic inclusions, the steel melt is degassed under a vacuum and then transferred via the tundish into the mould of a continuous casting machine (Sahai & Emi 2008).

The tundish serves as the last metallurgical vessel through which steel passes before solidifying in the moulds. It is here in the tundish that the last traces of non-metal inclusions should be removed otherwise the inclusions carry over to the moulds and cause defects in the steel product.

In the tundish, tundish slag is less dense than the melt and thus resides on the top of the melt. The slag provides a sink into which non-metallic inclusions float to and dissolve. The slag also protects the melt from air and heat loss. However, when the slag is entrained into the melt as a result of increased turbulence or shearing at the steel-slag, it can become a source of non-metallic inclusions.

The efficiency of non-metallic inclusion removal via flotation in the tundish strongly depends on the residence time of the steel melt in the tundish. Given enough residence time and slag-directed flow, the inclusions will float to the slag layer where they will dissolve in the tundish slag and thus be removed from the melt. A tundish with a large residence time characterised by large fractions of plug flow, minimal dead volume fractions and high ratios of plug flow over mixed flow results in cleaner steel melt reporting to the continuous caster (Sahai & Ahuja 1986).

Numerous studies on flow patterns in the tundish have been carried out over the years since the introduction of the tundish. These studies were aimed at improving the flow characteristics in the tundish (Chattopadhyay *et al.* 2010, Cloete 2014, Jha *et al.* 2001, Jha *et al.* 2008, Kumar *et al.* 2007, Kumar *et al.* 2008, Mazumdar & Guthri 1999, Sahai & Emi 1996, Sahai & Burval 1992, Tripathi & Ajmani 2011). What has emerged from these studies is the use of flow control devices. These flow control devices are used to increase the melt residence time in the tundish and also provide surface-directed flow so as to assist with

inclusion removal. These devices include dams, weirs, baffles and turbulence inhibitors. It is now generally understood that any tundish without the above mentioned flow control devices suffers from poor inclusion removal as a result of low melt residence time characterised by melt bypassing i.e. melt not spending enough residence time in the tundish (Mazumdar & Guthri 1999).

Due to the opaqueness of the steel melt and the elevated operating temperature (1600 ^{o}C) the above-mentioned studies were carried out using a combination of physical models, otherwise known as cold models, and numerical models. Physical models involve the use of reduced scale water models where water is used to represent the steel melt. Numerical models involve using computational fluid packages to model the melt flow in the tundish. When used together, the physical model can be used to verify numerical model results. Once verified, the numerical model can then be adapted without the need of a physical model. This significantly reduces the costs of exploring new designs and also saves time.

The flow behaviour studies that have led to the use of flow control devices were done using both physical and numerical models. In most of these studies, the researchers were only concerned with the melt phase i.e. how the flow control devices affect the melt residence time. Most researchers opted to use only water in their physical models and in numerical models (Sahai & Emi 2008, Chattopadhyay *et al.* 2010, Cloete 2014, Kumar *et al.* 2008, Mazumdar & Guthri 1999). As a result there is little to no information on how the flow control devices affect the slag layer. This is evident in the lack of mentions of the slag layer entrainment as a result of the use of flow control devices in the review of two decades of work (1979 to 1999) by Mazumdar and Guthri (1999). In a more recent review of two decades of work concerning tundish technology (1989 to 2009) by Chattopadhyay and co-workers commented on the lack of research on how the flow control devices affect the slag phase, they pointed out that there is a lack of both physical and numerical models to predict tundish slag entrainment (Chattopadhyay *et al.* 2010). There is therefore a general lack of understanding on how tundish slag is entrained and how the flow control devices affect the slag layer.

1.2 Purpose of study

Following from the above, the purpose of this study was to numerically and physically investigate the effect of flow control devices on the slag layer.

Thus the objectives of this study are to:

- Use physical modelling to study the behaviour of tundish slag in a bare tundish and in a tundish with a flow control device
- Develop a numerical model which can predict tundish slag behaviour in both a bare tundish and a tundish with a flow control device

- Identify, using the numerical model, a mechanism (or mechanisms) for slag entrainment in a bare tundish and a tundish with a flow control device
- Make recommendations based on the findings

1.3 Scope and limitations

In this study the focus is on the effects of a single flow control device on tundish slag behaviour. Due to the opaque nature of molten steel and high operating temperatures (1600 ^{o}C), experiments involving tundishes are often done using water models. In this study a reduced water scale model based on a design by Kumar *et al.* (2008) was used to model the melt flow. While paraffin was used to model the slag layer while water was used to model the melt flow.

The tundish used in this study was built and scaled by Cloete (2014). He used a scale ratio of 1:2 as opposed to the 1:3 originally used by Kumar *et al.* (2008). In this study, only one type of a turbulence inhibitor was studied, the design of which was also adopted from Kumar *et al.* (2008). Dams and weirs were not investigated.

In the water model and the numerical model, isothermal conditions were assumed. This assumption has generally been used by researchers and has yielded comparable results to those of the actual melt flow (Ahuja & Sahai Y. 1986, Hagemann *et al.* 2013, Hattingh 2009, Jha *et al.* 2001, Jha *et al.* 2008, Kumar *et al.* 2007, Kumar *et al.* 2008, Sahai & Emi 1996, Tripathi & Ajmani 2005). This is despite the results found by Sheng and other workers which showed that natural convection as a result of temperature differences in the tundish plays a significant role in the flow patterns that emerge in the tundish (Sheng *et al.* 1998, Joo & Guthrite 1991). Despite these results this study will follow numerous other researchers in the field and assume isothermal conditions.

The above assumption has an influence on the accuracy of predicting the concentration of entrained slag in the bulk steel phase. In the actual industrial tundish, natural convection caused by temperature differences between the top of the tundish and the bottom, adds more up-ward directed forces on entrained slag droplets thus promoting more surface-directed flow which leads to less entrainment compared to that in the physical model used in this study. Solhed *et al.* (2008) proved this when they studied numerically how adding buoyancy forces in the numerical model affects entrained slag concentration. They found that adding buoyancy forces decreases entrained slag concentration by a factor of ten (Solhed *et al.* 2008). Thus the entrained slag concentrations produced in this study cannot be immediately related to the actual industrial tundish slag entrainment.

However, it can be argued that the purpose with this study is to study the entrained slag behaviour and to develop a numerical model that can replicate the physical model results. Thus there need not in this study be an attempt to accurately model industrial tundish slag entrainment, instead there should be an attempt to sufficiently predict entrained tundish

slag behaviour and to develop a model which can later be fed the most accurate conditions to predict actual tundish slag entrainment.

2. LITERATURE REVIEW

2.1 The purpose of the tundish in steel making process

Steel production has increased significantly over the years, from 512 million tons per annum in 1980 to 1242 million tons in 2013 (World Steel Association 2015). Concurrent with this increase in production levels are stringent quality requirements which have become essential in the face of progressively increasing machine throughputs and larger production (Sahai & Emi 2008).

Steel produced in a furnace was initially cast directly into a mould by two methods; from the bottom of the mould, known as bottom pouring, or from the top of the mould, known as top pouring. With the top pouring method, the melt was exposed to air, and hence suffered from the oxidation of the dissolved deoxidising agent. The products of this reaction cause surface defects in the steel.

In bottom pouring, the melt stream is exposed to bare mould refractory which through refractory erosion can lead to mould defects due to refractory particles.

With the introduction of continuous casting, exposure of the steel melt to air and mould refractory wear was decreased and thus an increase in the yield of premium cast steel was realised by steelmakers (Sahai & Emi 2008).

The tundish was initially regarded as nothing more than a reservoir to hold sufficient melt to provide a constant head over the mould of a continuous caster and to allow for ladle changes to occur without interruptions to the continuous casting process (Schade *et al.* 2003). It is now generally known that the tundish plays a more important role in the production of clean steel. As a result of substantial research, the role of a tundish is now generally accepted to (Johannes *et al.*, 2003, Kumar *et al.*, 2008 and Sahai *et al.*, 2008):

- Promote non-metallic inclusion flotation by maximising melt residence time in the tundish;
- Prevent thermal and chemical losses from the melt;
- Eliminate contamination of the melt via air, refractory and slag entrainment;
- Provide a homogeneous melt to all casting moulds and thus yield a similar steel product for a number of heats.

2.2 Non-metallic inclusion in tundishes

Non-metallic inclusions are impurity elements and compounds found in the steel melt. Non-metallic inclusions include metal oxides, sulphides, nitrides, carbines and their compounds. The presence of non-metallic inclusions in cast steel can have detrimental effects on the quality of the steel, thus non-metallic inclusions should be prevented from being carried over into the steel mould of a continuous casting machine.

Sulphide inclusions can be minimised by ladle refining of the steel melt by desulfurising the melt prior to melt transfer to the tundish. Thus these types of inclusions are not significant in tundish operations. Oxide inclusions on the other hand arise in the ladle, tundish and during transfer of the melt to the mould via the tundish (Sahai & Emi 2008).

Oxide inclusions can either originate in the steel melt (indigenous inclusions) or externally (exogenous inclusions).

2.2.1 Indigenous inclusions

Indigenous inclusions have their origins in the de-oxidation reaction which takes place in the ladle via reaction 2-1

$$n[M] + m[O] \rightarrow M_n O_m \qquad 2\text{-}1$$

Where [M] is the deoxidising element such as Mn, Si or Al added to the ladle melt to lower the oxygen content of the melt, and M_nO_m is the inclusion, otherwise known as the de-oxidation product (Sahai & Emi 2008).

Although most of the de-oxidation products are removed during the ladle refining process, some small products do remain in the melt and are carried over into the tundish.

Indigenous inclusions can be as large as 100-200 µm after their formation and when agglomeration and growth are in progress. After subsequent intense stirring during ladle refining, their size can be reduced to 20 µm (Zhang & Thomas 2003a, Sahai & Emi 2008). Thus indigenous inclusions found in the tundish are smaller than 20 µm if no agglomeration and growth takes place during transfer.

Depending on the type of deoxidising agent used, the inclusions display different shapes. When aluminium is used as a deoxidising element (Al-killed steel), the alumina inclusions formed are dendritic when formed in high oxygen concentration environments, while silica inclusions, in silicon killed steel, are generally spherical (Zhang & Thomas 2003a).

In their agglomerated form, alumina inclusions show different structures of fractal characteristics (Luo-fang *et al.* 2013).

2.2.2 Exogenous inclusions

This type of inclusion can form via (Sahai & Emi 2008, Zhang & Thomas 2003b):

- Reoxidation of deoxidised steel melt by ingress air from joints either in the ladle, ladle nozzle, or in the tundish nozzles;
- Reoxidation of the melt bath surface in the tundish by ingress air;
- Reoxidation of melt bath surface by iron oxide, manganese oxide and or silica that are contained in the carry over slag from the ladle, or flux added to the tundish;
- Entrainment of ladle slag as a result of vortexing or drainage of ladle to near empty level;
- Emulsification and entrainment of tundish slag floating on the melt surface by turbulence caused by teeming stream from the ladle during the opening and changing of the ladle;
- Entrainment of tundish slag floating on the melt surface by turbulence flow near the steel-slag interface or by vortexes which can form above the tundish strands when the tundish is operated at low bath levels;
- Reoxidation of the melt at the melt/refractory interface by less stable oxides contained in tundish glaze, the nozzle, and/or the tundish lining;
- Entrainment of the fragments of the ladle glaze, ladle nozzle, long nozzle, tundish lining, and/or submerged entry nozzle due to erosion and detachment by turbulent melt flow

Exogenous inclusions are usually large in size, greater than 50 µm and have complex structures. They also have a complex chemistry due to their numerous sources of origin; often they include components from reoxidised melt, ladle slag, tundish flux, mould flux and refractory components (Zhang & Thomas 2003a, Sahai & Emi 2008).

2.2.3 Effect of inclusions on steel properties and operations

Steel as a structural material, has advantageous properties such as strength, ductility and durability. Ductility includes deep drawability, cold formability and low temperature toughness. Durability refers to resistance against wear, fatigue, hydrogen-induced cracking and stress corrosion cracking. The ductility and durability are significantly impaired by large non-metallic inclusions in steel (Sahai & Emi 2008).

Steel with large sized non-metallic inclusions is termed ‘’dirty steel’’ and is not fit for use. Only steel with small sized uniformly concentrated inclusions may be termed as ‘’clean’’ steel and is suitable for use. The critical inclusion size allowable in the steel product varies from one product to another. Table 2-1 below shows the critical inclusion size in various steel products.

Defects caused by non-metallic inclusions include (Zhang & Thomas 2003a):

- Lack of formability in Low Carbon Alumina Killed (LCAK) steel;
- Reduced life span of bearings and axles;
- Cosmetic defects such as slag spots on cold rolled steel and line defects known as slivers in cold rolled sheet

As mentioned, steel with large inclusions is not suitable for use and is thus discarded. This lowers the premium product yield of the steel maker and has financial implications.

Apart from financial implications, inclusions also cause operation difficulties such as clogging of nozzles due to agglomerated alumina inclusions. In the worst cases this can lead to process downtime. The clogged piece of alumina can also be dislodged by turbulence caused by the melt stream. This can cause surface defects in the cast steel mould.

Table 2-1 Critical Inclusion Size for various Steel Products (Zhang & Thomas 2003a)

Steel Product	Maximum Inclusion Size
Automotive and deep-drawing sheet	100 µm
Drawn and Ironed cans	20 µm
Line pipe	100 µm
Ball bearings	15 µm
Tie cord	10 µm
Heavy plate steel	Single inclusion 13 µm
	Cluster of inclusions 200 µm
Wire	20 µm

2.3 Tundish design and mechanism for inclusion removal

2.3.1 Typical tundish design

Figure 2-1 below shows a typical industrial tundish. Tundishes often have a rectangular cross sectional area with inclined side walls. The rectangular cross sectional areas and inclined walls help with effective mixing of the melt and promote longer melt residence time for inclusion removal (He & Sahai 1987). Other shapes include H-shape, T-shape. A tundish can have numerous strands, but typically tundishes have anywhere from one to six strands. The number of strands a tundish has is influenced by production demands, with more strands giving higher throughputs. More explanations on tundish parts can be seen in the list below.

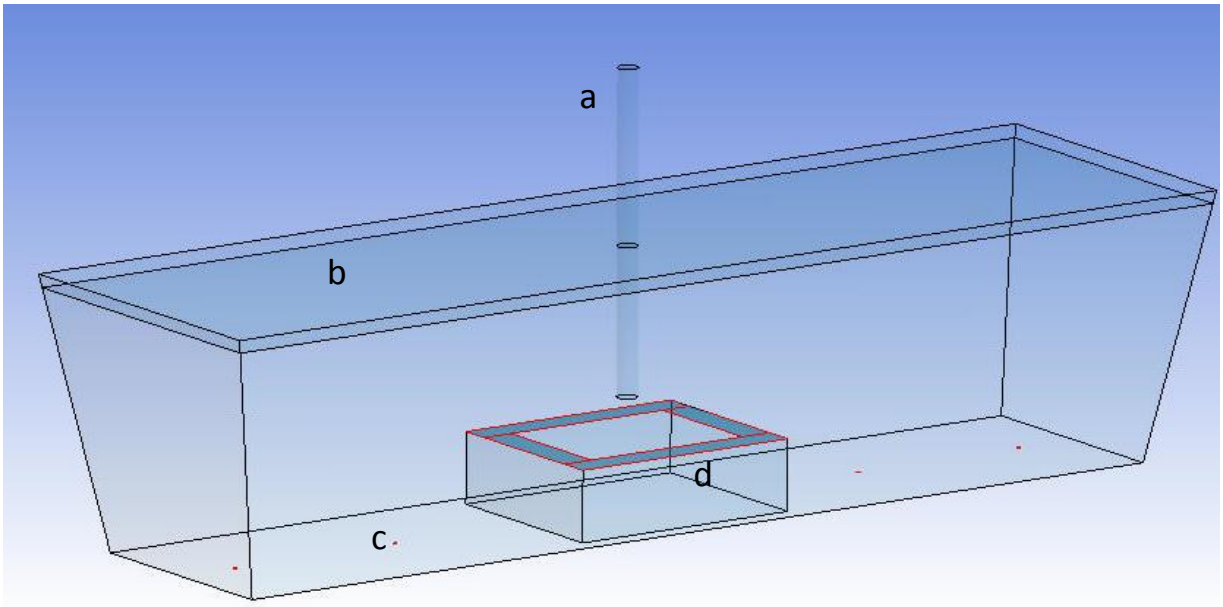

Figure 2-1 Typical tundish with flow control devices

a) Inlet shroud - Feeds molten steel into tundish without exposing it to air
b) Slag layer - Protects the bath from air, insulation and inclusion sink
c) Strand - Outlet to the casting machine
d) FCD - Prevents melt short-circuiting/absorbs teeming turbulence

2.3.2 Mechanisms for inclusion removal

Inclusions can move out of the tundish by three methods; flotation, attachment to refractory and by bypassing. The last-mentioned method is not ideal as it leads to inclusion being carried over to the mould.

Flotation

Flotation is the main mechanism for inclusion removal in the tundish. Inclusions are less dense than the steel melt and thus rise up by Stokes' flotation assisted by the upward flow of the melt, to dissolve in the slag layer.

Larger inclusions (>50 µm) float better than smaller sized inclusions (20-50 µm). In some operations, argon bubbling at the bottom of the tundish is used to aid the flotation of inclusions (Sahai & Emi 2008).

Attachment to tundish refractory

Inclusions can also move out of the melt by attaching themselves to the tundish refractory. This is due to the fact that inclusions are not wetted by the melt and thus there is a high contact angle between the inclusion particle and the melt. The high contact angle encourages alumina inclusions in the melt to attach themselves to the refractory wall to avoid contact with the steel (Zhang & Thomas 2003a). This method of removal is not ideal as it leads to a decrease in tundish volume due to tundish wall growth.

Bypassing

Inclusion bypassing is defined as inclusions flowing out of the tundish with the melt to the continuous casting mould. Inclusion bypassing is the result of the inclusion not having enough residence time in the tundish to float to the slag layer. Bypassing is caused by unfavourable flow patterns in the tundish characterised by low melt residence time in the tundish as a result of high mixing volume fractions, high dead volumes in the tundish and non-slag directed flow.

To improve flow patterns in the tundish, the tundish can be furnished with flow control devices such as dams, weirs, impact pads, turbulence inhibitors etc. The purpose of these devices is to promote increased melt residence time in the tundish by minimising fraction of dead volumes, increasing plug flow volume fractions and minimising mixing volume fractions in the tundish. These devices also assist with surface directed flow so as to promote the inclusion to dissolve in the slag layer (Kumar *et al.* 2008).

2.4 Tundish Slag

2.4.1 The role of tundish slag in tundish performance

Tundish slag comes from the tundish cover powder otherwise known as tundish flux. The function of tundish slag is to insulate the molten bath from heat loss, protect the melt from chemical changes and to absorb inclusions for additional refining (Tapia *et al.* 1996).

Factors which govern slag performance include viscosity, melting point, interfacial tension, and inclusion solubility (Sahai & Emi 2008). The exact values of these vary depending on the components of the tundish slag.

Viscosity

High viscosity slag is slow to absorb inclusions, while high fluid slag is easily entrained by the melt.

Melting point

The melting point of the slag should be such that the slag in contact with the melt is in a molten state for inclusion absorption, while the flux on the top of the slag should stay in a solid state for thermal insulation.

Interfacial tension

Low interfacial tension between the slag and molten bath leads to easy entrainment of the tundish slag. On the other hand slag, which has a high interfacial tension with the melt, does not readily dissolve inclusions.

2.4.2 Mechanisms for tundish slag entrainment

Slag entrainment is the formation of slag droplets in the steel melt. Entrainment of tundish slag into the steel melt can occur via vortexing, high velocity flow that shears the slag at the slag-steel interface and turbulence at the slag-steel interface (Hagemann *et al.* 2013).

Apart from high velocities at the interface, some authors have reported slag emulsification in slow steel melt velocity zones. This mechanism is thought to be caused by the Kelvin-Helmholtz Instability which arises when two streams of fluid with different densities flow past one another. The presence of shear stress leads to instability, which causes the growth of waves which later roll into small vortices (Solhed & Jonsson 2003).

Slag entrainment can also occur as a result of Marangoni flow or by mass transfer across the interface. In Marangoni flow, the slag movement into the steel phase and vice versa is caused by local gradients of the interfacial tension caused by chemical reactions (Hagemann *et al.* 2013) while in the mass transfer method, slag and steel move across the interface due to low concentrations of the two fluids across the interface. Critical entrainment values pertaining to this study are evaluated in Table 2-11.

Vortexing

Nagaoka and co-workers studied the effect of bath level on slag entrainment via vortex formation. They concluded that vortexing occurs during melt transfer to the mould when the bath level inside the tundish is low (Nagaoka *et al.* 1986).

Vortexing can therefore be controlled by controlling the bath level in the tundish. It is well-known in the steel making industries that melt transfer during low bath level causes vortex formation which leads to slag carrying over to the mould.

Slag shearing at the steel-slag interface

Entrainment of a lighter phase into a heavy phase starts with finger like protrusions of the lighter phase into the heavy phase. This fingering phenomenon can be described by the Taylor-Saffman Instability that occurs when a fluid of unequal density and viscosity relative to the second fluid pushes down on the second fluid. (Feldbauer & Cramb 1995) studied the entrainment of slag in the casting mould using Taylor-Saffman Instability. They commented that the instability depended upon interfacial tension, viscosity, and inertial energy exerted by the heavier phase. The actual entrainment at the tip of a lighter phase protrusion inside a heavier phase is a function of the deforming stress exerted by the heavier phase and the counteracting interfacial tension between both phases (Hagemann *et al.* 2013).

The entrainment of the lighter phase into the heavier phase was further studied in a couette device and four rollers, where the density ratio of the two fluids was 1 (ρ_{heavy} /$\rho_{lighter}$). The detachment of the lighter fluid into the heavier fluid was found to be a function of the viscosity ratios of the fluids used ($\eta_{heavy}/\eta_{lighter}$) and the dimensionless critical number, known as the critical capillary number (Hagemann *et al.* 2013).

Hagemann et al. (2013) furthered this research by studying the effect of the kinematic viscosity ratio of the two fluids ($\nu_{lighter}/\nu_{heavy}$) on the critical capillary number (Ca*). They used a water model with a rotating roller to generate shear stress at the interface. Different silicon oils were used to represent the slag layer.

In their studies the following definitions applied:

$$Ca = \frac{V_2 \eta_2}{\sigma} \quad 2\text{-}2$$

$$Ca^* = f\left(\frac{\nu_1}{\nu_2}\right) \quad 2\text{-}3$$

where:

V_2 - Tangential velocity of the heavier phase below the interface

η_2 - Molecular viscosity of the heavier phase

σ - Interfacial tension between the two phases

ν_1 - Kinematic viscosity of the lighter phase

ν_2 - Kinematic viscosity of the heavier phase

In their findings, Hagerman *et al.* (2013) showed that the critical capillary number for slag entrainment is a function of the ratios of kinematic viscosities given by:

$$Ca^* = 3 \times 10^{-6}\left(\frac{\nu_1}{\nu_2}\right) + 2.8 \times 10^{-3} \quad 2\text{-}4$$

According to the above equation, raising the ratio of kinematic viscosities of a system should raise the critical capillary number and thus reduce the chances of entrainment. If the capillary number of the system, calculated with eq. 2-2 is below the critical capillary number of that particular system, then no entrainment of slag will occur.

Hagemann *et al.* (2013) and co-workers also went on to study the effect of the slag layer thickness on the critical capillary number needed for slag entrainment to occur. They found that the slag layer thickness has no effect on the entrainment of slag resulting from shear stress at the interface.

A recent numerical study done by Solhed *et al.* (2008) showed that the slag entrainment in a one-strand bare tundish was caused by shearing at the interface. They commented that shearing was caused by a recirculating flow in the inlet region. They also showed that the highest entrained slag concentration was in the region behind the inlet. It is nevertheless worth mentioning that Solhed *et al*. (2008) did not do any mathematical investigation to establish which of the mechanisms identified above are responsible for slag entrainment, moreover, they did not do any studies on FCD and their effect on slag entrainment.

Harman and Cramb (1996) studied the size of the entrained slag droplets formed via shearing of the slag layer, using a water model. They noted that the size of the first entrained slag droplet is the largest. They noted that the size of this droplet can be estimated by eq. 2-5.

$$D = 0.534\left[\frac{\sigma^{0.639}}{g^{0.564}(\rho_2-\rho_1)^{0.130}\rho_2{}^{0.306}}\right]\frac{\mu_1{}^{0.114}}{\mu_2{}^{0.372}} \qquad 2\text{-}5$$

Hagemann and co-workers also studied the size of entrained "slag" droplets via shearing at the interface using clod models. They found that their estimated droplet sizes were of the same order of magnitude as those of Harman and Cramb (1996) (Hagemann *et al.* 2013).

However it was rather strange that they attempted to study the entrained droplet size with respect to changes in the kinematic ratio of the two fluids, when the empirical equation given by Harman and Cramb clearly shows that the relationship between the droplet size and the viscosity ratios of the two fluids used is not linear and that it varies independently of each viscosity ratio.

Kelvin-Helmholtz Instability

This method of entrainment arises when two inviscid, irrotational fluids of different densities separated by a flat interface move at different tangential velocities (Hibbeler & Thomas 2010). The instability and entrainment of slag takes place when the difference between the two fluids exceeds a critical velocity which is given by:

$$\Delta V_{crit} = \sqrt{\left[\frac{1}{\rho_2}+\frac{1}{\rho_1}\right]\left[\frac{g}{k}(\rho_2-\rho_1)+k\sigma\right]} \qquad 2\text{-}6$$

where:

ΔV_{crit} - Critical tangential velocity difference between steel and the slag

ρ_2 - Density of steel

ρ_1 - Density of the slag

g - Gravitational acceleration

σ - Interfacial tension between steel and slag

k - Angular wave number of small perturbation on the interface with wavelength λ.

$$k = \frac{2\pi}{\lambda} \qquad 2\text{-}7$$

The minimum wavelength at which Kelvin-Helmholtz instability takes place in nature is given by:

$$\lambda = 2\pi\sqrt{\frac{\sigma}{g(\rho_2-\rho_1)}} \qquad 2\text{-}8$$

This gives rise to the minimal critical velocity at which Kelvin-Helmholtz instability takes place which is given by:

$$\Delta V_{crit} = \sqrt[4]{4g(\rho_2-\rho_1)\sigma\left[\frac{1}{\rho_2}+\frac{1}{\rho_1}\right]^2} \qquad 2\text{-}9$$

Milne-Thomson (1968) extended Kelvin-Helmholtz instability to include finite fluid depth but neglected the effect of viscosity and interfacial tension, yielding:

$$\Delta V_{crit} = \sqrt{g(\rho_2-\rho_1)\left(\frac{H_2}{\rho_2}+\frac{H_1}{\rho_1}\right)} \qquad 2\text{-}10$$

Where H_1 and H_2 are the thickness of the slag layer and the steel melt layer respectively. Iguchi and co-workers confirmed this using physical experiments which involved a rotating roller under water and oils. They found that the above equation is valid for low viscosity and low frequency disturbances where surface tension is not important or can be neglected (Iguchi *et al.* 2000).

Turbulence at the steel-slag interface

Turbulence at the steel-slag interface is caused by excessive surface directed flow of the melt to the slag layer as a result of the flow reflecting back from the bottom of the tundish or as a result of the improper use of flow control devices.

Too much surface directed flow does not only lead to slag entrainment but also to balding of the slag layer. In the latter case, the surface directed flow is so high that it pushes the slag away and causes the melt to be exposed to air (Hibbeler & Thomas 2010).

Marangoni flow

Exchange reactions, such as the oxidation of dissolved aluminium, which take place at the interface, reduce the local interfacial tension between steel and slag and thus increase the system's capillary number. If the system's capillary number is increased past its critical capillary number, then emulsification can occur even at low melt velocities.

Similar to the exchange reactions at interface, bubbling of argon from the bottom of the tundish decreases the local interfacial tension between steel and the melt thus leading to slag entrainment even at low melt velocities.

Gas bubbling

Gas bubbling is often used in tundishes to promote inclusion flotation. The gas of choice is argon due to its inertness. The injected gas may however lead to slag entrainment when the gas bubbles rapture at the upper slag layer.

The bubbles rise up due to buoyancy, they penetrate the slag layer and once they reach the surface of the slag layer, they rupture, causing small slag droplets to enter the steel phase (Hibbeler & Thomas 2010).

Mass transfer at the interface

Although not well documented as a mechanism for slag entrainment, mass transfer across the steel-slag interface could possibly lead to low concentrations of slag in the steel phase and low steel concentration is the slag phase. In a summary of model studies on slag entrainment methods in gas stirred ladles, Senguttuvan and Irons (2013) comment that entrainment of slag/steel across the steel-slag interface increases the mass transfer rate substantially across the interface. They also go on to comment that identification or characterisation of entrainment has been limited to finding the conditions for entrainment and that quantifying the amount of entrainment has been neglected. Although not explicitly stated by Senguttuvan and Irons (2013) it is easy to imagine how a combination of mass transfer across the interface and relatively small shearing flow patterns can lead to entrainment of slag.

Solhed and Jonsson numerically studied slag entrainment in a real sized industrial tundish at its operation temperature. In their findings they questioned the existence of slag in the steel phase at 3 mm below the interface despite the low tangential velocities; 7×10^{-2} m/s. The two authors speculated about the cause of the existence of this slag in such a system (Solhed & Jonsson 2003). Mass transfer could be the method that caused slag "entrainment" in their study.

2.5 Flow Characterisation Theory

A flow characterisation study is a key starting point when it comes to understanding a reactor or any metallurgical vessel or optimising its performance. Typically in such studies, a tracer (salt, dye or acid) is injected in the inlet stream of the vessel. Its concentration is then monitored at the outlet of the vessel as a function of time. A plot of the tracer concentration at the outlet ports against time is known as the residence time distribution (RTD) curve. The RTD of the vessel can then be analysed to gain knowledge of the flow patterns inside the vessel. Such an analysis involves calculating plug flow volume fraction, dead volume fraction and mixing volume fractions.

In a vessel where the maximum residence time of the fluid is required, the RTD of such a vessel needs to exhibit large plug flow volume fractions as opposed to mixing volume fractions and minimal dead volume fractions. In a vessel where mixing is the main object,

the RTD needs to show high mixing volume fractions whilst still maintaining low dead volume fractions.

2.5.1 Ideal flow patterns

Plug flow

In an ideal plug flow vessel, each fluid element moves as a unit, there is no longitudinal mixing. All the fluid elements in a plug flow vessel have an equal residence time (τ_p). A typical RTD response of a plug flow reactor is shown by Figure 2-2.

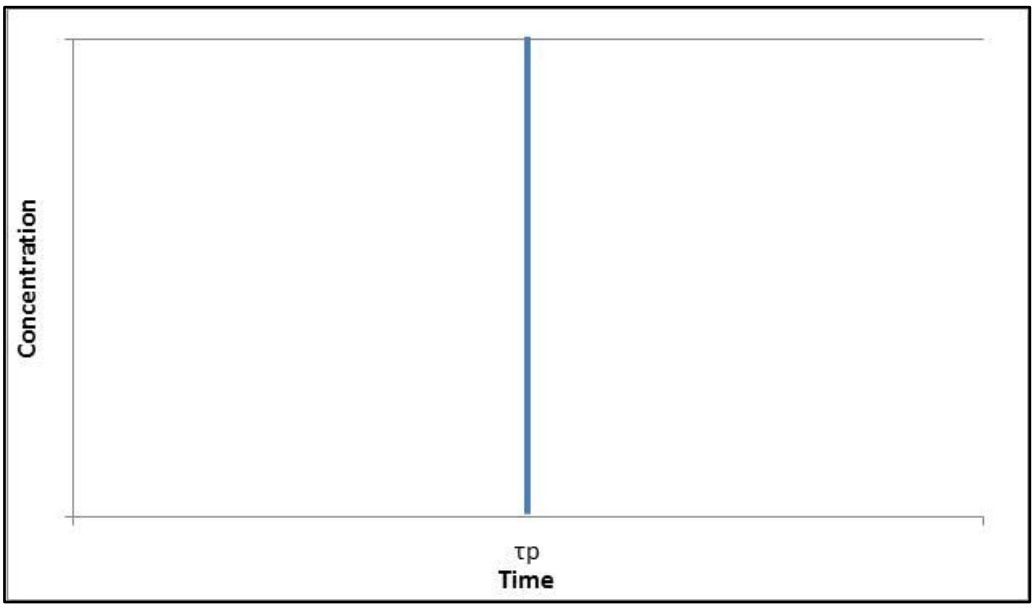

Figure 2-2 Typical RTD of plug flow reactor or vessel

Mixed flow

In a mixed flow vessel, there is maximum mixing both longitudinally and transversely. Because of the high degree of mixing in a mixed flow vessel, a fluid element entering a mixed flow reactor can spend anywhere between zero time to infinity time in the vessel. The typical RTD response of a mixed flow vessel is depicted in Figure 2-3

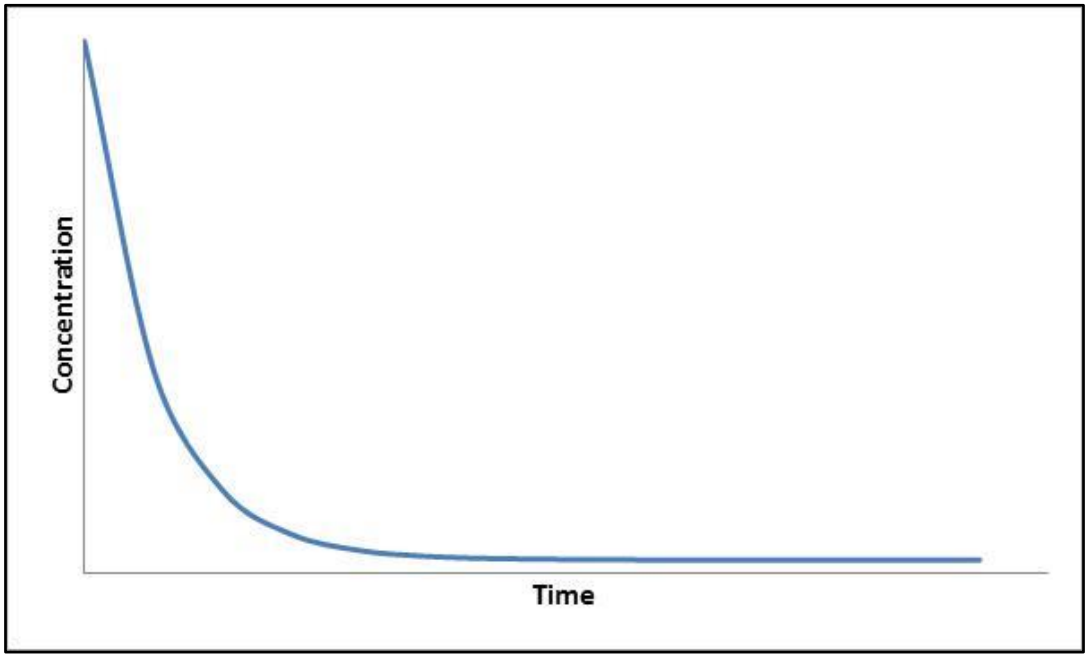

Figure 2-3 Typical RTD response of a mixed flow reactor or vessel

2.5.2 Non-ideal flow patterns

In reality flow patterns in any vessel exhibit characteristics of both mixed and plug flow patterns. In most vessels, flow can be classified as dispersed plug flow or combined flow.

Dispersed plug flow

In reality, plug flow vessels exhibit some degree of longitudinal mixing. When this happens, a fluid element is spread both longitudinally and radially or transversely. As a result of this not all fluid elements spend exactly the same time in the vessel. Longitudinal mixing in a plug vessel can be caused by turbulence in the vessel or friction at the vessel walls. The extent of longitudinal mixing in a plug flow reactor or vessel is termed dispersion, De. De is zero for an ideal plug flow and infinity for a well-mixed flow. The typical RTD of a dispersed plug flow vessel is shown in Figure 2-4.

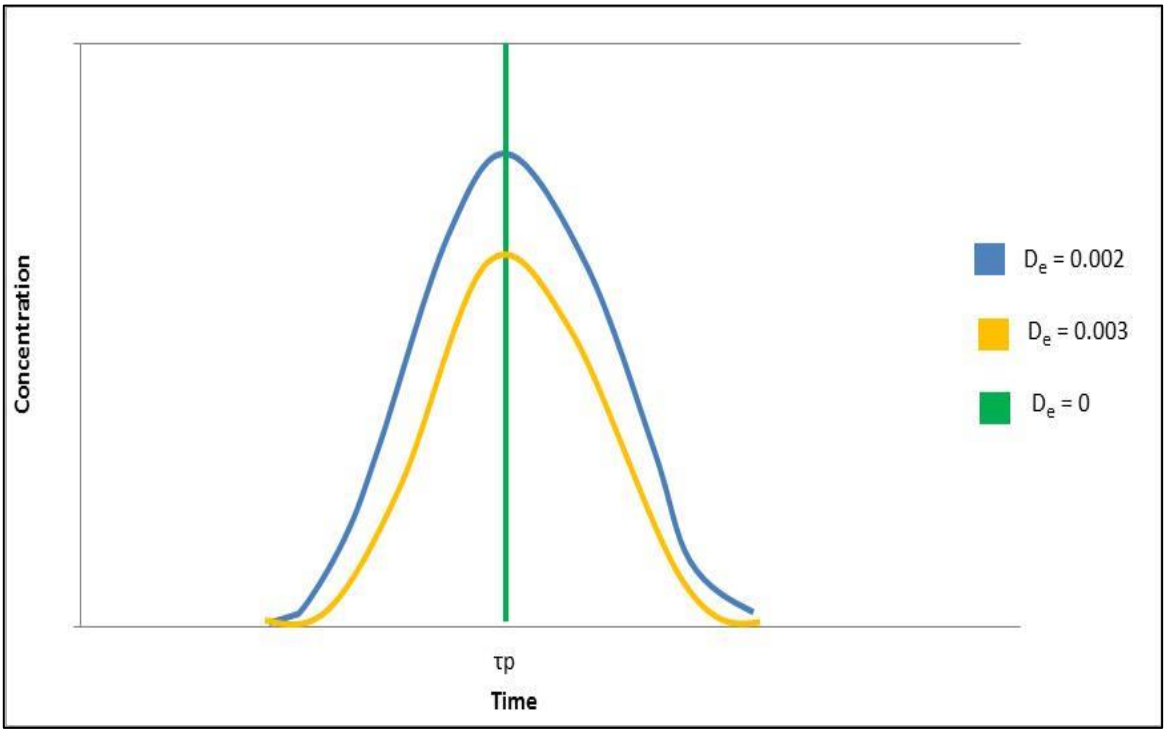

Figure 2-4 RTD of a dispersed plug flow reactor or vessel

Combined flow

In a combined flow, the vessel is segmented into plug flow volume, mixed flow volume and a dead volume.

The plug flow in a mixed model flow regime can be either ideal or dispersed. Figure 2-5 and 4-6 show the RTD response of the two situations respectively.

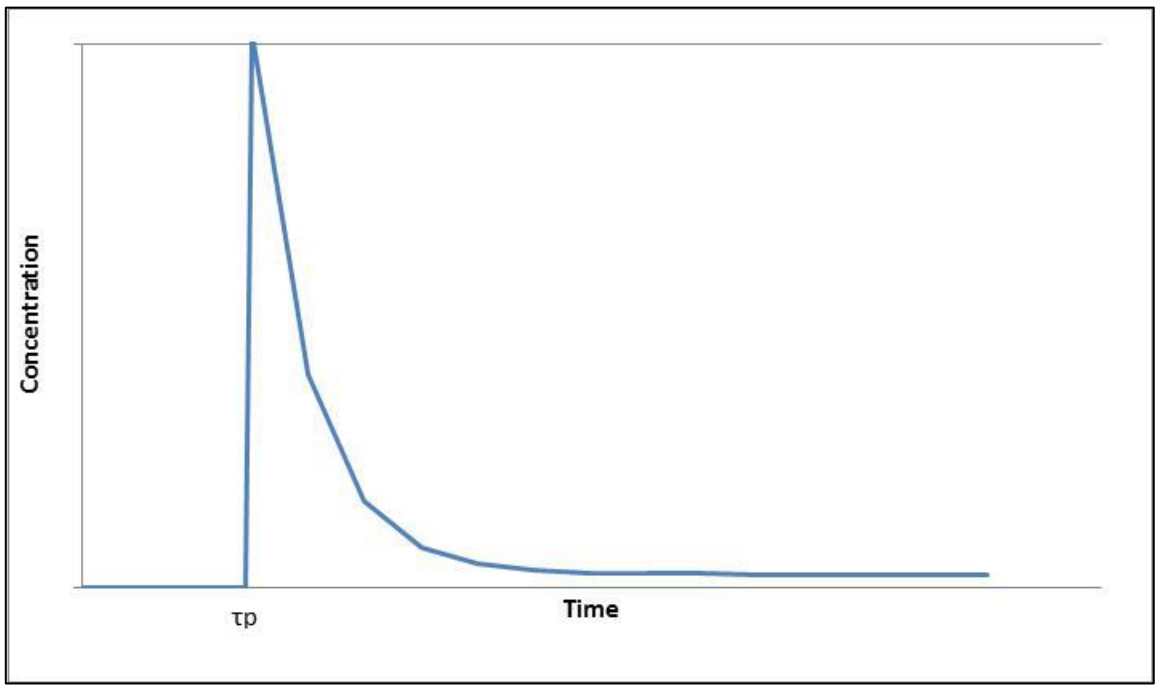

Figure 2-5 Mixed model RTD with ideal plug flow

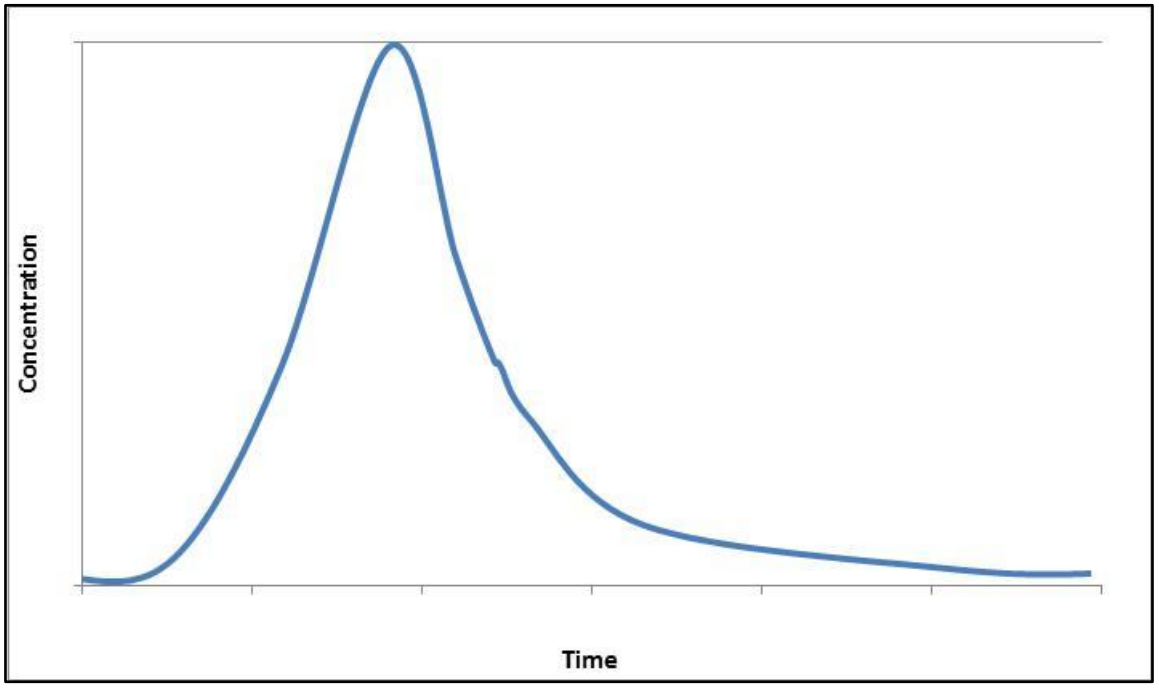

Figure 2-6 Mixed model RTD with dispersed plug flow

Dead volume in a combined flow model can either be stagnant, or slow moving. In a stagnant dead volume, no flow enters or leaves that fraction of the vessel whilst in a slow moving dead volume a portion of the flow enters the dead volume and slowly exits it. A vessel with slow moving dead volumes can be identified by the long tail in the RTD of that vessel, whilst the one with stagnant dead volumes does not have such a tail.

2.5.3 Combined model for tundish use

Most tundishes exhibit flow patterns with the characteristics of the combined flow model. The plug flow fraction is that of a dispersed plug flow and the dead volumes are often slow moving as opposed to being stagnant (Sahai & Emi 1996).

At this stage the following concepts should be introduced:

τ_m - Theoretical residence time given by the ratio of the flow rate into the vessel and the volume of the vessel

C - Dimensionless concentration given by the ratio of concentration of the tracer at the outlet and the concentration of the tracer initially present in the entire vessel

θ - Dimensionless time given by ratio of the flow time at which the concentration of the tracer at the exit is recorded and the mean residence of the vessel

$\bar{\theta}_c$ - Dimensionless mean residence time up to a certain cut off value

With the above definitions, the RTD plot can be changed to become a plot of dimensionless concentration against dimensionless time. In this form, comparison between RTDs from different vessels can be drawn.

Calculating mixing volume fraction

The fraction of volume which shows mixing flow patterns can be calculated by using the inverse of the maximum dimensionless concentration.

Calculating plug flow volume fraction

The plug flow volume fraction can be read off the dimensionless residence time distribution curve as the dimensionless time at which the first sign of the tracer can be seen at the outlets (θ_{min}). This idea holds true for ideal plug flow vessels in series with ideal well mixed vessels, but in reality, as pointed out in Figure 2-6, the plug flow is dispersed, thus there is a minimum time for the tracer to show at the outlet, followed by a time when the peak concentration of the tracer is seen or read at the outlets (θ_{peak}). To solve the problem of calculating the volume of plug flow in dispersed plug flow, Ahuja and Sahai suggested that the average between θ_{min} and θ_{peak} be used to calculate the volume fraction of plug flow (Ahuja & Sahai Y. 1986). This approach will be followed in this study.

Calculating dead volume fraction

In the combined model with slow moving dead volumes, the volume fraction of the vessel which is slow moving dead volumes can be calculated by eq. 2-11 (Sahai & Emi 1996).

$$\frac{V_d}{V} = 1 - \frac{Q_a}{Q}\bar{\theta}_c \qquad 2\text{-}11$$

where

$\frac{Q_a}{Q}$ - The fraction of flow that enters the tundish and goes through the active region of the tundish given by eq. 2-12

$$\frac{Q_a}{Q} = \sum_{i=0}^{2} C_i \Delta\theta \qquad 2\text{-}12$$

$\bar{\theta}_c$ - Dimensionless mean residence time up to 2 given by

$$\bar{\theta_c} = \frac{\sum_{i=0}^{2} C_i \theta_i}{\sum_{i=0}^{2} C_i} \qquad 2\text{-}13$$

It is worth mentioning here that in the above equations, it has been assumed that any tracer exiting the tundish after θ=2 is considered to be as a result of slow moving volumes, hence the cut off point for any analysis is 2 (Mazumdar & Guthri 1999). Furthermore, the above equations only work if the concentration readings of the tracer in the exit stream are taken at equal intervals.

In this study a mix of slow moving dead volumes (in the bulk fluid) and stagnant dead volume fractions (paraffin phase) will be experienced. Thus it is not clear whether the above approach is suitable for this study. Instead of calculating the dead volume fractions by using

eq. 2-11, the idea that the dead volume fraction, plug flow volume fraction and mixed flow volume fraction should be a unity will be used.

2.6 Modelling Theory

Due to the high operating temperatures in the steel making factory and the opaqueness of the steel melt, it is difficult to conduct experiments or to gain visual images from an actual industry tundish.

Modelling allows researchers to conduct experiments that are at times impossible or too expensive to accomplish in the steel-making environment. Modelling can be split into two classes; physical modelling and numerical modelling.

2.6.1 Physical modelling theory

Physical models make use of scaled down models or equally sized models of the tundish vessel. Water is used to study and simulate the steel melt flow, while paraffin or silicon oils are used to simulate the slag layer.

Depending on the similarity criteria being fully satisfied, results from a physical model can accurately predict the performance of an actual industrial tundish.

Criteria for physical modelling

Geometrical similarities

Physical models can be full scale where all the dimensions of the model are the same as the prototype, or reduced scale where the dimensions of the prototype are reduced by a factor, λ, given by eq. 2-14. The choice between a full-scale model and a reduced scale model is the researcher's choice. Reduced models are usually used in the laboratories where space and finance are factors, while full scale models are used in industry.

$$\lambda = \frac{L_m}{L_P} \qquad 2\text{-}14$$

To satisfy the geometrical similarity criteria, all dimensions of the prototype must be reduced by λ and all angles in the model must be the same as in the prototype.

Dynamic similarities

Dynamic similarities are concerned with the forces that act on a fluid element. It is necessary that the ratios of the corresponding forces between the model and the prototype be identical for the model to give useful results. Two force ratios are considered when modelling tundish flow patterns; Reynolds Number (N_{Re}) and Froude Number (N_{Fr}). This is mathematically given by eq. 2-15 and eq. 2-16 respectively (Mazumdar & Guthri 1999). In these equations subscripts m and p are the model and prototype respectively.

$$N_{Re,m} = N_{Re,p} \quad 2\text{-}15$$

$$N_{Fr,m} = N_{Fr,p} \quad 2\text{-}16$$

Research by Sahai and Burval shows that in turbulent regimes such as in the tundish, the magnitude of the Reynolds Number, irrespective of geometry or size, is very similar. Therefore Reynold similarities are naturally satisfied as long as the model is operated in a turbulent regime (Sahai & Burval 1992).

Following from the above, the only dynamic similarity that should be taken into account when modelling melt flow is the Froude similarity.

Froude similarity is achieved if eq. 2-17 is satisfied. From eq. 2-17, a number of scale factors for different properties can be formulated for the model to remain dynamically similar to the prototype. Table 2-2 shows such scale factors.

$$\frac{{V_m}^2}{gL_m} = \frac{V_p^2}{gL_p} \quad 2\text{-}17$$

where:

V_m - Velocity of fluid or inclusion in the model

V_p - Velocity of fluid or inclusion in the prototype

g - Gravitational acceleration

L_m - Any form of length in the model

L_p - Any form of length in the prototype

Table 2-2 Froude Scaling Table

Property	**Scale factor**
Velocity (V)	$\sqrt{\lambda}$
Time (t)	$\sqrt{\lambda}$
Volumetric flow (Q)	$\lambda^{2.5}$
Area (A)	λ^2

Water is the fluid of choice to model the steel phase. This is primarily due to the fact that water at 20 ^{o}C has a similar kinematic viscosity to that of steel at 1600 ^{o}C (Mazumdar & Guthri 1999).

Table 2-3 below shows the properties of water and steel. As can be seen, the kinematic viscosity of steel is 91.3 % of the kinematic viscosity of water.

Table 2-3 Properties of water and steel (Mazumdar & Guthri 1999)

Property	**Water**	**Steel**
Molecular viscosity (kg/m.s)	0.001	0.0064
Density (kg/m^3)	1000.	7014.
Kinematic viscosity (m^2/s)	1.00 x10^{-6}	0.913 x 10^{-6}
Surface tension (N/m)	0.073	1.60

To simulate the slag layer, a variety of fluids are used, ranging from modified silicon oils, benzene, paraffin or kerosene (Chattopadhyay *et al.* 2010, Hagemann *et al.* 2013).

However, Krishnapisharody and Irons recommend the use of paraffin oils for modelling tundish slag when water is used to model the steel melt (Krishnapisharody & Irons 2008).

A similarity criterion known as the Weber number (We) can be used to evaluate how far the modelled system is from the actual prototype tundish. The Weber number is the ratio of momentum to interfacial tension force given by eq. 2-18 (Chattopadhyay *et al.* 2010) .

$$We = \frac{V_2^2 L \rho_2}{\sigma} \qquad 2\text{-}18$$

where:

V_2 - Velocity of the melt phase or water phase

L - Characteristic length of the tundish

ρ_2 - Density of the melt or water phase

σ - Interfacial surface tension between steel melt and slag phase

Ideally the ratio between the model Weber number and the prototype Weber number should be a unity. By using a combination of eq. 2-17 and eq. 2-18 one can calculate the ratio of the Weber number for the two systems in this study. A calculation based on a steel-slag system interfacial surface tension of 1.6 Nm^{-1} (Mills 2011, Mazumdar & Guthri 1999) and water to paraffin interfacial surface tension of 0.048 Nm^{-1} (Johansen 1924) shows that the ratio of the model and prototype Weber number is 1.21. This is considered to be close to unity and thus justifies the use of paraffin to model tundish slag.

Exceptions to physical modelling rules

Not all the dimensions of the prototype are reduced by a scale factor λ. To maintain dynamic similarity between the bath level of the prototype and that in the model, the outlet cross sectional area of the model must disobey the similarity criteria or else the model may overflow or drain out.

The outlet cross sectional area in the model is calculated and designed to maintain similarity between the prototype bath level and model bath level. As a consequence:

$$A_{\text{Outlet,Model}} \neq A_{\text{outlet,Prototype}} \times \lambda^2 \qquad \text{2-19}$$

If the tundish model is operated at steady state, the outlet cross sectional area of the model can be calculated to satisfy eq. 2-20:

$$Q_{\text{out,m}} = Q_{\text{in,m}} = A_{\text{out,m}} \times V_2 \qquad \text{2-20}$$

where:

Q - Volumetric flow of water

$A_{out,m}$ - Cross sectional area of the outlet nozzle in the model

V_2 - Velocity of water at the outlet nozzle. Given by the Bernoulli equation

Bernoulli equation for V_2:

$$V_2 = \sqrt{\frac{2\times(\rho_2 g h_2 + \rho_1 g h_1)}{\rho_2}} \qquad \text{2-21}$$

where:

h_1 - Simulated slag layer thickness

h_2 - Simulated melt phase thickness

2.6.2 Numerical modelling theory

Numerical methods make use of computer packages to solve a series of fluid mechanics differential equations in 3D or 2D space. Whereas physical modelling incorporated with fluid flow characterisation gives quantitative results about what is happening in the vessel, numerical modelling allows the investigator to gain both detailed visuals and quantitative information about the flow patterns inside the vessel. In addition to this, numerical simulations allow the investigator to gain knowledge about turbulence, pressure changes and velocity patterns inside the vessel.

Results from numerical models can be verified by comparing them to results from a physical model study. Once verified, the numerical model can be changed for use in a variety of situations without the need to do any experimental work.

Before using the computer package, it is imperative to understand the governing equations. The following sections are dedicated to explaining the governing equations behind computational fluid dynamics (CFD) modelling of the tundish.

Governing equations

Laminar regime equations

In order to model fluid flow, two main equations must be solved. These are the conservation of mass equation, otherwise known as the continuity equation (eq. 2-22), and the conservation of momentum equation (eq. 2-23). The derivation of these equations is not trivial but this is considered to be basic fluid mechanics knowledge and thus will not be discussed here. In the form given below these equations are related to laminar flow regime (ANSYS 2011).

$$\frac{\partial \rho}{\partial t} + \nabla . \left(\rho \vec{V}\right) = S_m \qquad 2\text{-}22$$

$$\frac{\partial \rho \vec{V}}{\partial t} + \nabla . \left(\rho \vec{V} \vec{V}\right) = -\nabla P - \nabla . \bar{\bar{\tau}} + \rho \vec{g} + \vec{F} \qquad 2\text{-}23$$

In eq. 2-22, the first term on the left relates to changes in density as result of time, followed by changes in mass due to convection (mass flowing out of the system). S_m relates to changes in the system's mass as a result of source terms such as mass transfer, evaporation and or other methods of adding mass to a system.

In eq. 2-23, the first term on the left is the change in momentum over time. The second term is change in momentum as a result of convection (flow). On the right of eq. 2-23 is the change in momentum due to pressure changes, shear stress, gravitational forces and bodily forces respectively (ANSYS 2011).

For Newtonian fluids whose density does not change with time, the first term of both the momentum and continuity equation is zero.

The following definitions apply to both the continuity equation and the conservation of momentum equation:

where:

$\vec{V}$ - Velocity vector of the fluid element in x-y-z direction

S_m - Mass source terms

ρ - Density of the fluid

P - Pressure exerted on the fluid element in x-y-z direction

$\vec{g}$ - Gravitational field vector acting on the fluid element

$\vec{F}$ - Force vector on a fluid element

$\bar{\bar{\tau}}$ - Shear stress tensor in the x-y-z direction given by

$$\bar{\bar{\tau}} = \mu\left[\left(\nabla\vec{V} + \nabla\vec{V}^{T}\right) - {}^{2}/_{3}\,\nabla.\vec{V}l\right] \qquad 2\text{-}24$$

where:

μ - Molecular viscosity of the fluid

l - Unit tensor

The above mentioned equations are applicable to laminar flow regime for turbulent regime similar but slightly different equations are used. The principle of conservation of momentum and mass are still applicable.

Turbulent regime equations

To derive conservation of momentum equations for turbulent regimes, it is important to explain transfer of momentum in laminar and in turbulent regimes. Figure 2-7 shows a simple Newton experiment. A fluid is placed between two plates. The bottom plate is moving at a velocity, V, in the x-direction, because of a force (F) being applied to it. Because of the movement of the bottom plate, the layer of fluid just above the bottom plate begins to move and soon moves at a velocity of V. The layer of fluid closest to the upper plate does not move. Thus a velocity profile is generated in the y-direction.

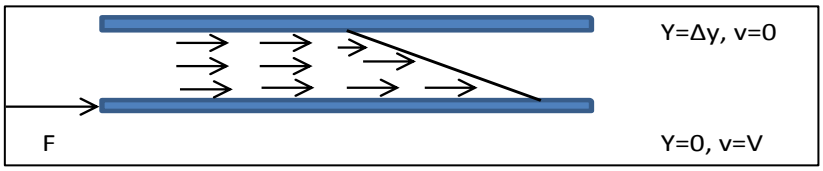

Figure 2-7 Newtonian experiments for shear stress and momentum transfer

In a laminar regime such as shown in Figure 2-7, the velocity profile exists because of intermolecular forces between the fluid layers. The velocity profile is directly proportional to the shear stress caused by the moving bottom plate. The proportionality constant, as Newton found, was the viscosity of the fluid.

In turbulent regimes, fluid layers are not streamlined as in laminar flow regimes because of the presence of eddy currents. The eddy currents cause fluctuation in the velocity, pressure and other fluid properties. Within a well-developed turbulent flow there can be a variety of sizes of eddy currents ranging from large eddy currents which can interact with each other

to form medium sized eddy currents. The medium eddies can in turn interact to give rise to small eddies which lose their energy to viscous forces and disappear (Sahai & Emi 2008).

At any given time the velocity and pressure of the fluid is given by eq. 2-25 and 2-26.

$$v_i = \overline{v_i} + v_i' \qquad 2\text{-}25$$

$$P = \overline{P} + P' \qquad 2\text{-}26$$

In general, in turbulent regimes any scalar at any point in time is given by:

$$\emptyset_i = \overline{\emptyset_i} + \emptyset_i' \qquad 2\text{-}27$$

where:

$\emptyset$ - Instantaneous scalar quantity

$\overline{\emptyset}$ - Average scalar quantity over the calculation period

$\emptyset'$ - Fluctuating scalar component at the time of interest

Substituting eq. 2-25 into 2-22 and 2-23 gives:

$$\frac{\partial \rho}{\partial t} + \frac{\partial}{\partial x_i}(\rho v_i) = S_m \qquad 2\text{-}28$$

$$\frac{\partial(\rho v_i)}{\partial t} + \frac{\partial(\rho v_i v_j)}{\partial x_j} = -\frac{\partial P}{\partial x_i} + \frac{\partial}{\partial x_j}\left[\mu\left[\left(\frac{\partial v_i}{\partial x_j} + \frac{\partial v_j}{\partial x_i}\right) - {}^2/_3\,\delta_{ij}\frac{\partial v_l}{\partial x_i}\right]\right] + \frac{\partial(-\rho\overline{v'_i v'_j})}{\partial x_j} + \rho\vec{g} + \vec{F} \qquad 2\text{-}29$$

Eq. 2-28 and 2-29 are known as Reynolds-averaged Navier-Stokes (RANS) equations. Unlike eq. 2-22 and 2-23 which are instantaneous, RANS equations are averaged over the flow time (ANSYS 2011). In particular the term $\rho\overline{v'_i v'_j}$, which is known as Reynolds stresses, needs to be known to complete eq. 2-28 and 2-29. This presents a problem in that the average fluctuating component of the velocity field has to be known in order to calculate the instantaneous velocity field. It is for this reason that turbulent models were derived.

Turbulence models

Turbulence models are used to calculate the turbulent viscosity in the calculation domain. Once the turbulent viscosity is known, knowledge of how velocity in the calculation domain changes with time and direction as a result of turbulent sheer stress can be known. The turbulent viscosity can be a function of time and location or it can be independent of both time and location, i.e. constant (Sahai & Emi 2008).

The models used to calculate the turbulent viscosity range from simple algebraic equations to more sophisticated models involving differential equations. Table 2-4 below shows a list of some of the popular turbulence models with their strengths and weaknesses.

Table 2-4 List of Turbulence Models with their weakness and strengths (Bakker 2008)

Model	Strength	Weakness
Spalart-Allmaras	Economical. Good record for mildly complex flows	Not very widely tested; lack of sub models (e.g. combustion, buoyancy). Not good for 3D flows
STD k-ε	Robust, economical, reasonably accurate; performance is well known	Poor results for complex flows with large pressure gradients, strong streamline curvature, swirl and rotation. Poor results for flow developed flow in round jets. Assumes whole flow is turbulent
RNG k-ε	Good for moderately complex behaviour like jet impingement, separating flows, swirling flows, and secondary flows	Subject to limitations due to isotropic eddy viscosity assumption. Same problem with round jets as STD k-ε. Hard to converge
Realizable k-ε	Offers the same benefits as RNG. Good for shear flows and flows with local transitional zones	Subject to limitations due to isotropic eddy viscosity assumption
Reynolds Stress Model	Most complete model (history, transport, and anisotropy of turbulent stresses are all accounted for)	Requires more computing power (2-3 times more); momentum and turbulence equations are coupled and may be unsteady at times

The most extensively used model in the past for tundish modelling was the STD k-ε model (Mazumdar & Guthri 1999). Since the development of the realizable k-ε model more researchers tend to use the latter due to the added advantage it has when it comes to modelling large pressure gradients and streamlined flows.

In the STD k-ε model, k is the kinetic energy per unit mass of fluid and ε is the rate of energy dissipation. Mathematically:

$$k = \frac{1}{2}(\overline{v_i'^2} + \overline{v_j'^2} + \overline{v_k'^2}) \qquad 2\text{-}30$$

where:

$\overline{v_i'^2}$ - Average squared fluctuating component of the turbulent velocity

The values of k can be calculated from the following differential equations:

$$\frac{\partial}{\partial t}(\rho k) + \frac{\partial}{\partial x_i}(\rho k v_i) = \frac{\partial}{\partial x_i}\left[\left(\mu + \frac{\mu_t}{\sigma_k}\right)\frac{\partial k}{\partial x_i}\right] + G_k + G_b - \rho\varepsilon - Y_M + S_k \qquad 2\text{-}31$$

While ε can be calculated from:

$$\frac{\partial}{\partial t}(\rho \varepsilon) + \frac{\partial}{\partial x_i}(\rho \varepsilon v_i) = \frac{\partial}{\partial x_i}\left[\left(\mu + \frac{\mu_t}{\sigma_k}\right)\frac{\partial \varepsilon}{\partial x_i}\right] + C_1\frac{\varepsilon}{k}(G_k + C_3 G_b) - C_2\rho\frac{\varepsilon^2}{k} + S_\varepsilon \qquad 2\text{-}32$$

where:

G_k - Rate of generation of kinetic energy per unit mass given by:

$$G_k = \mu_t\left[\frac{\partial v_i}{\partial x_j} + \frac{\partial v_j}{\partial x_i}\right]\frac{\partial v_i}{\partial x_j} \qquad 2\text{-}33$$

μ_t - Kinematic turbulent viscosity

μ - Molecular viscosity

G_b - Generation of turbulent energy due to buoyancy

Y_M - Changes in dilation (compressible fluids)

S_k - User defined source terms

S_ε - User defined source terms

The turbulent viscosity can then be calculated by:

$$\mu_t = \frac{C_\mu \rho k^2}{\varepsilon} \qquad 2\text{-}34$$

C_1, C_2, σ_k, σ_ε and C_μ are constants. Table 2-5 shows the values of these constants.

In the Realiazable k-ε model the C_μ term has a differential equation as opposed to being constant; moreover the dissipation equation is based on a dynamic equation of the mean-square vorticity fluctuation. This gives the Realizable k- an advantage over the standard k- equations when calculating flows that show strong streamline curvature, vortices, and rotation (ANSYS 2011).

Table 2-5 k-ε model constant values (Launder *et al.*, 1974)

Constant	Typical value
C_1	1.44
C_2	1.92
C_μ	0.09
σ_k	1.00
σ_ε	1.30

Two phase modelling

Multiphase flow in ANSYS FLUENT can be solved by two methods; the Euler-Lagrange approach and the Euler-Euler approach. In the Euler-Lagrange approach, the fluid is treated as small particles where interpenetration is not permissible. In contrast, the Euler-Euler approach treats the different phases as interpenetrating continua which allows one to study their mixing patterns (ANSYS 2011).

In the latter approach, to keep track of each phase in the calculation domain, the volume fraction of each phase is tracked. Conservation equations for each phase are derived to obtain a set of equations which have a similar structure for all phases. These equations are then solved in the calculation domain to obtain a solution (ANSYS 2011).

Three different Euler-Euler multiphase models are available in ANSYS FLUENT to solve multiphase flow; the volume of fluid (VOF) model, the mixture model, and the Eulerian model (ANSYS 2011).

The VOF model is appropriate for stratified or free-surface flows, while the Mixture and Eulerian models are appropriate for flows in which the phases mix or separate and/or the dispersed phase volume fractions exceed 10 % (ANSYS 2011).

Since the water-paraffin fluids used in this study were free surface flows and the volume fractions were expected to be lower than 10 %, the VOF model was chosen.

VOF consists of three methods to model fluid interactions; a methodology to locate the free surface, an algorithm allowing the tracking of free surface as it moves through the computational domain and a method allowing boundary conditions to be applied at the free surface (Reilly *et al.* 2013).

Material properties of the combined fluid mixture are calculated using the individual fluid properties and their volume fractions in the concerned region. An example of this is the

fluid density in each calculation cell, given by eq. 2-35. All other fluid properties are calculated in a similar manner (ANSYS 2011):

$$\rho = \sum_{i=1}^{n} a_i \rho_i \qquad 2\text{-}35$$

where:

ρ_i - Individual fluid density

a_i - Volume fraction of the i-th phase in the concerned cell volume

A single momentum equation is solved for all the phases, where the fluid properties are calculated in a similar manner as eq. 2-35. The resulting velocity is shared amongst the phases i.e. assumed to be equal for all phases present. The drawback to this method of calculating the fluid velocities is that it can overestimate the velocity of one of the phases when a large velocity difference exists between the phases as experienced when two fluids of large viscosities differences are mixed (viscosity ratio of larger than $1x10^3$). This tends to have a negative effect on the accuracy of the velocities computed near the interface (ANSYS 2011). In the case considered in this study, the viscosity ratio (paraffin/water) is 1.26 thus the above problem does not apply.

Interface tracking is achieved by solving a continuity equation that incorporates the volume fraction of each phase, eq. 2-36 (ANSYS 2011).

$$\frac{1}{\rho_i}\left[\frac{\partial(a_i\rho_i)}{\partial t} + \nabla.(a_i\rho_i\vec{v_i}) = Sa_i + \sum_{i=1}^{n}(\dot{m}_{ij} - \dot{m}_{ji})\right] \qquad 2\text{-}36$$

Where:

Sa_i - Rate of generation of the i-th phase

m_{ij} - Mass transfer rate of i-th phase into the j-th phase

For surface tension modelling, one can choose to specify a constant surface tension coefficient or choose to specify a user-defined equation for surface tension. The VOF model then adds additional tangential stresses that arise due to variable changes in surface tension at the interface. Two surface tension models exist in the VOF model, the continuum surface force (CSF) and the continuum surface stress (CSS). Essentially these models are used to calculate the surface tension force (ANSYS 2011).

In the continuum surface force model the surface tension force is calculated by first calculating the surface curvature from local gradients in the surface normal at the interface. The continuum surface stress model is a more conservative model. It avoids calculating the surface curvature to solve for the surface tension force and thus misses some activity at the interface (ANSYS 2011).

Since the primary objective of this study is to model the entrainment process; the less conservative CSF model ought to be used to yield accurate results.

Boundary conditions

Boundary conditions specify, inter alia, direction of flow, fluid source and sink, and how the flow must behave in certain regions.

Boundary conditions can be split into inlet conditions, outlet conditions, wall conditions and surface conditions.

Inlet conditions

Inlet conditions involve specifying the position of the inlet, direction of flow, pressure and whether the velocity has a profile or not.

In the case of a turbulent flow entering at the inlet region, the turbulent kinetic energy and dissipation have to be specified. One method to specify the turbulence at the inlet is to specify the turbulence intensity and hydraulic diameter. The turbulence intensity is given by eq. 2-37, and the hydraulic diameter is the diameter of the duct (Bakker 2008).

$$I = \frac{\sqrt{2/3k}}{V} \qquad 2\text{-}37$$

where:

I - Turbulence intensity, typically 5% for fully developed flow in a pipe

k - Turbulence kinetic energy

V - Average velocity in the pipe

Outlet conditions

The velocity at the outlet is assumed not to have a profile and is given by eq. 2-21. Pressure at the outlet is given by the hydrostatic pressure. The outlets are assumed to be open to the atmosphere. All flow property gradients are zero over the outlet region except for pressure (Bakker 2008).

Wall conditions

Wall boundaries are specified to allow the software to know where the boundaries are. The no slip conditions are used for viscous flows meaning that the tangential velocity of the fluid closest to the wall has the same velocity as the wall and that the normal fluid velocity at the wall is zero.

The presence of the wall and the choice of no slip conditions affect how turbulence is dissipated near the wall.

In particular, regions closest to the wall are dominated by laminar flow where viscous forces play a significant role. At the outer parts of the wall, momentum transfer is dominated by turbulent conditions. The area between the laminar and turbulent regions is dominated by both laminar and turbulent dissipation of momentum.

To resolve flow patterns in near wall regions, one can use semi-empirical formulas known as wall functions or modified turbulence models. In the wall functions, the viscosity dominated region is not resolved, and instead semi-empirical models are used to calculate the flow behaviour in the viscous layer near the wall.

In modified turbulence models, the flow behaviour is resolved all the way to the wall. This involves making use of fine mesh sizes near the wall region, which cost in computational time.

For ε based equations, wall enhanced wall treatment functions are recommended and thus will be used in this study (Bakker 2008).

Top surface conditions

One can also choose to specify frictionless wall conditions. This has been the norm for most researchers who have done work in the field. They specified the boundary condition at the top of the fluid layer (Cloete 2014, Kumar *et al.* 2008, Mazumdar & Guthri 1999, Sahai & Emi 1996, Tripathi & Ajmani 2011). It is worth mentioning though that this boundary condition was used without the presence of the slag phase. The implication of this is that there are zero nominal velocity gradients at the very top of the tundish fluid level and that all velocity vectors are bounced back from the top surface. The other implication of this is that the free surface is not allowed to have waves. This boundary condition can be problematic in this study as it may result in an unrealistic “free” surface which is not allowed to be mobile and non-realistic mixing due to flow being reflected from the “free” surface in the numerical model.

Symmetry conditions

Symmetry conditions are considered when the flow in a vessel is thought to have planes of symmetry. These can be transverse, longitudinal or vertical. Considering symmetry planes lowers the computational time demand of the software (Bakker 2008).

When this condition is specified, the following constraints are activated:

- Zero normal velocity at the symmetry plane
- Zero normal gradients of all variables at the symmetry plane

Meshing theory

Cell choice

Mesh topography defines the cells in which the flow equations will be solved. It does this by breaking the geometry of the problem up into discrete groups of cells to which boundary conditions are applied (Bakker 2008).

The type of mesh topography used in the model determines the solution accuracy, computational time required to solve the problem and the rate of the model convergence (Bakker 2008).

One can choose from triangular, quadrilateral, tetrahedron, hexahedron (hexagonal), pyramids, wedges, polyhedral and arbitrary polyhedron cells. The choice of which cells to use depends on the set up time, computational time demand and numerical accuracy that is achieved by using that particular type of cell (ANSYS 2011). Table 2-6 gives a general guideline for selecting which cells are suitable for which problems.

Table 2-6 Guideline for cell choice (ANSYS 2011)

Geometrical type	**Ideal cell type**
Simple	Quadrilateral
Moderately complex	Unstructured quadrilateral/ hexahedral
Complex	Triangular/ tetrahedral with prism layer
Extremely complex	Triangular/ tetrahedral

The geometry considered in this study is fairly simple leaning to moderately complex, thus the hexahedral cells should be employed. The use of hexagonal cells also lowers the number of cells as compared to tetrahedral mesh. Cloete (2014) however used tetrahedral cells. This was not done in this study because it is generally understood that hexahedral cells yield better results with two phase modelling (Bakker 2008).

Mesh quality

Mesh quality can be judged from the cell's skewness, smoothness and aspect ratio. Cell skewness of hexahedral cells can be defined as the measure of deviation of the hexahedral cell from a cube. Mathematically this is given by eq. 2-38. A skewness value of 0 is ideal and 1 is not favourable. An accepted maximum value of 0.85 is allowable for hexahedral cells (Bakker 2008).

$$Skewness = \left[\frac{\theta_{max}-90}{90}; \frac{90-\theta_{min}}{90}\right] \quad 2\text{-}38$$

where:

θ_{max} - Largest angle in the hexahedral

θ_{min} - Smallest angle in the hexahedral

- Cell smoothness is defined as the change in size between neighbouring cells. Ideally size change between neighbouring cells should not be greater than 20 % (Bakker 2008).
- The cell aspect ratio is defined as the ratio between the longest edge length and the shortest edge length (Bakker 2008). A value of 1 is ideal, while large values are not ideal.

Solver theory

Solution bases

ANSYS Fluent has two solver bases to solve the flow equations; the pressure-based solver and the density-based solver (ANSYS 2011).

In the pressure-based solver, the pressure of the system is derived by manipulating the continuity and momentum equations; the velocity is then calculated to satisfy the continuity equation. Since the velocity and pressure need to satisfy the momentum and continuity equations, an iterative calculation process is needed to satisfy both equations. One can choose between two iterative algorithms for this, a segregated algorithm and a coupled algorithm. In the segregated algorithm, pressure and momentum are solved sequentially whereas in the coupled algorithm, momentum and pressure are solved simultaneously (ANSYS 2011).

In the density-based solver, the continuity equation is used to find the density of the system while the pressure of the system is derived from an equation of state (ANSYS 2011).

In terms of applicability, the pressure-based solver in both the segregated form and coupled form is in most cases, more appropriate. Its use ranges from low speed incompressible flow to high speed compressible flow. The density-based solver is applicable to flows where there is a strong dependency or interdependency between density, momentum and species. Within the Pressure-based solver, the coupled version is much more computationally time efficient (ANSYS 2011).

Spatial discretisation

During the solution steps, flow variables are stored at the centre of the grid cells. To be able to solve the flow patterns across the entire calculation field, the programme needs the values of the flow variables at the faces of the grid cell. Flow variables at the faces of the grid cells are interpolated from the centre cell values (ANSYS 2011). Figure 2-8 is an illustration of this idea.

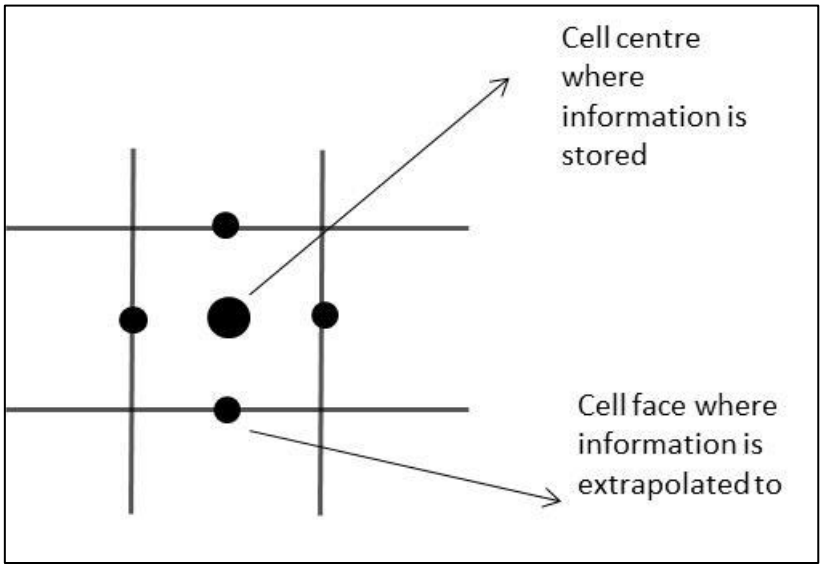

Figure 2-8 Grid cell illustration of information storage in ANSYS Fluent. (Redrawn from ANSYS 2011)

ANSYS Fluent has five interpolating schemes for interpolating flow scalar values. Table 2-7 below lists the names and properties of these schemes.

Table 2-7 Interpolating schemes in Fluent and their properties (ANSYS 2011)

Scheme Name	**Properties**
First Order	Easiest to converge but not accurate. Only first order accurate
Power Law	More accurate than first order. Good for low Reynolds Number flows
Second Order Upwind	More accurate, second order accurate. Good for tri/tet mesh.
MUSCL	3rd order accurate, more useful for predicting secondary flow, vortices and body forces
QUICK	Applicable to hexagonal or quadrilateral meshes. 3rd order accurate

In cases where the solution basis is pressure based, five interpolating schemes are available, specifically for the pressure in the system. These are shown in Table 2-8

Table 2-8 Interpolating Schemes in ANSYS Fluent for pressure (ANSYS 2011)

Scheme Name	Properties
Standard	Not useful for flows which exhibit large pressure differences
PRESTO!	For flows with steep pressure differences and swirl flow
Linear	To be used when other methods result in convergence difficulty or unphysical behaviour
Second Order	Useful for compressible flows. Not to be used for VOF or mixture multiphase flows
Body force weighted	Used when large body forces exist

ANSYS Fluent has three schemes with which it evaluates gradients of the solution variables. The gradients from these schemes are also used to calculate the diffusive fluxes and velocity derivatives. Table 2-9 lists these schemes and their properties.

Table 2-9 Gradient Schemes for variables in ANSYS Fluent (ANSYS 2011)

Scheme Name	Properties
Green-Gauss Cell Based	Least computational time intensive. Prone to false diffusion
Green-Gauss Node-Based	More accurate. Computational time intensive. For unstructured meshes
Least-Square Cell-Based	Same as Green-Gauss Node-Based but less computational time intensive

Flow characterisation in numerical modelling

A comparison between the results of a numerical RTD and those of the physical model is often the first step towards validating the numerical results.

To study the RTD of a vessel numerically using ANSYS Fluent, eq. 2-39 is solved for the tracer element (Mazumdar & Guthri 1999).

$$\frac{\partial \rho Yi}{\partial t} + \nabla.\left(\rho \vec{V} Y_i\right) = -\nabla.J_i + R_i + S_i \qquad 2\text{-}39$$

Where:

Y_i - Mass fraction of the tracer in the calculation domain

J_i - Effective mass transfer in the calculation domain given by eq. 2-40

R_i - Rate of production of the tracer by reaction

S_i - Rate of production of the tracer via addition

ρ - Density of the primary fluid or fluid in which the tracer is flowing

$$J_i = -\left(\rho D_i + \frac{\mu_t}{Sc_t}\right)\nabla Y_i \qquad 2\text{-}40$$

where:

D_i - Molecular diffusion of tracer in main fluid

Sc_t - Turbulent Schmidt Number, with a value of 0.7

μ_t - Turbulent viscosity

2.7 Summary

The role of the tundish in the steel-making process is now better understood to aid inclusion removal. The efficiency of inclusion removal in the tundish is now well understood to be dependent on the melt residence time and flow patterns in the tundish i.e. given enough residence time, and surface directed flow, maximum inclusion removal can be realised (Sahai *et al.* 1996).

Research dating back to 1979 pertaining to tundish technology has been focused on understanding and adjusting the flow patterns in the tundish. These studies have involved the use of water models, scaled models from the prototype tundishes using Froude numbers, and/or mathematical models. What has emerged from these studies is the importance of the use of flow control devices. These devices are meant to increase the melt residence time in the tundish by decreasing dead volume fractions and increasing plug flow volume fractions over mixing volume fractions. Furthermore they promote slag directed flow to increase inclusion removal.

In the above mentioned studies, the researchers used water to model the steel layer due to water's dynamic similarity to steel at 1600^{o}C. Less consideration has been given to the slag layer behaviour both in bare tundishes and in tundishes furnished with a flow control device. As a result there is little to no understanding of tundish slag behaviour in bare tundishes and tundishes furnished with flow control devices. Of particular importance is the mechanism by which tundish slag is entrained into the melt phase.

Water models can be used to model the flow behaviour of industrial vessels. Depending on the dimensionless numbers being correctly used (Reynolds number, Froude number, Webber number), the water models can successfully be used to model industrial vessels. The Reynolds number involves correctly modelling the ratio of inertial forces over gravitational forces, while the Froude number involves correctly modelling the ratio between inertial forces and gravitational forces. Sahai *et al*. (1992) argue that the Reynolds number is not unique to a tundish but instead is the same for every tundish as long as that tundish is operating in a turbulent regime. Following from this, the dimensionless number of choice in tundish modelling is the Froude number.

The Webber number (We) relates to the ratio of momentum forces to interfacial forces. The Webber number can be used to select two fluids to represent prototypical fluids. Although a variety of fluids has been used to model the slag layer in other processes, Krishnapisharody and Irons recommend the use of paraffin oils for modelling tundish slag when water is used to model the steel melt (Krishnapisharody *et al*. 2008). Krishnapisharody *et al*. (2008) recommendation was followed in this study. A small calculation was done to determine the Webber number ratio between the water model tundish and the tundish prototype. The ratio was found to be 1.21. This was deemed acceptable for this study i.e. the force ratios in the prototype were sufficiently modelled in the water model.

Methods of slag entrainment were investigated and found to be caused by: shearing of the slag layer at the interface at high and low velocities, impinging of the slag layer as a result of flow moving up the side walls, vortexing during low bath conditions and interfacial reactions which weaken the interfacial tension. Table 2-10 is a summary of the slag entrainment mechanism and their triggers. Table 2-11 lists the critical parameters specific to this study in order for entrainment to take place.

Harman *et al*. (1996) studied the size of the entrained slag droplet and found it to be given by eq. 2-11. From this equation the entrained paraffin (slag) droplet size in this study be 43 mm in diameter. This is slightly higher than what Harman *et al*. (1996) calculated, 5-32 mm for varying kinematic viscosity ratios, but it is important to note that the kinematic viscosity ratio used in this study is at the high end of what Harman *et al.* (1996) studied hence the size of the diameter.

Table 2-10 Slag entrainment mechanism summary

Mechanism (Developer)	Action- trigger	Entrainment criteria
Shearing at the interface (Hagemann *et al.* 2013)	Interface. When $Ca(V_2)>Ca^*$	$Ca^* = 3 \times 10^{-6}\left(\frac{\nu_1}{\nu_2}\right) + 2.8 \times 10^{-3}$ $Ca = \frac{V_2 \eta_2}{\sigma}$
Shearing at the interface low velocities (Kelvin and Helmholtz)	When steel velocity tangential to the interface exceeds critical velocity	$\Delta V_{crit} = \sqrt[4]{4g(\rho_2 - \rho_1)\sigma\left[\frac{1}{\rho_2} + \frac{1}{\rho_1}\right]^2}$
Shearing at the interface low velocities neglecting interfacial tension and viscosity (Milne-Thomson 1968)	When steel velocity tangential to the interface exceeds critical velocity	$\Delta V_{crit} = \sqrt{g(\rho_2 - \rho_1)\left(\frac{H_2}{\rho_2} + \frac{H_1}{\rho_1}\right)}$
Vortexing	At low bath levels	N/A
Turbulence at the interface	High velocity slag directed flow	N/A
Mass transfer across interface	Concentration difference	N/A
Gas bubbling and surface reactions	Lower interfacial tension	N/A

Table 2-11 Entrainment limits specific to this study

Entrainment criteria	Calculated critical velocity (m/s)
$Ca^* = 3 \times 10^{-6}\left(\frac{\nu_1}{\nu_2}\right) + 2.8 \times 10^{-3}$	1.34×10^{-1}
$Ca = \frac{V_2 \eta_2}{\sigma}$	
$\Delta V_{crit} = \sqrt[4]{4g(\rho_2 - \rho_1)\sigma\left[\frac{1}{\rho_2} + \frac{1}{\rho_1}\right]^2}$	2.15×10^{-1}
$\Delta V_{crit} = \sqrt{g(\rho_2 - \rho_1)\left(\frac{H_2}{\rho_2} + \frac{H_1}{\rho_1}\right)}$	9.44×10^{-1}

3. EXPERIMENTAL METHOD

3.1 Physical model set-up

3.1.1 Dimensions

The physical model used in this study was designed by Cloete (2014). The design is based on a tundish used by Kumar et.al. (2008) but instead of a scale factor of 1/3 as used by Kumar and co-workers used, a scale factor of 1/2 was used by Cloete (Cloete 2014, Kumar *et al.* 2008). The model is constructed from clear 6 mm PVC. It has four strands instead of the normal one or two strands. It has walls inclined at 10°. Figure 3-1 is a schematic representative of the tundish.

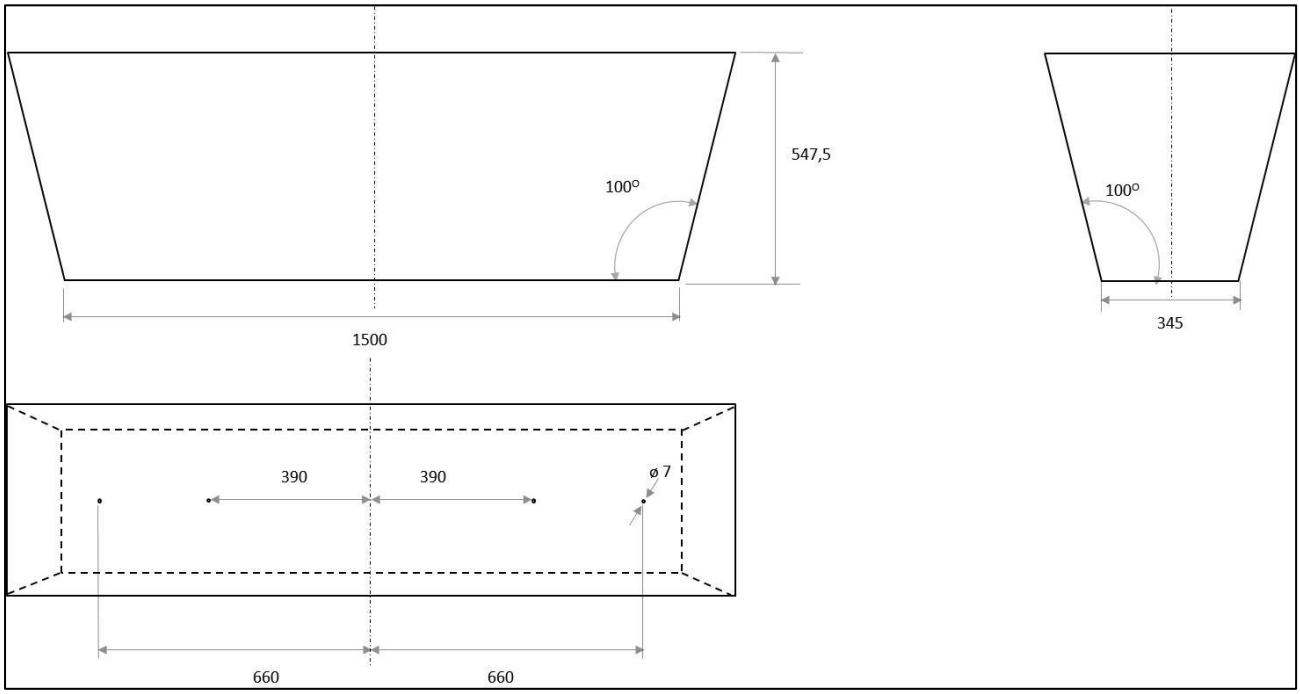

Figure 3-1 Dimensions of the tundish model. (a) Front view, (b) Side view and (c) Top view

Table 3-1 below lists the dimensions and operating conditions of the prototype (industrial scale) and the model used in this study.

Table 3-1 Dimensions and operating conditions of prototype and reduced model

Property	Prototype	Water model
Length at base(m)	3.00	1.50
Volume (L)	2000	250
Volumetric flow rate (L/h)	8 700	1572
Melt height (m)	0.78	0.39
Slag height (m)	-	0.02
Entry nozzle depth (in tundish) (m)	-	0.48

Table 3-2 below lists the properties of the two liquids used in the water model.

Table 3-2 Operating fluid properties (ANSYS Fluent)

Property	water	Paraffin
Density (kg/m^3)	998.2	780
Viscosity (kg·m^{-1}·s^{-1})	1.00 x10^{-3}	2.40 x10^{-3}
Kinematic viscosity (m^2/s)	1.00 x 10^{-6}	3.08 x10^{-6}
Fluid thickness (m)	0.39	0.02
Interfacial tension (N/m) (Johansen 1924)	0.048	
Operating temperature range (^{o}C)	19-25	19-25

It is important to note here that slag thickness is often not mentioned in studies. Often researchers quote the bath height, which is taken as the melt bath height. Distinction should be made in this study between the total bath height, steel height and slag height.

The velocity of the water exiting the tundish is driven by the hydrostatic pressure of the two fluids; water and paraffin. The velocity can be calculated using eq. 2-21. The volumetric flow rate of water flowing out of the model is given by eq. 3-1. The strand outlet diameter was designed by Cloete (2014) to be 7 mm.

$$Q_2 = \sum_{i=1}^{n} V_{2,i}\, A_{outlet} \qquad 3\text{-}1$$

where:

i - ith strand

n - Number of strands

A_{outlet} - Cross sectional area of the stand

V_2 - Velocity of water leaving via the stand

3.1.2 General set up

Figure 3-2 below shows a schematic lay out of the experimental set-up. Water is fed from the mains to a feed tank, which is kept at a fixed level by a float valve. From the feed tank the water is pumped to the tundish. The inlet flow rate is controlled by a gate valve (V-2) and a rotameter (3). The four ball valves (V-3, V-4, V-5 and V-6) can be closed to stop outlet flow, which is driven by gravity, to allow the tank to fill up. The water from the outlets is fed back to a storage tank (Cloete 2014).

Details on the inlet (4 and 5) configuration and justification of the set up can be found in (Cloete 2014).

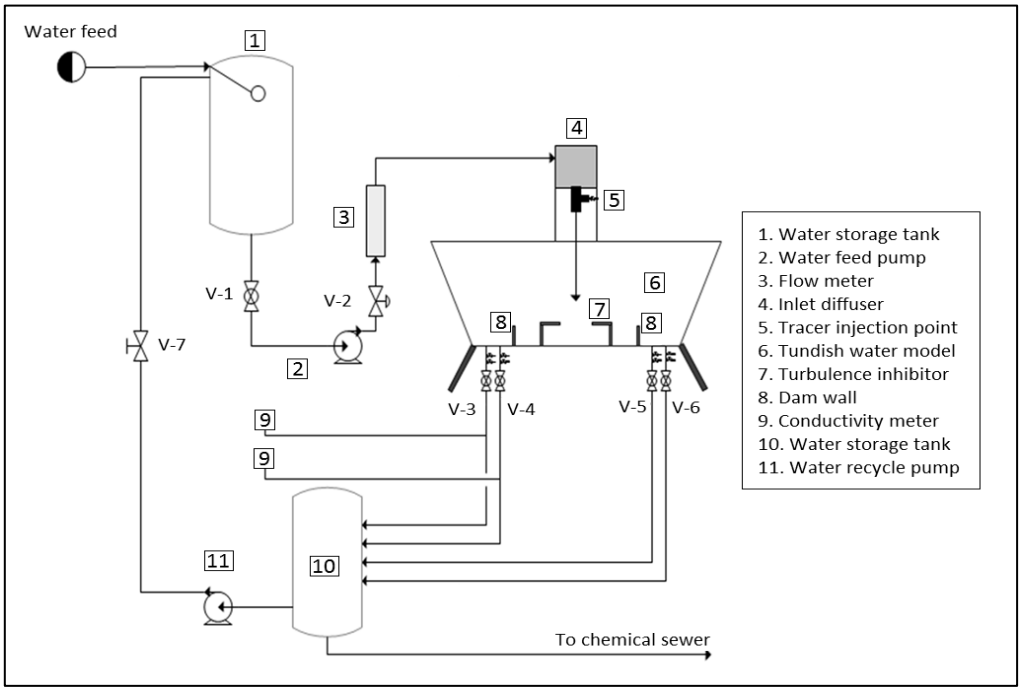

Figure 3-2 Experimental set-up (Cloete 2014)

Figure 3-3 shows the dimensions of the flow control device used in this study. The design is based on work done by Cloete (2014). The flow control device is constructed from 15 mm thick grey PVC. It was fixed in position and sealed with silicon.

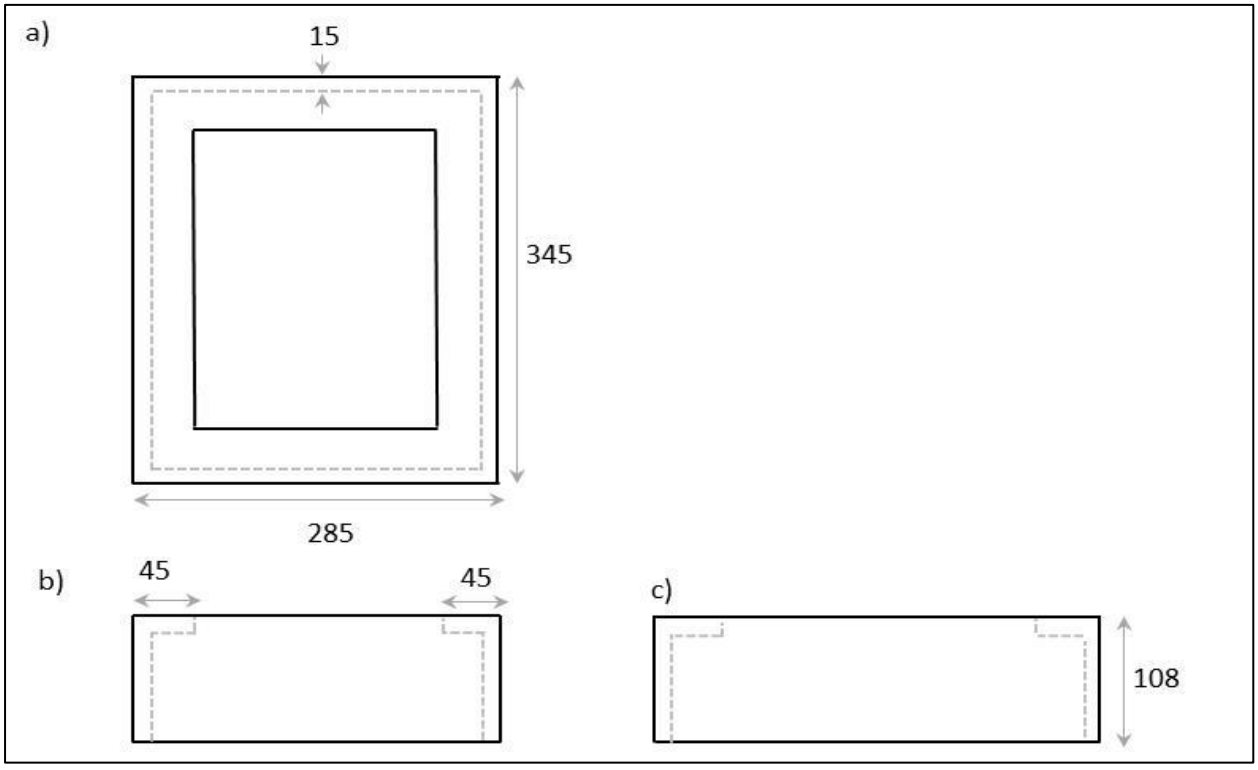

Figure 3-3 Turbulence Inhibitor dimensions a) Top view, b) Front view, c) Side view

3.2 Operating procedure and sampling protocol

3.2.1 Start-up procedure

To start the experiment, the following steps must be followed:

- Ensure that the main feed line to the storage tank is open
- Ensure that v-1 and v-2 are open and that the tracer injection point is closed
- Ensure that v-3, v-4, v-5 and v-6 are closed
- Start the water feed pump to fill the model with water. Fill the model up to the desired water level of 390 mm. Stop the pump when this level is reached
- Use a bucket to fill the model with 20 mm of paraffin
- Open v-3, v-4, v-5 and v-6. Also open the micro-valves on the outlet pipes to control the flow out of the strands
- When flow out of the tundish is steady, start the pump and adjust the flow meter to give 1547 l/h
- Allow 45 minutes for the system to stabilise before commencing tests

3.2.2 Dispersed phase sampling for paraffin (slag) entrainment

Sampling approach

The dispersed phase hold up sampling approach was employed to determine the concentration of the simulated slag phase throughout various regions of the tundish. This involved taking 50 ml samples with a pipette from the tundish whilst in operation, weighting the sample using a two-decimal place weighing scale to determine to sample's mass, from there calculating the sample's density and then the volume fraction of entrained paraffin at that location using eq. 3-2. The density of water and paraffin used in eq. 3-2 was determined by taking ten 50 ml samples of each fluid and weighing them to determine their mass. This was done every day during the sampling period to account for changes in water density due to weather.

$$x_{vol.fraction} = \frac{\rho_{sample} - \rho_{water}}{\rho_{paraffin} - \rho_{water}} \qquad 3\text{-}2$$

To avoid systematic errors, the location at which a sample was to be taken was programmed into Microsoft Excel to be random. Five repeats of each sampling location were taken. The locations where the samples were taken were dictated by the results achieved by Cloete (2014).

Sampling locations

In his thesis, Cloete (2014) studied the flow patterns in the tundish model used in this study. In his work, he investigated the effect of different flow control devices on the melt flow behaviour. However, like other authors, he did not include the slag layer. Based on his work, areas where entrainment at the interface might occur can be predicted. Moreover

dead volumes where entrained "slag'' might or might not accumulate can be identified. This was the basis for the physical grid design and sampling locations.

Figure 3-4 depicts a longitudinal view of the flow patterns which exist in a bare tundish. It can be seen from Figure 3-4 that relatively large velocity flow fields (1.5 $x10^{-2}$ - 2 $x10^{-2}$ m/s) in the downward direction exist near the entry nozzle (Region A), these flow fields tend to fade away towards the tundish walls where the velocity flow fields are 5 $x10^{-3}$ – 1 $x10^{-2}$ m/s (Region B). It is expected that the majority of the entrainment caused by shearing or Kelvin-Helmholtz instability will take place in Region A due to the relatively high velocities in this region.

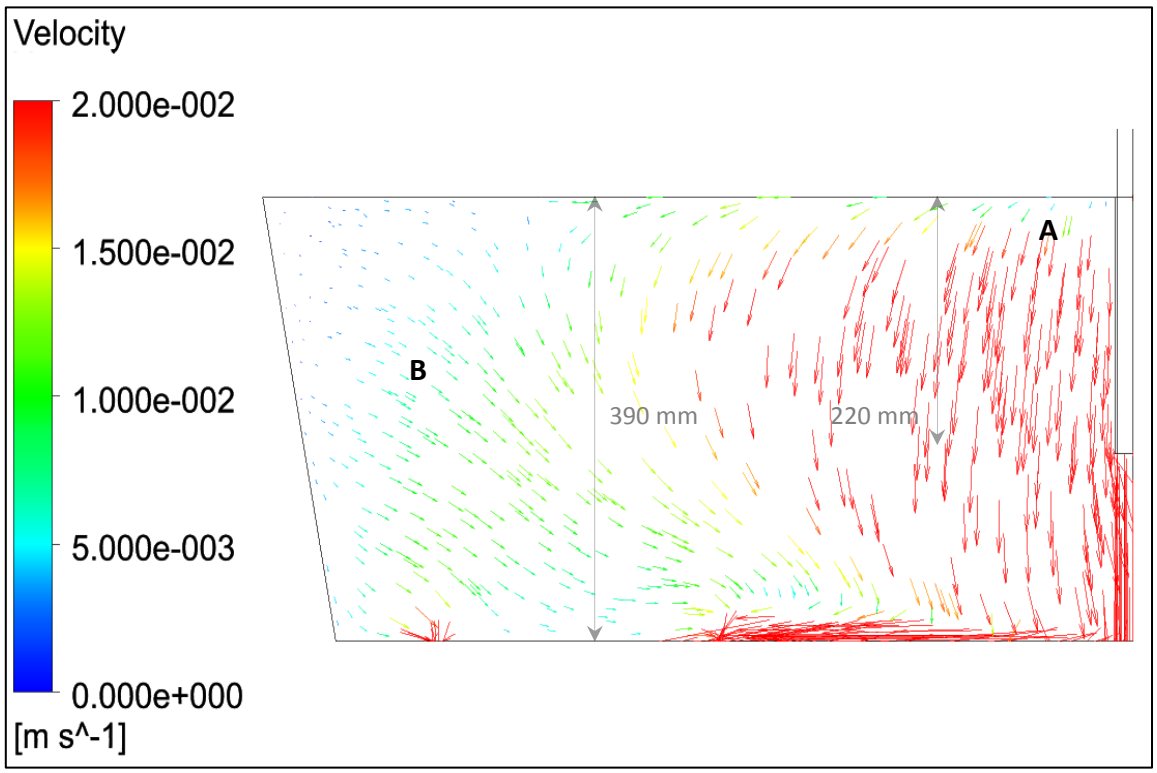

Figure 3-4 Longitudinal view of the flow pattern in a bare tundish (Adopted from Cloete 2014)

Figure 3-5 shows a transverse view of the flow patterns in a bare tundish. High velocity flow (1.5 $x10^{-2}$ – 2 $x10^{-2}$ m/s) tangential to the interface exist in Region C. This flow pattern suggests that the "slag" entrainment at the interface should start taking place in Region C. This entrained "slag" should travel with the prevailing flow that is down the centre line of the tundish and can potentially get trapped in the eye of the flow (Region D). Region C would not be ideal for sampling because most of the entrainment might takes place in this region and thus no major spatial difference will be realised and measured. Region D however, which is just above half way into the melt, could provide interesting contour plots, the half depth mark is 195 mm in Cloete (2014).

It is important to note that the above figures from Cloete (2014) do not include a slag layer and that the identified Region D will shift positions to lower depths when the slag layer is included, for this reason sampling in this study was done at a depth of 220 mm.

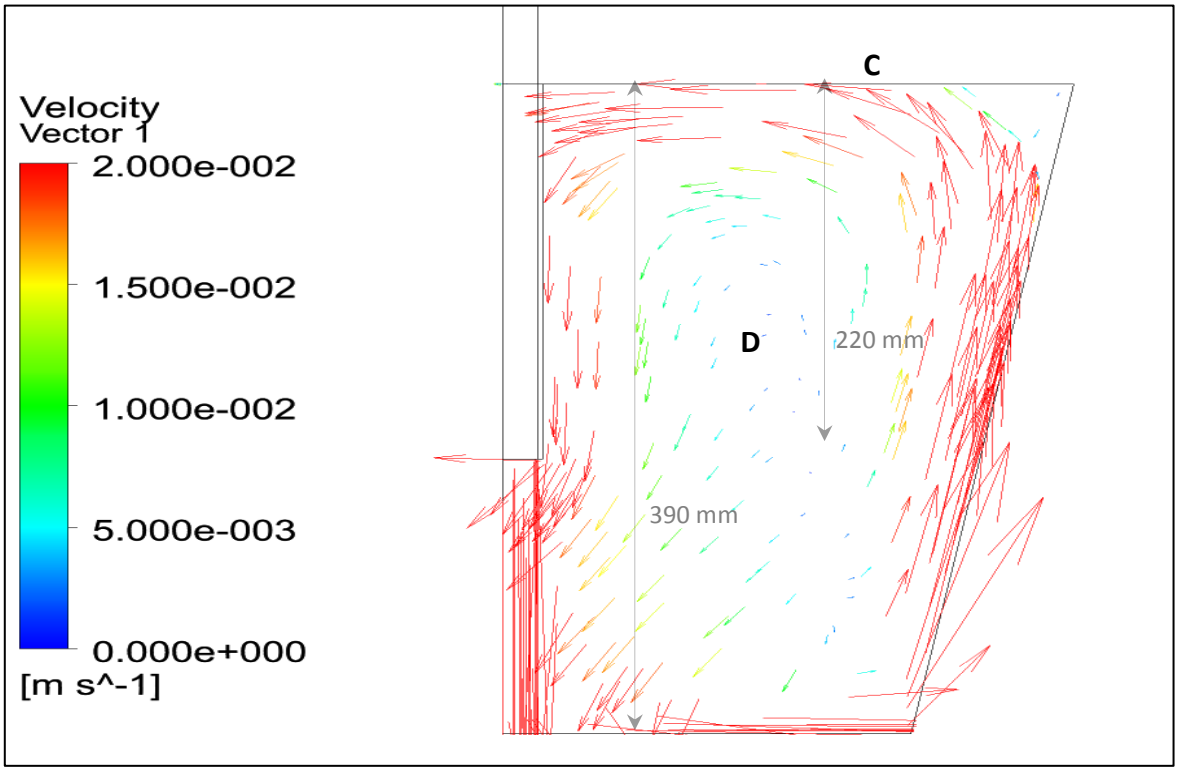

Figure 3-5 Transverse view of flow patterns in bare tundish (Adopted from Cloete 2014)

By using a flow control device, the turbulence from the entry nozzle is contained in the region above the flow control device, as can be seen in Figure 3-6 Region E where the velocity flow fields are 2 x10^{-2} m/s. Shearing of the slag layer and entrainment might also be contained in this region.

Based on the above information, a physical grid to mark where samples were to be taken could be constructed. A fine resolution grid was needed close to the entry nozzle, and coarser grid size was needed towards the end walls of the tundish, hence the design of the grid. Sampling was done at 220 mm depth. It is worth noting that the tangential velocities close or at the “interface” for both the bare and tundish with a FCD are significantly lower than the critical velocities calculated in Table 2-11 hinting that there could either be no entrainment or that if there is any entrainment of the slag layer it does not take place via the methods identified.

Figure 3-7 shows a top view of the physical grid where samples were taken. The numbers (sampling locations) on the grid should be used in conjunction with Appendix B Figure 3-8 is a transverse view of the tundish with the grid on top and the depth from which samples were taken.

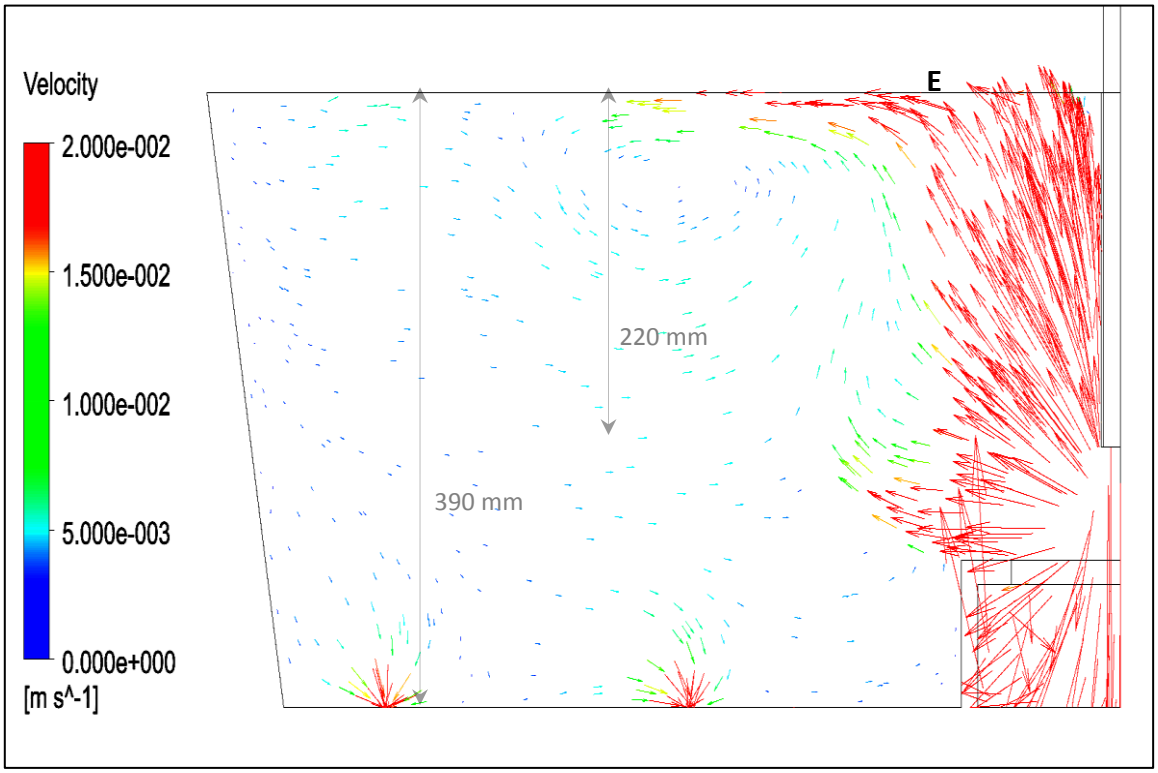

Figure 3-6 Longitudinal view of flow patterns in a tundish with the flow control device (Adopted from Cloete 2014)

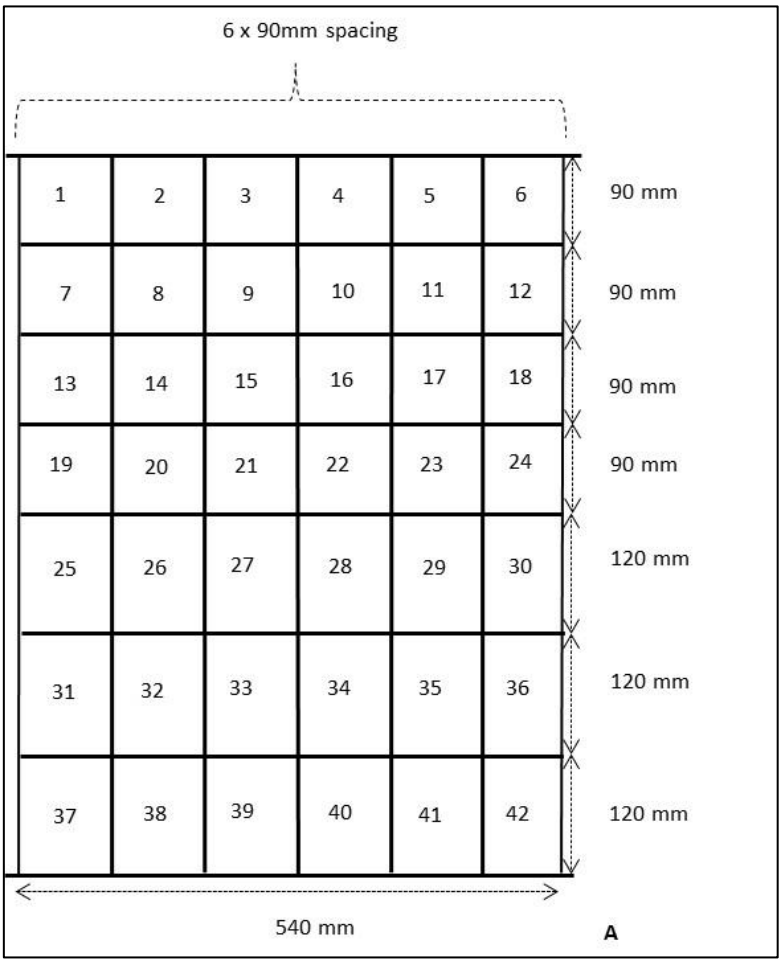

Figure 3-7 Top view and dimensions of the physical grid used

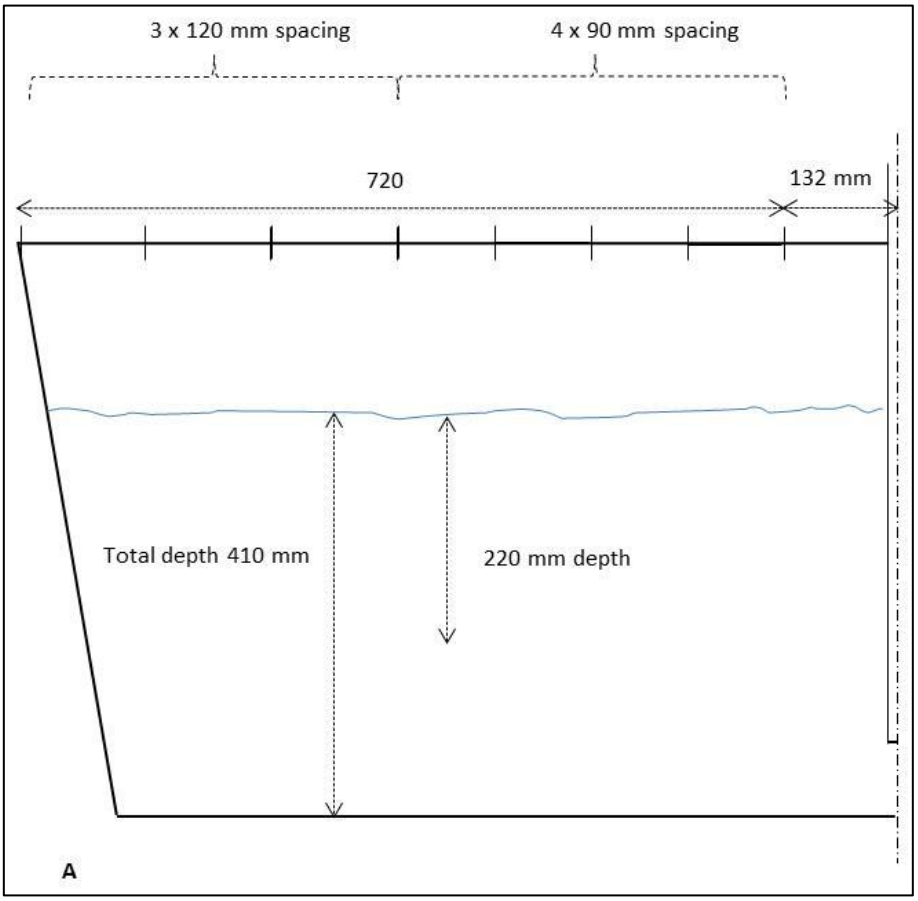

Figure 3-8 Transverse view of grid on top of the tundish, and sampling depth levels

It is important to note that 132 mm of sampling space close to the inlet is not accessible due to structural interference.

Sampling duration

Five repeats of each sampling point were taken over a period of 5 hours. The five repeats were averaged to give one value for the volume fraction of entrained paraffin.

It is worth mentioning that the residence time of the cold model is 8 minutes, and that the sampling method followed in this study mimicked a number of hits i.e. a number of ladles transferring melt to the tundish. The same procedure done in an actual industrial tundish.

Weather changes had a significant effect on the water density, thus sampling had to be done over steady weather conditions. In this study sampling all 42 locations was done over a week to account for weather changes, each day the density of water was measured by weighing 50 ml of water.

3.2.3 Flow characterisation study protocol

To provide a basis on which the physical model will be compared to the numerical model, a tracer study was performed. Five repeats of the RTD study were done. The following guidelines applied:

Steps in Section 3.2.1 were followed. When the system had stabilised (after 45 minutes), the tracer was injected into the model via the tracer injection point. 60 mL of 300 g/L table salt was used for these tests. The injection was done over 5 seconds.

After injecting the tracer, the concentration of the tracer in the outlet stream of two strands was monitored by making use of a calibrated conductivity meter. The concentration of the tracer was recorded at 30 second intervals for 20 minutes; this is more than twice the theoretical residence time of the model. Since there was one conductivity meter, the test had to be done twice. The first time was for the first strand and the second time for the second strand. Five repeats of each run were done.

4. PHYSICAL MODELLING RESULTS AND DISCUSSION

4.1 Observations

While running the physical model, it was noticed that there seemed to be little to no movement of the water-paraffin interface, which implies that there is no turbulence at the interface and that slag entrapment does not take place via turbulence at the interface.

There was no visual evidence of the paraffin entrainment as a result of shearing at the interface as was seen by other workers. Small droplets of entrained paraffin of approximately 1 mm could be seen floating even at low depths of 300 mm.

Initial measurements showed that a small amount of paraffin is entrained with an approximate maximum volume fraction of 0.02 even at depth of 220 mm. These observations suggest that the entrainment of the paraffin “slag” does not take place via macroscopic shearing of the interface but by microscopic entrainment possibly assisted by mass transfer at the steel-slag interface. By studying the interfacial velocities using the numerical model developed in this study, more insight will be gathered on this.

These observations also necessitate that the mesh be fine at the water-paraffin interface, possibly less than 1 mm. This is because the VOF model cannot resolve details at the interface smaller than the mesh size i.e. if the mesh is bigger than the smallest detail at the interface, the VOF model will overlook entrainment caused by microscopic shearing (Bakker, 2008).

It was also noted that as the pipette was being immersed in the paraffin layer and bulk water phase for sampling, a small amount of paraffin (simulated slag layer) and a mix of “entrained” paraffin and water from higher depths (<220 mm) in the bulk water phase tended to be forced into the pipette before a sample could be taken. This caused a high bias in the results. The bias resulting from the pipette going through the paraffin phase can be measured by sampling at the model at the 220 mm depth when there is no flow i.e. have the paraffin phase and water phase, close all the strand outlets, sample at 220 mm depth

with no flow entering the model. Thus this error can be eliminated (see Section 4.2). The error or bias resulting from the "entrained" paraffin and water mixture could not be measured. See the comparison between the numerical and physical model results for how much this error affected the results, Section 8.4.

4.2 Entrained slag behaviour

Figure 4-1 and Figure 4-2 show contour plots of entrained paraffin (slag) in a bare tundish and a tundish with FCD respectively. The zero on the x-axis represents the centre line where the inlet is located. The y-axis represents the length of the model. It is important to remember that 130 mm of sampling location was lost due to structural interference hence the y-axis starts at 200 mm.

To investigate the use of symmetry conditions along the longitudinal and transverse centre lines in the numerical model, a parity chart based on entrained "slag" concentrations was drawn, shown in Figure 4-3.

Figures 4-1 to Figure 4-3 should be looked at in conjunction with Figure 4-4 for orientation and explanation of what side 1 and side 2 mean. The values used to generate these plots can be found in Appendix B.

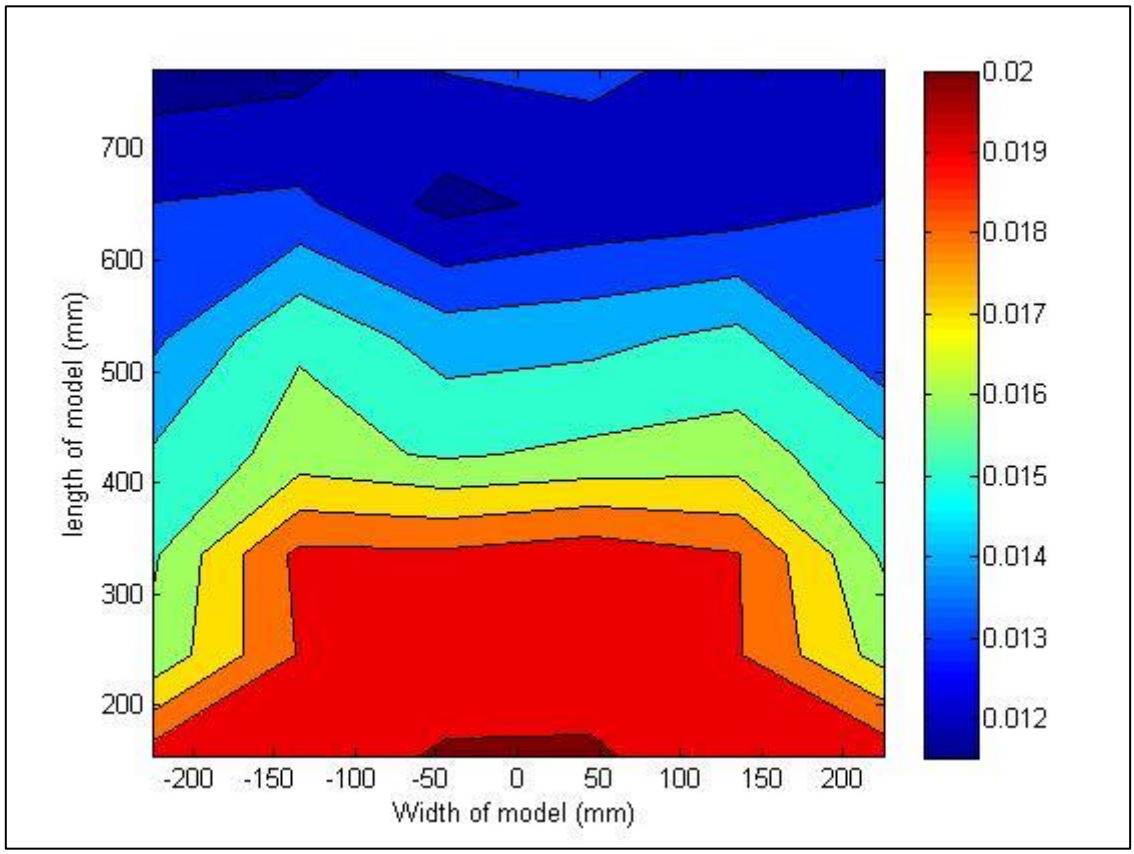

Figure 4-1 Top view of tundish showing contour plot of entrained "slag" concentration (volume fraction) at 220 mm depth in a bare tundish

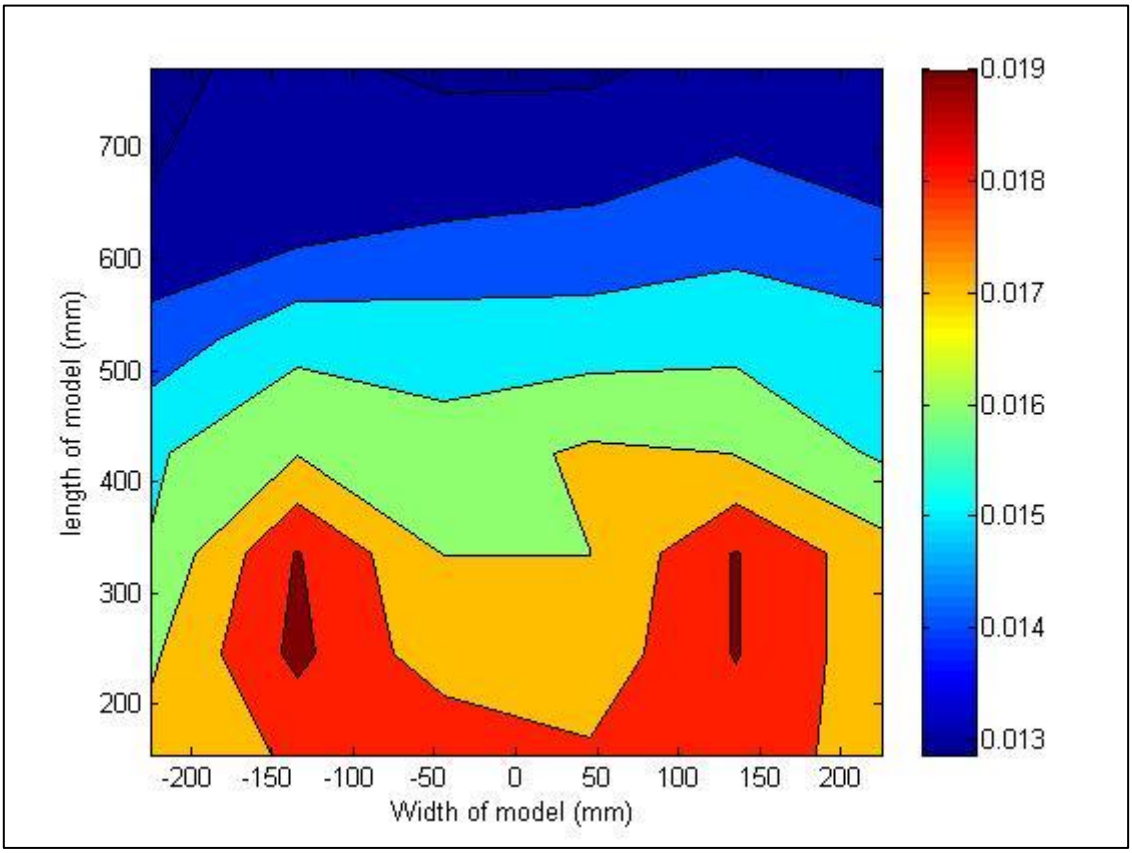

Figure 4-2 Top view of tundish showing contour plot of entrained "slag" concentration (volume fraction) at 220 mm depth in tundish with a FCD

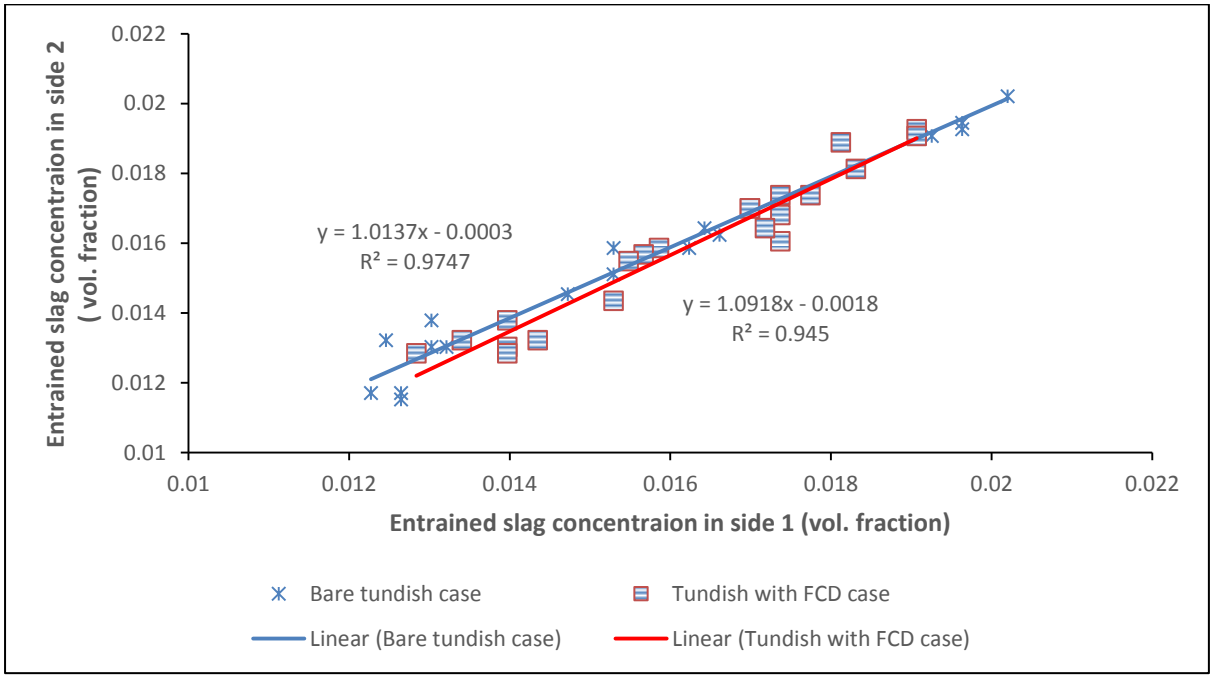

Figure 4-3 Parity chart of entrained "slag" concentration expressed as volume fraction

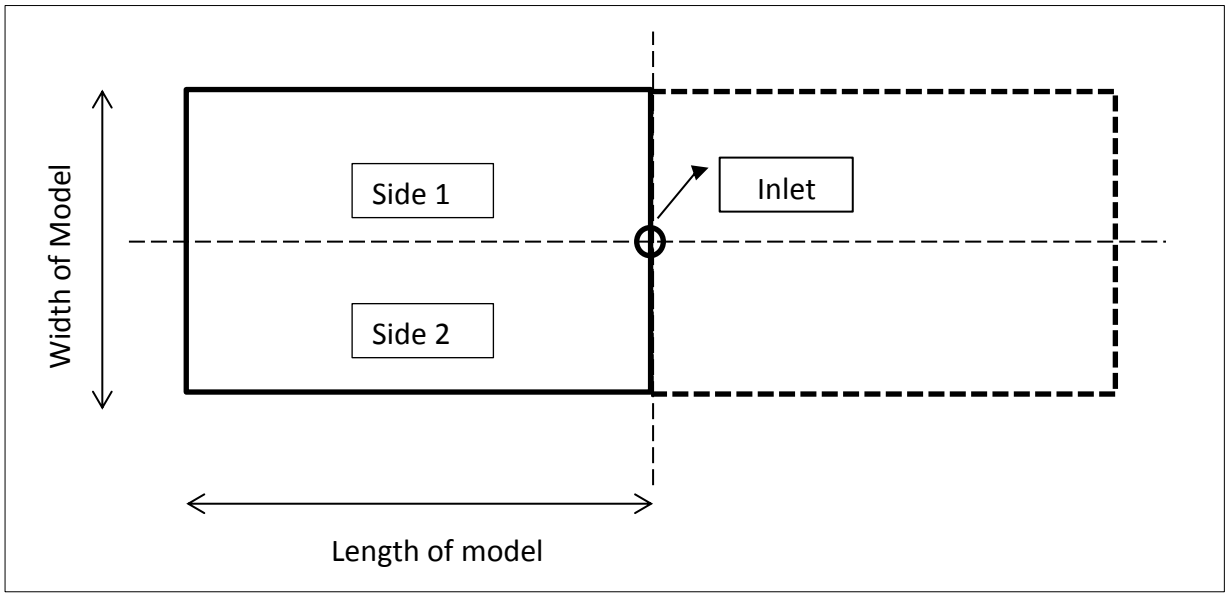

Figure 4-4 Top view of the tundish to explain of parity chart

From Figure 4-1 it can be seen that entrained slag in a bare tundish tends to accumulate in the region closest to the inlet. The concentration of entrained slag tends to decrease when approaching the end walls. This is a similar to findings made by Solhed *et al.* 2008. Interestingly a slightly similar pattern is seen in the tundish with a flow control device (Figure 4-2) however in the FCD device case, the entrained "slag" seems to appear in more localised pockets which form two parallel slits.

From the above parity charts, it can be seen that the concentration of entrained "slag" is indeed symmetrical about the longitudinal centre line. These results make it acceptable to numerically model only a quarter of the tundish and assume symmetry planes along the longitudinal and transverse centre line, instead of the full tundish. This saves a significant amount of computational time when solving the flow equations.

4.3 Error analysis for entrained slag behaviour

As noted in the observation, when the pipette was being immersed in the paraffin layer and bulk water phase for sampling, a small amount of paraffin (from the simulated slag layer) and a mix of "entrained" paraffin and water from higher depths (<220 mm) in the bulk water phase tended to be forced into the pipette due to hydrostatic pressure before a sample could be taken. This caused a high bias in the results shown in Section 4.2. To account for the bias resulting from the pipette going through the paraffin layer, ten blank samples (samples taken at 220 mm depth with no flow) were taken and the concentration of paraffin was measured. Table 4-1 shows the results from this test.

Table 4-1 Concentration of paraffin resulting from inherent error in sampling method

Sample No.	Paraffin volume fraction
1	0.0098
2	0.0089
3	0.0089
4	0.0098
5	0.0108
6	0.0108
7	0.0098
8	0.0108
9	0.0108
10	0.0089
Average	**0.0099**

Since this error in inherent throughout the model it can be subtracted from the data shown in Section 4.2 thus giving more accurate results. Figure 4-5 and Figure 4-6 show results with reduced inherent error. It is important to note that although further analysis will be done using these figures (Figure 4-5 and Figure 4-6), these results still contain a portion of the inherent sampling error and thus could be higher than the true concentration of the entrained paraffin. However, of importance to this study is the numerical model being able to predict the slag behaviour and the same magnitude of entrained paraffin concentration as in the physical model as opposed to the actual value entrained slag concentration.

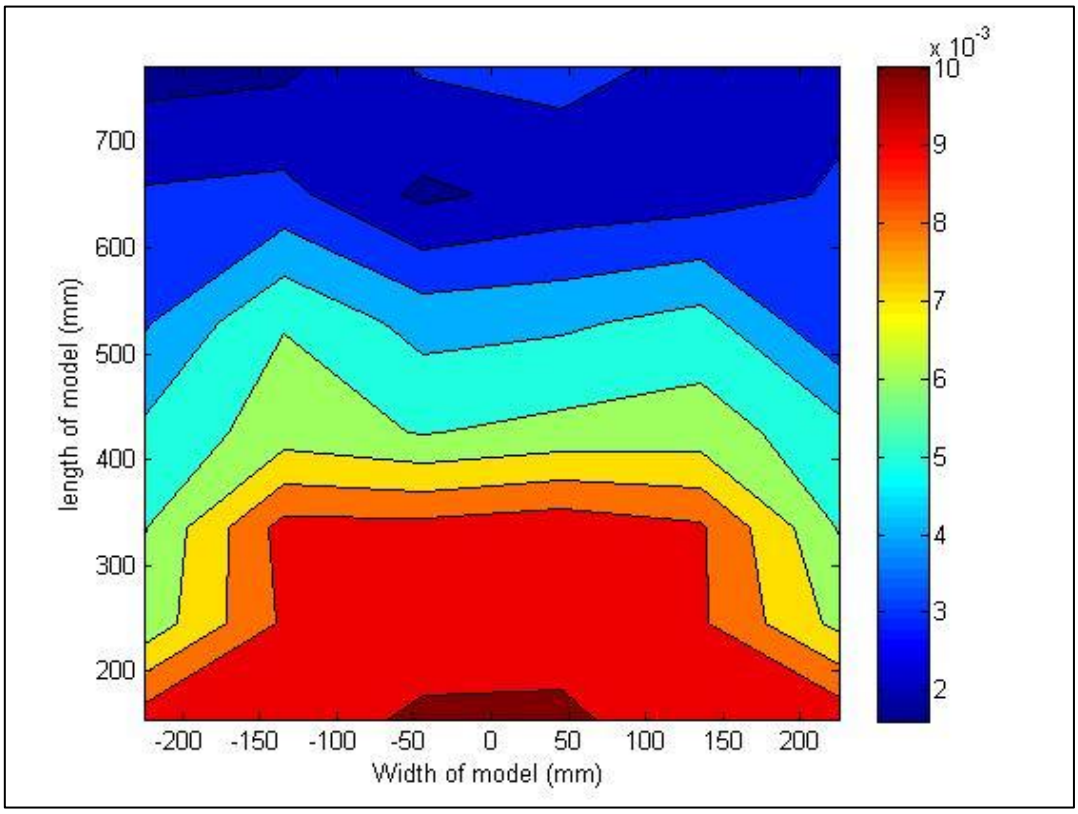

Figure 4-5 Top view of tundish showing adjusted contour plot of entrained "slag" concentration (volume fraction) at 220 mm depth in a bare tundish

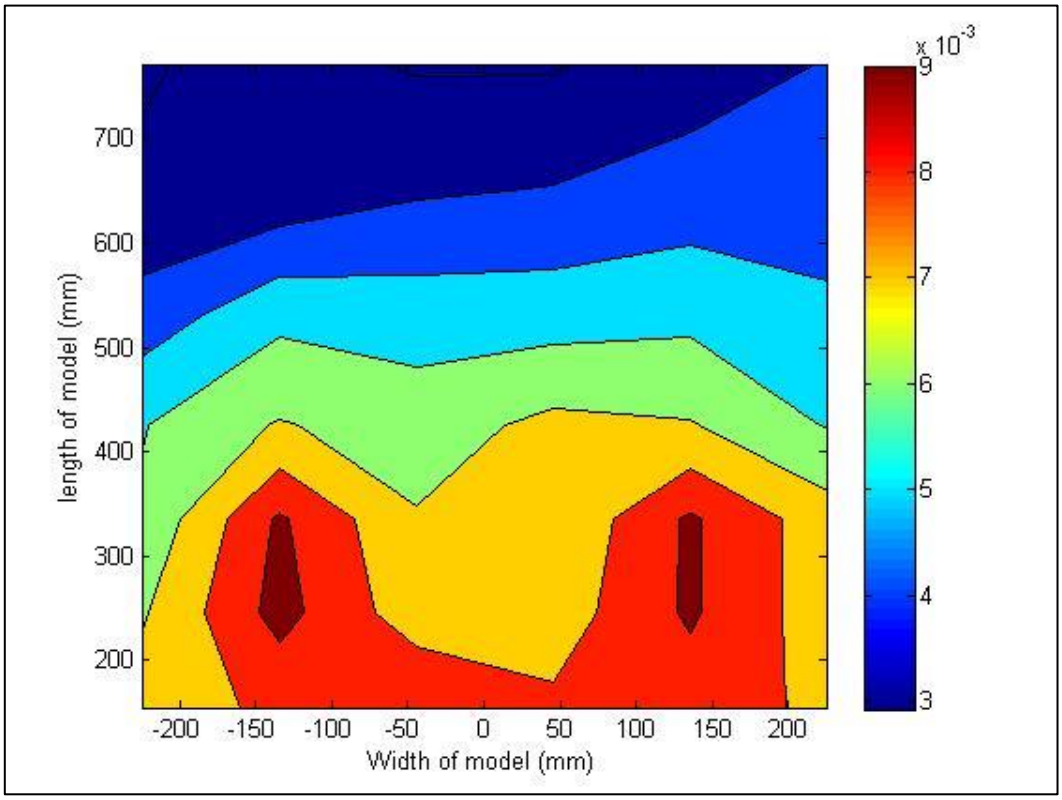

Figure 4-6 Top view of tundish showing adjusted contour plot of entrained "slag" concentration (volume fraction) at 220 mm depth in a tundish with FCD

4.4 Flow characterisation results

Figure 4-7 and Figure 4-8 below show the average residence time distributions in both the bare tundish and the tundish furnished with a flow control device.

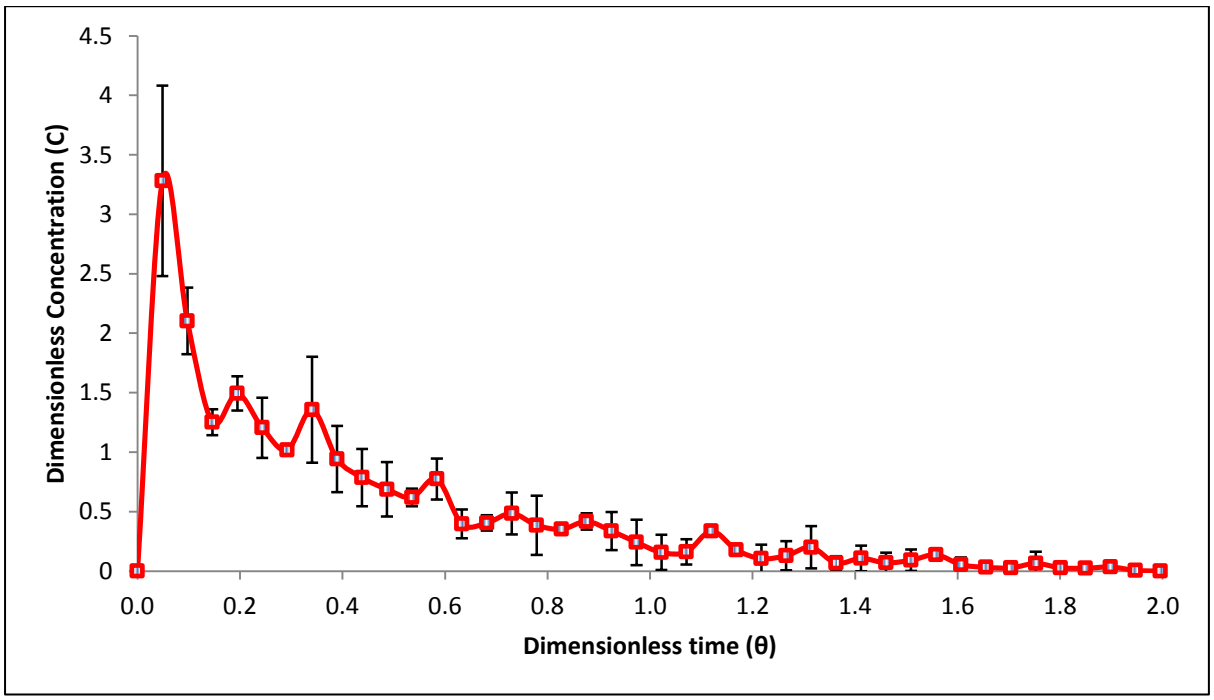

Figure 4-7 Residence time distribution of the bare tundish

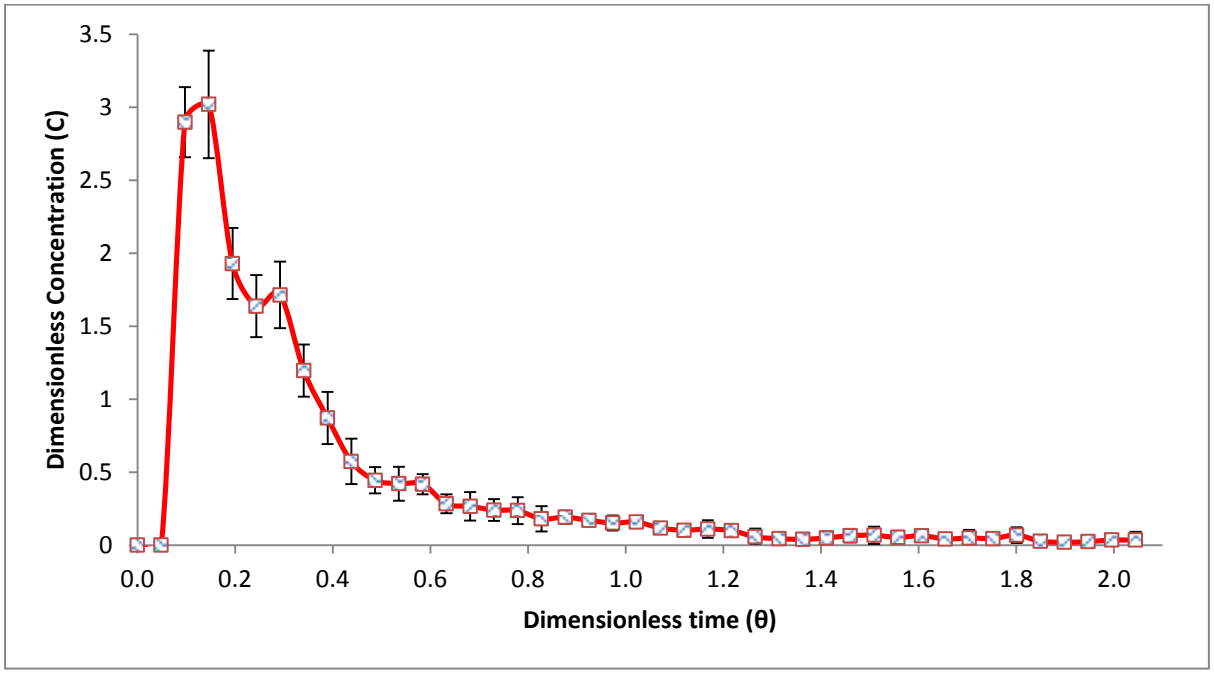

Figure 4-8 Residence time distribution of the tundish with a flow control device

The characteristic long tail of the RTD mentioned by Sahai *et al.* (1996) is evident in the above figures. Table 4-2 and Table 4-3 depict the numerical interpretation of the RTD study.

Table 4-2 Numerical interpretation of RTD in a bare tundish

Run	V_d	V_p	V_{mix}
1	0.483	0.122	0.396
2	0.565	0.122	0.313
3	0.577	0.146	0.277
4	0.636	0.122	0.243
5	0.564	0.146	0.290
Average	**0.565**	**0.131**	**0.30**
Standard deviation	**0.055**	**0.013**	**0.057**

Table 4-3 Numerical interpretation of RTD in a tundish with a flow control device

Run	V_d	V_p	V_{mix}
1	0.490	0.219	0.291
2	0.398	0.219	0.383
3	0.462	0.219	0.319
4	0.476	0.219	0.305
5	0.438	0.219	0.343
Average	**0.453**	**0.219**	**0.33**
Standard deviation	**0.036**	**0**	**0.036**

From Table 4-2, it can be seen that the bare tundish suffers from low plug flow volume fractions and high mixing volume fractions. After the introduction of a flow control device, the fraction of plug flow volume increased by 68 % whilst the volume fraction of dead zones decreased by 19 %. There

was no noticeable change in the mixing volume fraction. It is worth mentioning here that a portion of the dead volume fraction consists of the slag layer which cannot be varied by the installation of a flow control device.

5. NUMERICAL MODEL SET-UP

5.1 Geometry

Figure 5-1 and Figure 5-2 show the two geometries as drawn in ANSYS DesignModeler. The total bath level height in model is 410 mm, it was therefore decided to draw and model the tundish with a height of 410 mm. The inlet was taken to be just below the bottom of the ladle; this gave enough length for the velocity to form a profile before entering the tundish, as pointed out by Cloete (2014). It is worth noting that there is a possibility of decreasing cell count by modelling a shorter length of the inlet pipe, but this will not be explored in this study.

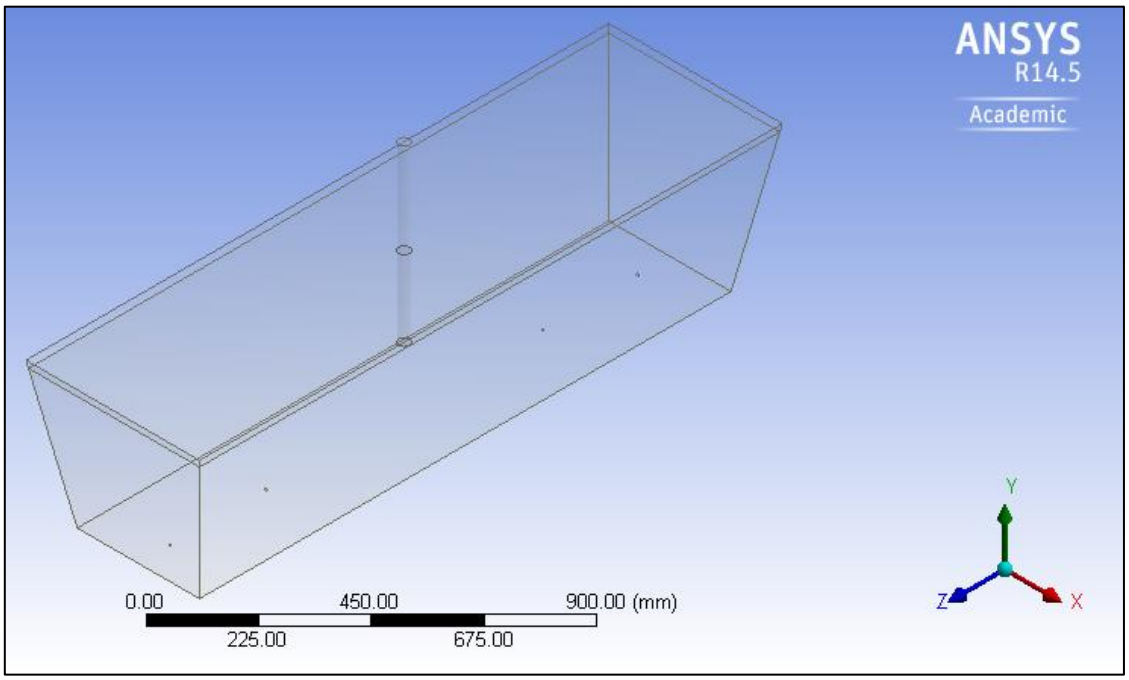

Figure 5-1 Geometry of a bare tundish

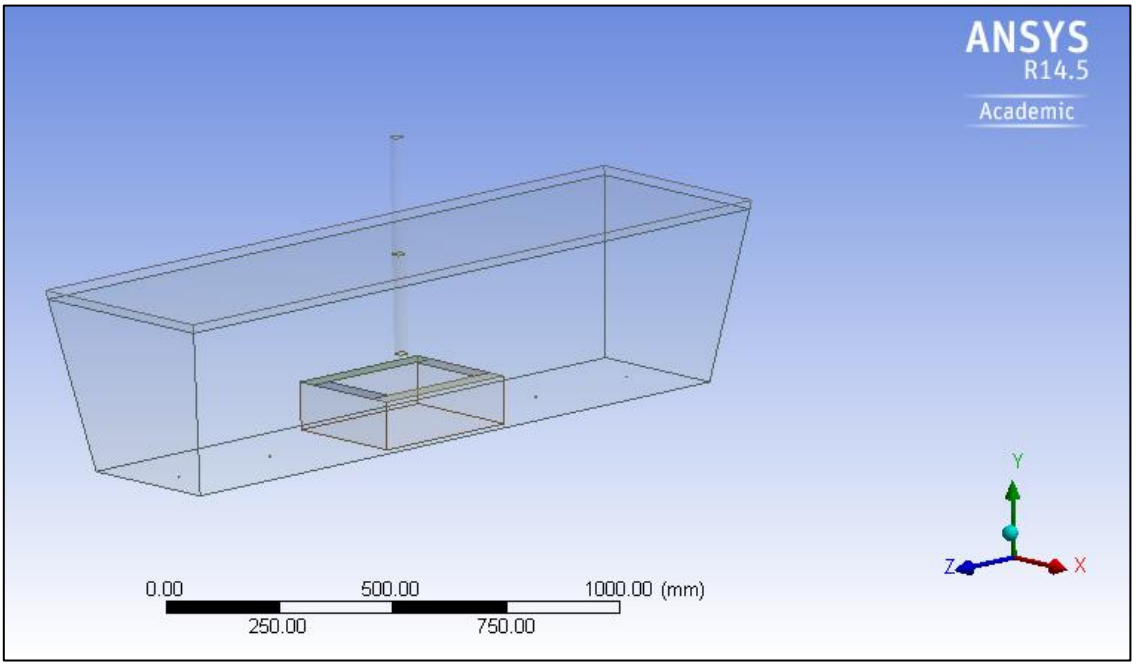

Figure 5-2 Geometry of tundish with a FCD

5.2 Geometry slicing and meshing

5.2.1 Geometry slicing

In order to use a hexagonal mesh the geometry had to be sliced in ANSYS DesignModeler. Figure 5-3 shows the modifications that need to be done in order to make the body sweepable. The modifications include:

- Creating a slice at the paraffin-water interface so as to create a new body
- Creating a slice where the inlet pipe ends
- Extruding the entry nozzle pipe to the bottom of the tundish using the slice method
- Extruding the four ports to the tundish top most surface using the slice method

Symmetry along the longitudinal and transverse planes was used.

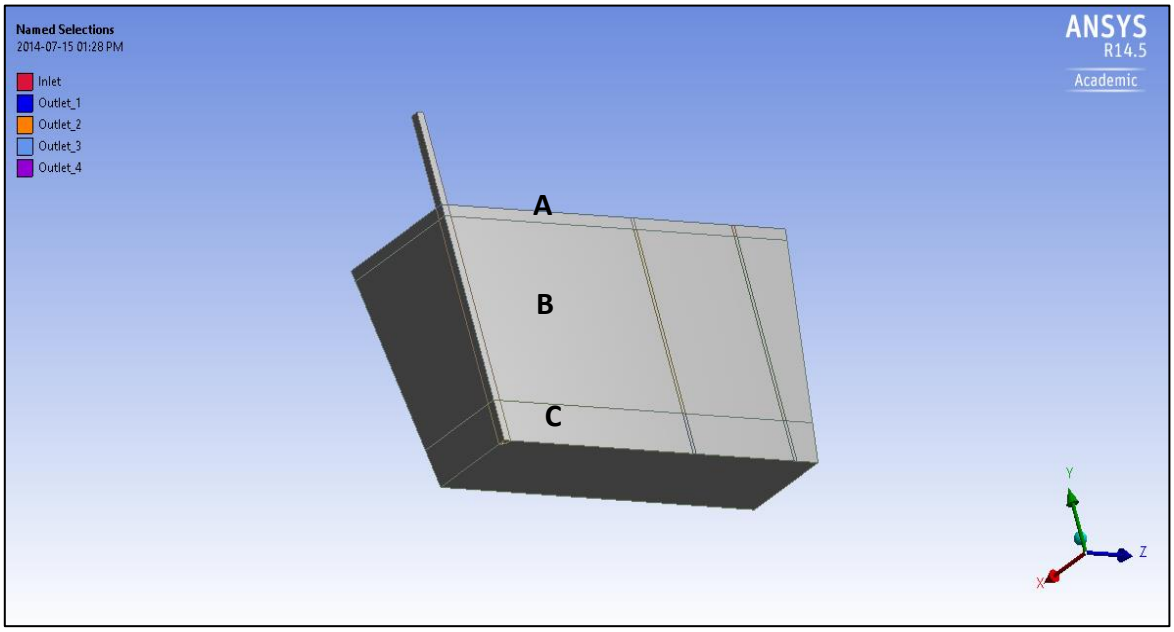

Figure 5-3 Geometry modification to accommodate hexagonal meshing (Drawn in ANSYS DesignModeler)

Meshing approach

The hexagonal mesh was installed as seen in Figure 5-4. The meshing steps included:

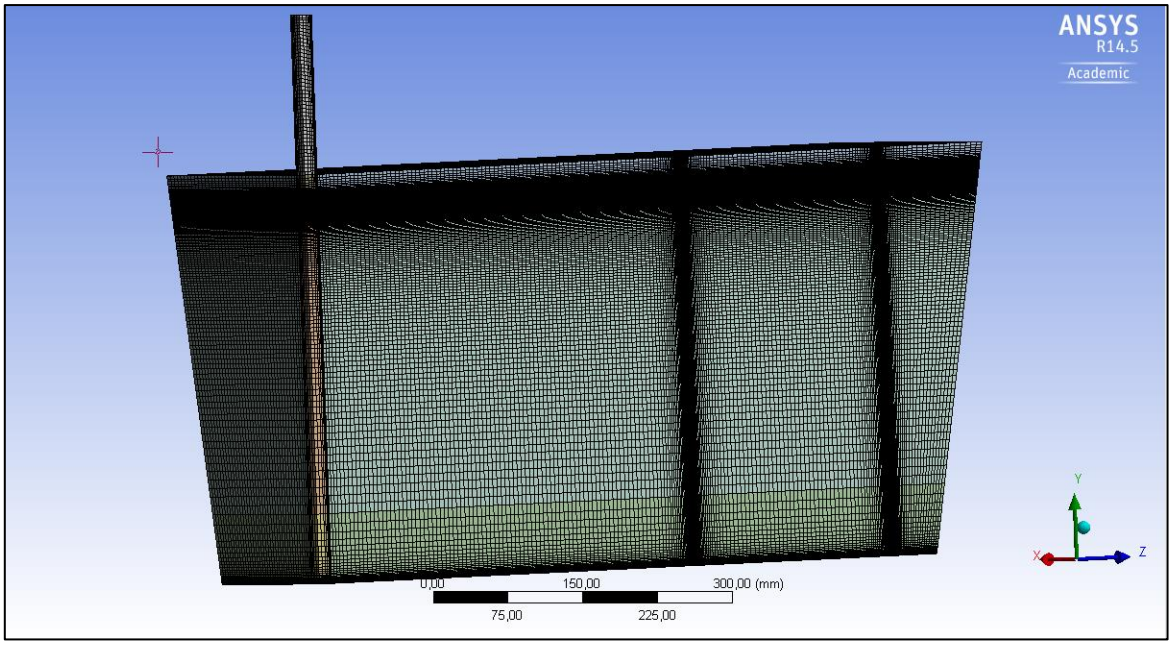

Figure 5-4 Hexagonal Mesh on tundish (taken from ANSYS Mesh Modeler)

- Installing hexagonal mesh with 30 divisions and a bias of 20 ranging from big to small in the paraffin region (Region A in Figure 5-3);
- Installing hexagonal mesh with an element size of 2 mm and a bias of 200 ranging from small to big in the water region below the paraffin layer (Region B in Figure 5-3);

- Installing hexagonal mesh in the lower part of the tundish to inflate the bottom of the tundish. The inflation was done by installing 2 mm size elements with a bias of 200 which reduces in size close to the bottom (Region C in Figure 5-3);
- Inflating the entry nozzle wall by specifying five layers with a growth rate of 1.2;
- A maximum face size of 10 mm was specified to control cell size;
- The relevance centre was left at 0 % to ensure that the hexagonal mesh was not distorted

It is quite obvious that the above mentioned mesh sizes have a significant influence on the accuracy of the numerical results. Thus they will become crucial when doing the mesh study (discussed in Section 6)

5.2.2 Fluent settings

In Fluent, the following settings were used:

General settings:

- The Explicit VOF model was used to model the two phases because the volume fraction of entrained paraffin fell below the 10 % volume fraction requirement for the mixture model furthermore the paraffin phase used in this study resembles free-surface flow of which the VOF model is suited for (ANSYS 2011) ;
- The Realizable k- ε equation was used with enhanced wall treatment as recommended by Bakker (2008). The Realizable k- ε is suitable for shear flow and local transitional zones as shown in Table 2-4. Shearing and transitional zones are expected to occur at the water-paraffin interface. Other more robust models such as RNG k- ε and Reynolds Stress Model could have been used, however these would have been hard to converge and would cost in terms of computational time.
- The operating density was specified as that of kerosene, 780 kg/m^3;
- Gravity was specified as 9.81 m/s;
- The surface tension between water and kerosene was specified as a constant of magnitude 0.048 N/m (Johansen 1924);
- The solution was run in full transient regime

Boundary conditions

- The velocity inlet was at the entry nozzle top, the velocity was specified as 0.614 m/s;
- The turbulence intensity was left as 5 % and the hydraulic diameter was specified as 30 mm;
- On the strand outlets, the settings were left as pressure based. The gauge pressure was left at 0 Pa and the turbulence intensity was left as 5 % , the hydraulic diameter was specified as 7 mm;
- Symmetry conditions were applied along the transverse and longitudinal plane of the tundish, thus reducing the computational domain to a quarter of the full scale model;

- The side walls, bottom of the tundish and FCD walls were specified as no slip conditions;
- The top surface has often been specified as a frictionless wall by researchers but it is important to note that in such studies, the researchers did not have a slag layer (Cloete 2014, Kumar *et al.* 2008, Mazumdar *et al.* 1999, Sahai *et al.* 1996, Tripathi *et al.* 2011). In this study the top surface layer was left as unspecified;
- No extra boundary conditions were specified at the interface since the continuity equation and momentum equations were naturally satisfied across the interface. The VOF also inherently specifies a balance of forces due to pressure difference across the interface and interfacial tension at the interface given by eq. 5-1 (Bakker 2008).

$$\Delta \boldsymbol{P} = \boldsymbol{\gamma}\left(\frac{\mathbf{1}}{\boldsymbol{R_x}} + \frac{\mathbf{1}}{\boldsymbol{R_y}}\right) \qquad 5\text{-}1$$

where:

ΔP - Pressure difference across the interface or top surface

$R_{x/y}$ - Radii of curvature in the each of the axes parallel to the top surface

Υ - Surface tension

Solver settings

- The pressure based solver was used. SIMPLE scheme was used for pressure-velocity calculations;
- All convective parameters were first interpolated using First Order upwind to stabilise the solution and later changed to second order upwind once the solutions had stabilised for better results;
- Volume fraction was solved using second order upwind throughout. This was chosen because it would give better results for the entrained paraffin concentration without being impacting negatively on the computational time and solution convergence;
- Gradients of solutions were evaluated using the Least-Square Cell-Based scheme. This was chosen to reduce false (numerical) diffusion. This was especially important at the water-paraffin interface where a sharp change in paraffin volume fraction occurs;
- The pressure was interpolated using the PRESTO! Scheme. This was found suitable since there is the a big change in pressure from the bottom of the tundish where the flow impacts on the rest of the tundish;
- The time step was initially left at 0.5 s

Solution initialisation

The solution was initialised from the inlet, and the rest of the tundish was assumed to be stagnant. A layer from 0 mm depth to 20 mm depth was patched with a paraffin volume fraction of 1 so as to simulate slag resting on top of the melt. The rest of the tundish was patched with a water volume fraction of 1.

6. NUMERICAL TESTS AND PRELIMINARY RESULTS

6.1 Set-up of numerical tests

A number of factors need to be fine-tuned in order to achieve a numerical model which can sufficiently resemble the numerical results whilst still maintaining economical computational time. Of most importance to this study are:

Symmetry

The tundish geometry presents a chance for symmetrical flow patterns about the longitudinal and transverse plane. Cloete (2014) physical experimental data on flow patterns suggest that the flow in the tundish is indeed symmetrical about the transverse and longitudinal plane of the tundish. A number of other authors have also assumed symmetrical flow patterns in symmetric tundishes but none of them have investigated the truth to this assumption (Jha *et al.* 2001, Jha *et al.* 2008, Tripathi *et al.* 2011, Tripathi *et al.* 2005).

Cell size

The maximum grid cell size is one of the most important parameters that contribute to the accuracy of the numerical model and the computational time needed by the model to converge. A numerical solution resulting from a non-refined mesh yields inaccurate results due to large cells or uneconomical computational times due to an unnecessary fine grid cells. To achieve a grid independent result, one has to manually refine the mesh until the solution does not change with change in grid size. Figure 6-1 shows the process which will be followed to achieve an independent solution.

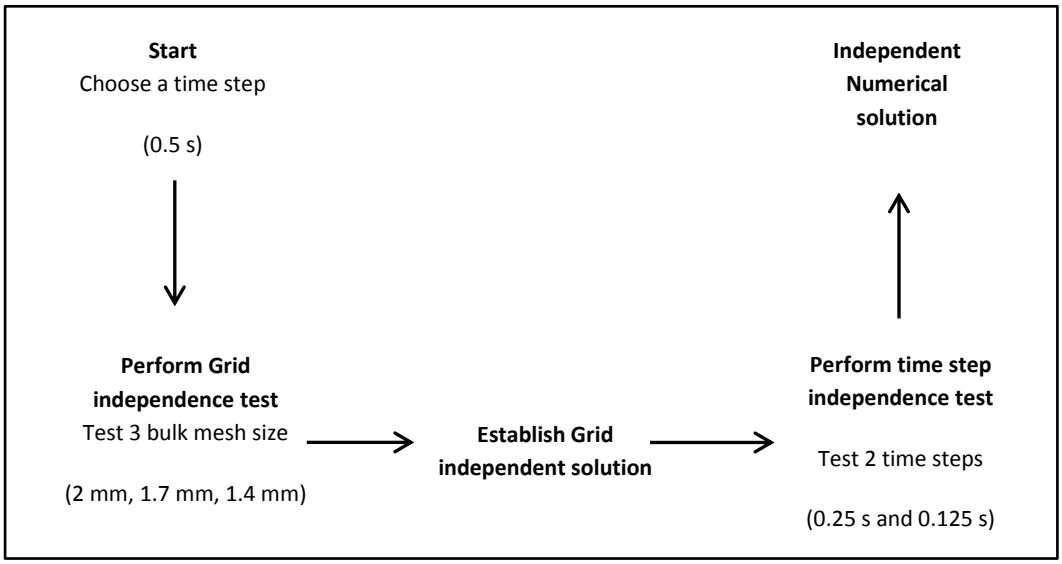

Figure 6-1 Flow chart process for independent numerical solution

The cell size will be varied from 2 mm to 1.7 mm and 1.4 mm to achieve a numerical model which can sufficiently replicate the physical modelling results. When varying the cell size, more emphasis will be placed on how well the model predicts the averaged flow patterns (average of 5 repeats). This is primary because the numerical entrainment will be heavily influence by the inflation at the water-paraffin interface, not by the bulk mesh size while the flow patterns will be influenced by the bulk mesh size. More over the entrainment is governed by the flow patterns therefore if the flow patterns are modelled well, then the entrainment ought to be also sufficiently modelled.

The inflation at the water-paraffin interface will not be varied. It is worth stating that it was found by trial and error that any divisions in the slag layer lower than 30 and a bias meshing lower than 200 in the bulk water phase leads to divergence of the solution.

Inflation at the inlet pipe will also not be varied; this decision is the result of based on work by Cloete (2014) who studied the effect of mesh size in the inlet pipe on the numerical RTD curve. He concluded that the mesh size, varied from 5 mm to 1 mm, has no effect on the flow patterns inside the tundish (Cloete 2014).

Step time

The time step setting in ANSYS Fluent allows the programme to segment the flow time into small time steps in which the flow equations are solved. The time step has to be small enough to converge the flow equations in each time step. Initially a time step of 0.5s will be used for the grid independent study, afterwards the time step will be varied from 0.5s to 0.25s and 0.125 s to see what effect this has on the results.

Convergence criteria

The numerical model was run until all residuals were stable below $1x10^{-4}$. This usually took 1.5 hours of flow time to achieve for both the bare tundish and the tundish with a flow control device. This took anywhere between 8 and 24 hours in real time using an HPC server with 4 to 16 processing cores.

6.2 Numerical modelling results

6.2.1 Grid independence

Figures 6-2 and 6-3 show the numerically predicted RTDs for a bare tundish and a tundish with a flow control device for the three different mesh sizes.

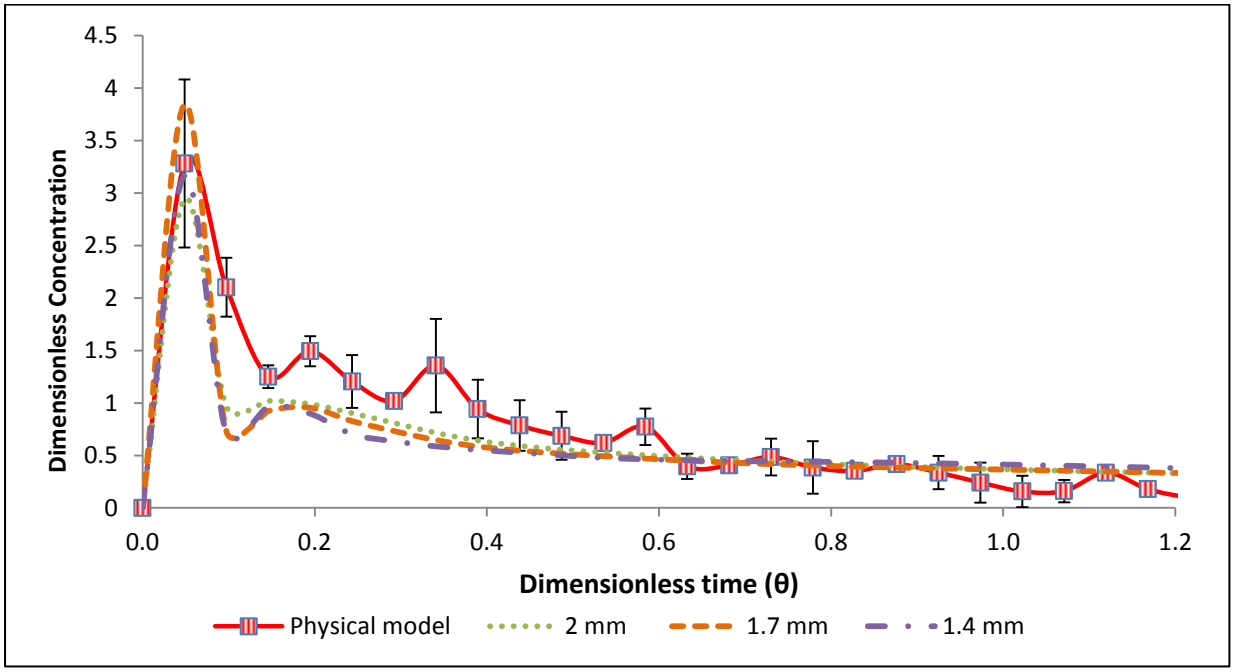

Figure 6-2 Numerically predicted RTDs vs. physical results RTD for a bare tundish at time step of 0.5 s

For the bare tundish, an accurate solution which can predict the flow patterns well was reached with a mesh size of 1.4 mm. This mesh size was used for a time step independent study.

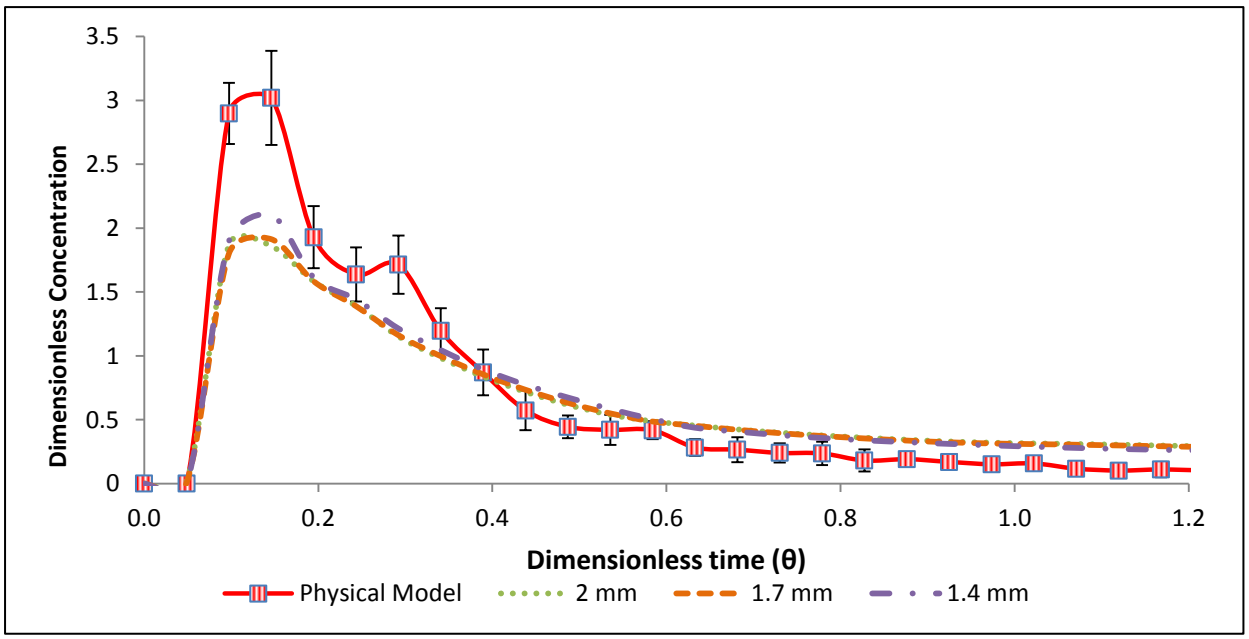

Figure 6-3 Numerically predicted RTDs vs. physical results RTD for a tundish with a FCD at time step of 0.5 s

In the case of the FCD, the numerically predicted RTD did not significantly change with change in mesh size i.e. the spread of the RTD, C_{max} and $\tau_{p,}$ were the same for all the mesh sizes considered. It is evident that the mesh size at the ranges considered has little effect on the RTD structure. The smaller 1.4 mm size mesh size should yield better results in the time step independent studies, and was thus used.

6.2.2 Time step independence study

Figure 6-4 and Figure 6-5 show the numerically predicted residence time plots for the two cases (bare tundish and tundish with a FCD) at the three time steps considered.

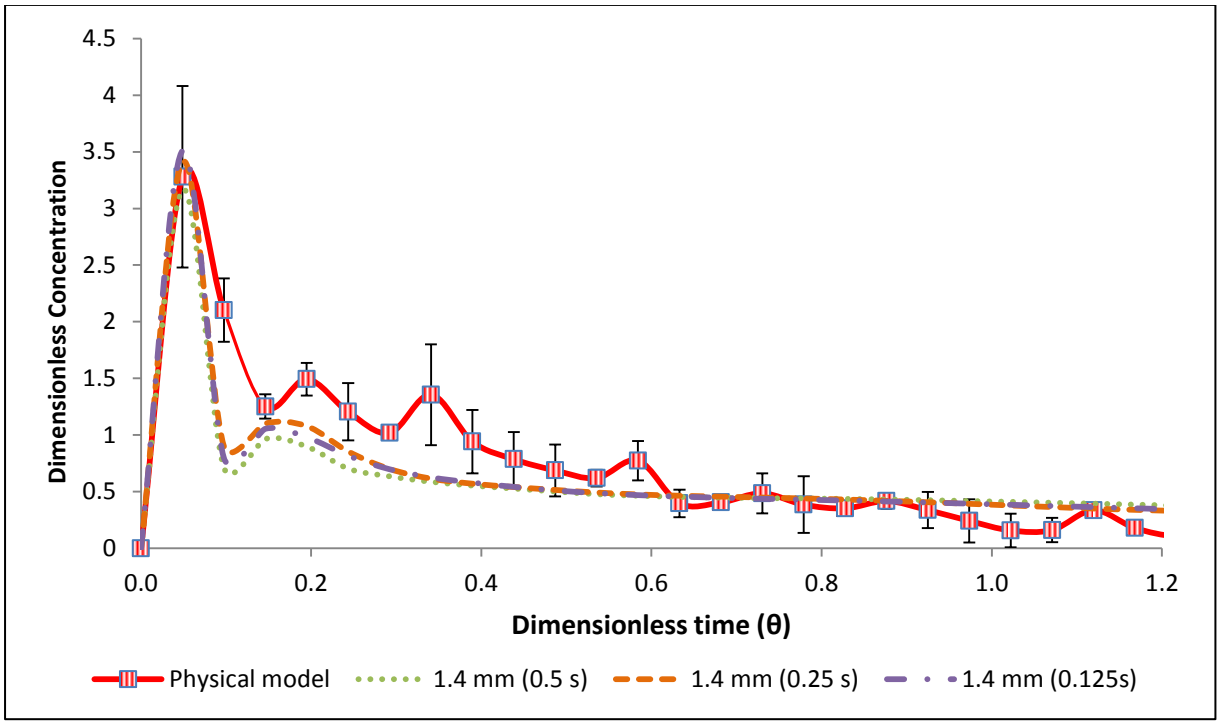

Figure 6-4 Numerically predicted RTD for a bare tundish at different time steps (0.5 s, 0.25 s, 0.125 s)

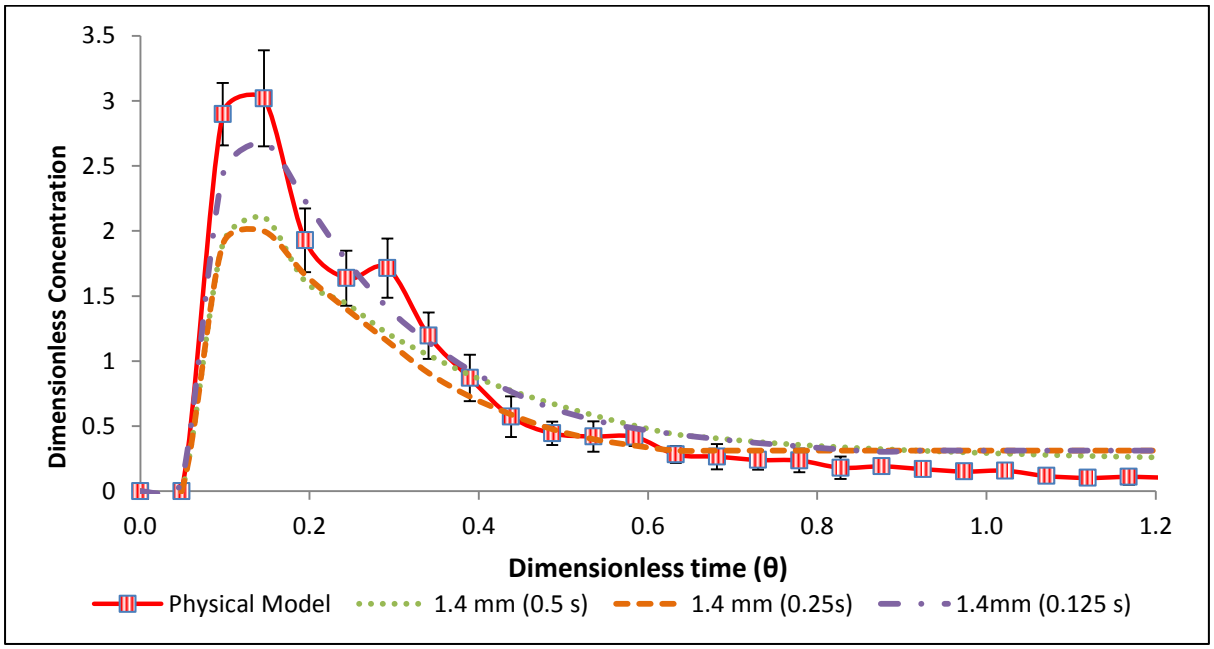

Figure 6-5 Numerically predicted RTD for tundish with FCD at different time steps (0. 5 s, 0.25 s, 0.125 s)

In the cases of both the bare tundish and the FCD, a match between the physical model and the numerical model was achieved with a mesh of 1.4 mm at a time step of 0.125s. It is quite interesting to note that the spread was numerically modelled well in the FCD case but

the details of the second peak were not. However in the bare tundish, the spread is not modelled well but the details of the second peak are captured well. Also it is interesting to see that the time step reduction had more effect on the accuracy of the numerical model than changing mesh sizes had. For further analysis, the 1.4 mm mesh size at a time step of 0.125 s will be used for analysis.

7. NUMERICALLY PREDICTED ENTRAINED SLAG BEHAVIOUR

Figure 7-1 and Figure 7-2 show contour plots of entrained paraffin concentration (slag) at a depth of 220 mm in a bare tundish and a tundish furnished with a FCD.

As in the physical model, the entrained slag concentration is highest behind the inlet shroud. The concentration of entrained slag tends to decrease towards the end walls. It is interesting to note that the concentration of entrained slag is lower in the case of the FCD than in the case of the bare tundish (38% lower, based on the highest entrained “slag” concentration). However this does not imply that less slag is entrained in the case of the FCD. Such a conclusion can only be made if the concentration of the entrained “slag” were to be measured at the strands for both cases. This was not done in this study due to the complexity of acquiring accurate results given the small concentration.

It is also interesting to note that the numerically entrained concentration is 55% and 68% lower than that found in the cold model for the bare tundish and tundish with FCD respectively. These above numbers are based on the highest recorded concentration, seen on the colour legend. This high bias in the cold model was noted in the observations. It results from fluid in shallower depths being pushed into the pipette as a result of hydrostatic pressure. It is important to note that an attempt was made to reduce this error and that the residual error as highlighted in Section 4.3. is what is causing the offset between numerical model and the cold model here. It is also important to note that the main concern of this study is to numerically model the entrained slag behaviour. By comparing the physical model results (Section 4.2) to the numerical model results, it can be seen that a numerical model which can predict entrained tundish slag behaviour in a bare tundish and tundish with a FCD was developed and thus this objective is met in this study.

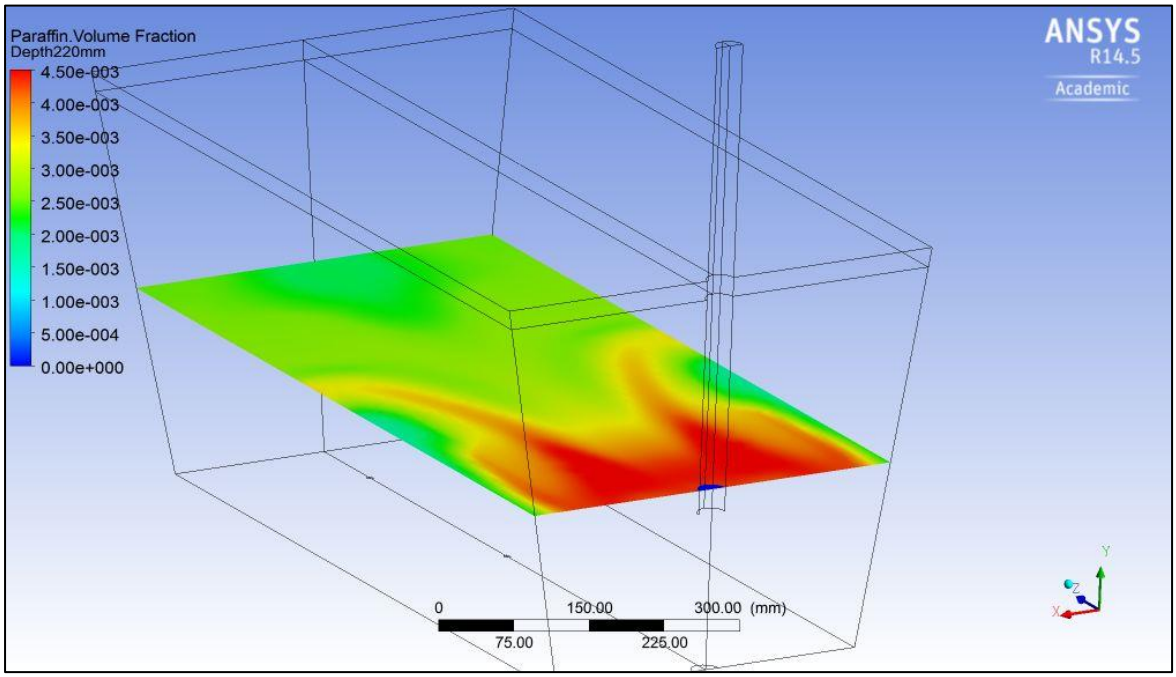

Figure 7-1 Contour plot of entrained paraffin "slag" in a bare tundish

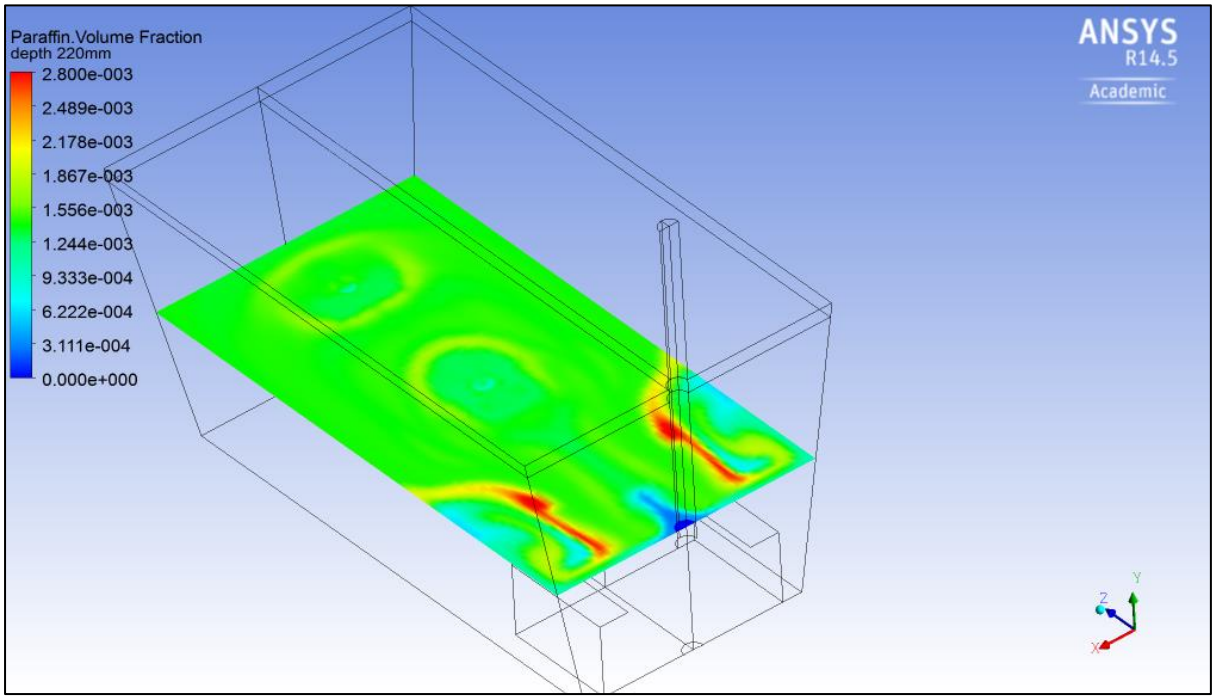

Figure 7-2 Contour plot of entrained paraffin “slag” in a tundish with a FCD

8. FLOW PATTERNS WHICH LEAD TO SLAG ENTRAINMENT

Having found a numerical model which can predict the slag entrainment and flow patterns in the tundish, it is worthwhile to study the flow patterns which lead to slag entrainment in both the bare tundish and the tundish with a flow control device.

8.1 Bare tundish flow patterns

Figure 8-1 and 8-2 depict the longitudinal view of the flow patterns in a bare tundish.

In Figure 8-1 it can be seen that the flow exits the inlet shroud, impinges at the bottom of the tundish and reports to the inner strand. The displacement of the melt at the bottom of the tundish causes a draft of melt from the outer walls of the tundish (Region A). In this view it can be seen that there is no excessive tangential flow close to the steel-slag interface. Thus the entrainment does not arise from longitudinally directed flow. In Figure 8-2 a downward directed flow from the side walls can be seen (Region B). See also Figure 8-3 to Figure 8-5.

Figure 8-3 and Figure 8-4 depict the flow patterns in transverse view. The flow impinges at the bottom of the tundish, and then moves up the sidewalls to cause shearing below the steel-slag interface (Region C). It is this flow being assisted by mass transfer at the interface that in this study is believed to contribute to slag entrainment in bare tundishes.

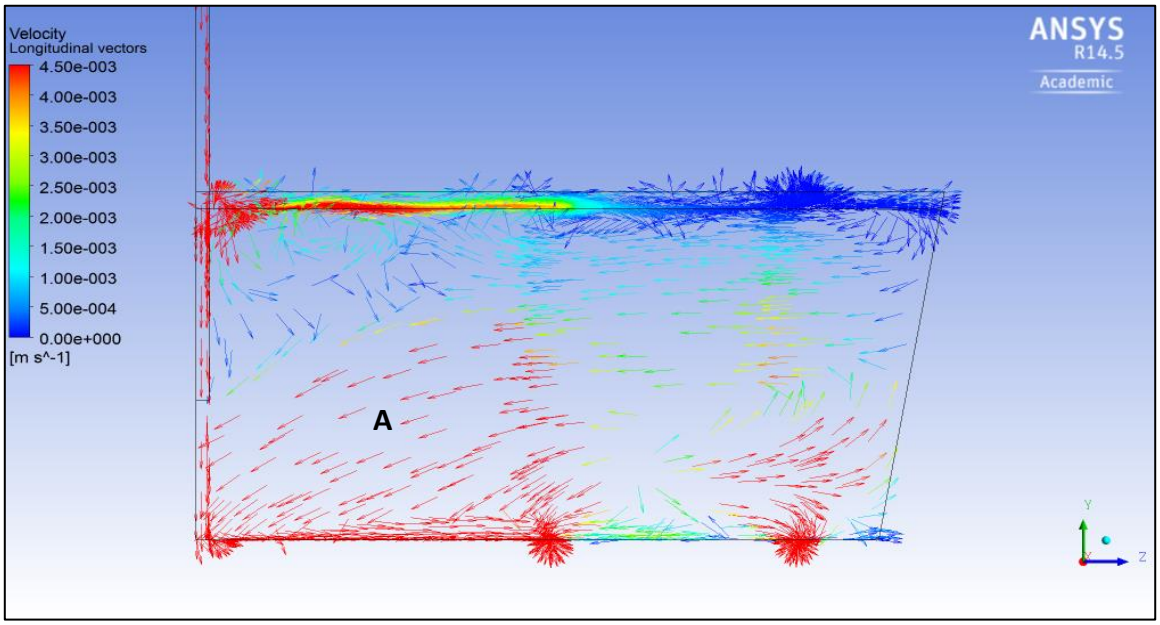

Figure 8-1 Longitudinal view of flow vectors at the centreline of a bare tundish

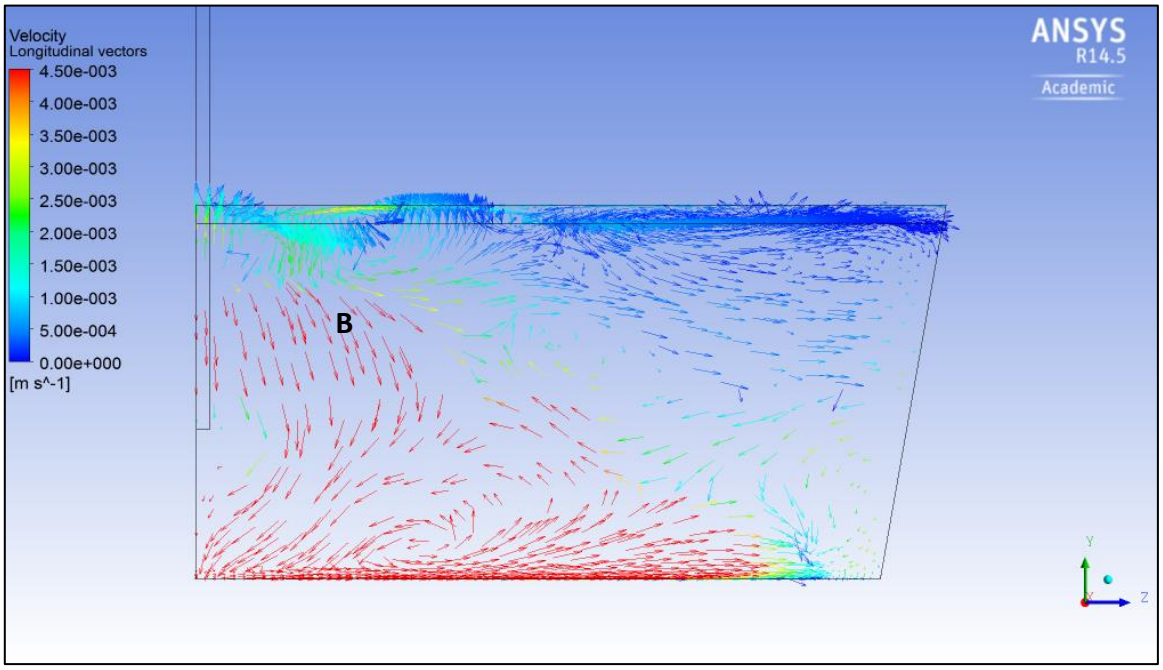

Figure 8-2 Longitudinal view of flow vectors at 100 mm from the centreline in a bare tundish

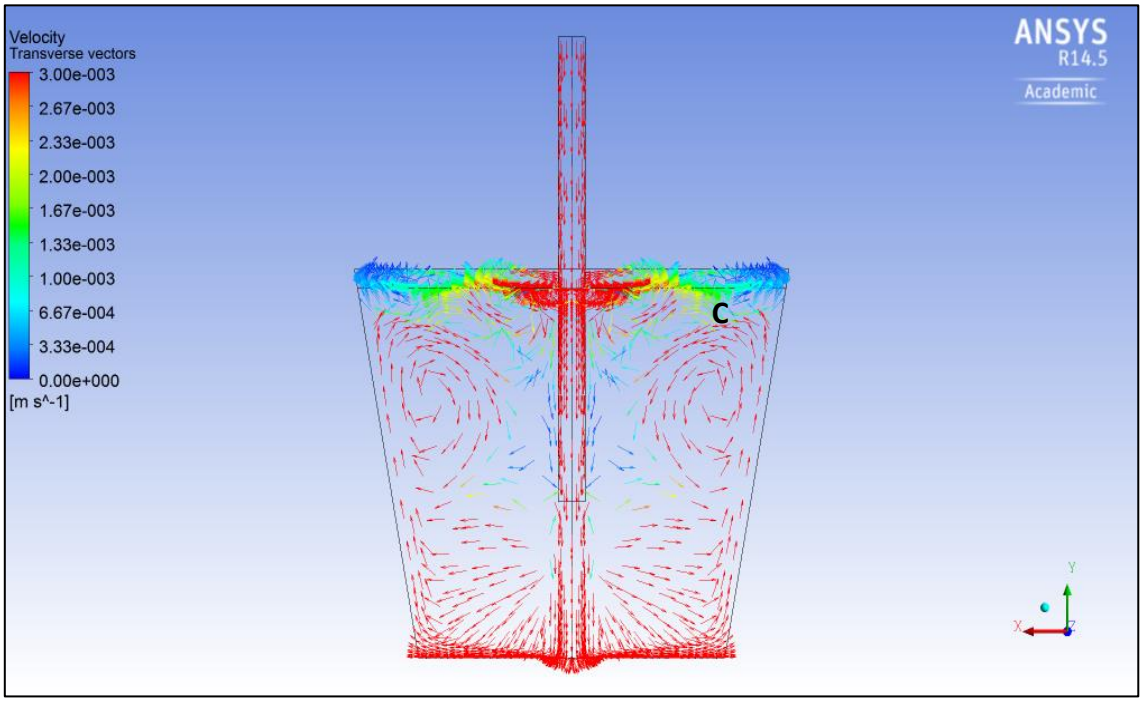

Figure 8-3 Transverse view of flow vectors at the centreline in a bare tundish

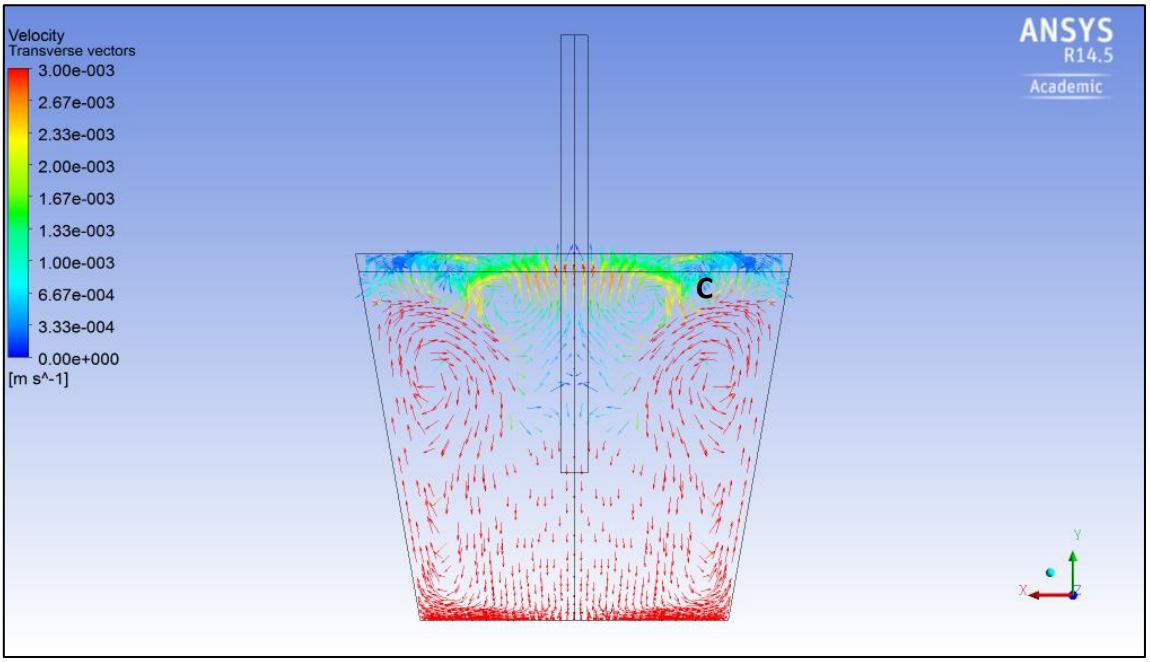

Figure 8-4 Transverse view of flow vectors at 100 mm from the centre line

Figure 8-5 and Figure 8-6 show the flow patterns in the transverse plane superimposed on a contour plot of entrained paraffin “slag” concentration at a depth of 220 mm.

It can be seen that the areas of high paraffin (slag) concentration are the areas where the flow which impinged on the bottom of the tundish falls on itself (Region D). The entrained slag is then carried by the flow down until the flow turns into itself in Region D. As the flow

which rises up the sidewalls fades, less slag is seen in the steel phase in Region E (see Figure 8-6)

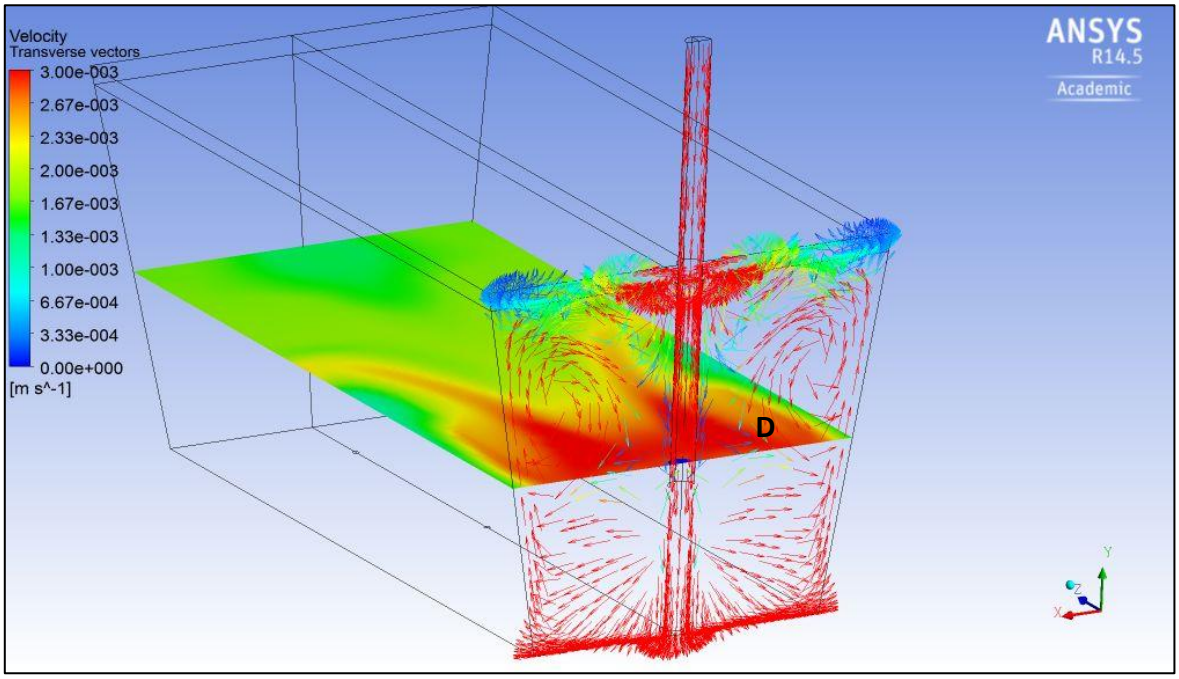

Figure 8-5 Transverse flow vectors at the centre line superimposed with entrained slag concentration at a depth of 220 mm.

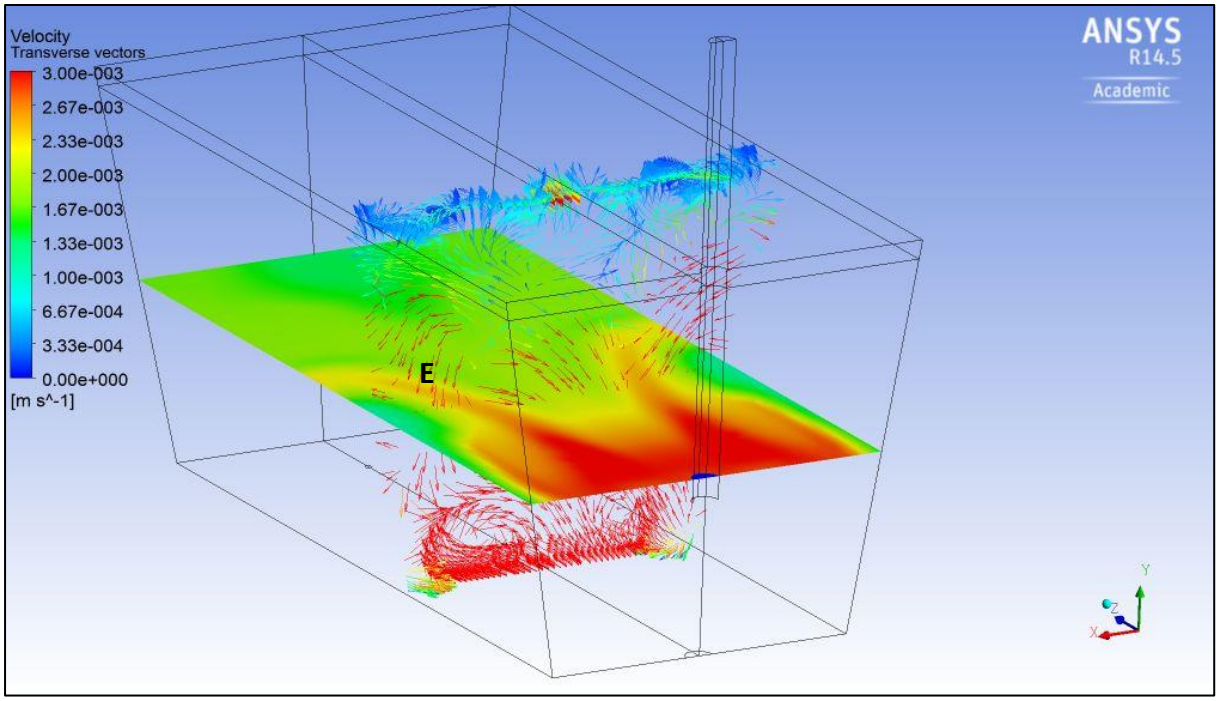

Figure 8-6 Transverse flow vectors at 300 mm from the centreline superimposed with entrained slag concentration at a depth of 220 mm.

8.2 Flow patterns in Tundish with a FCD

Figure 8-7 and Figure 8-8 show longitudinal flow patterns in a tundish with a FCD. The flow exits the inlet shroud and is immediately directed to the steel-slag interface by the FCD as intended (Region F). There are two clear vortexes above the inner and outer strand that did not show in previous studies such as Cloete (2014) and Kumar *et al.* 2008. These vortexes do not extrude to the top of the slag layer possibly due to the viscous of the paraffin (slag) layer (Region G and H).

Similarly to the bare tundish case, the displacement of fluid close to the inlet region causes flow to the inlet region from nearby areas (Region I).

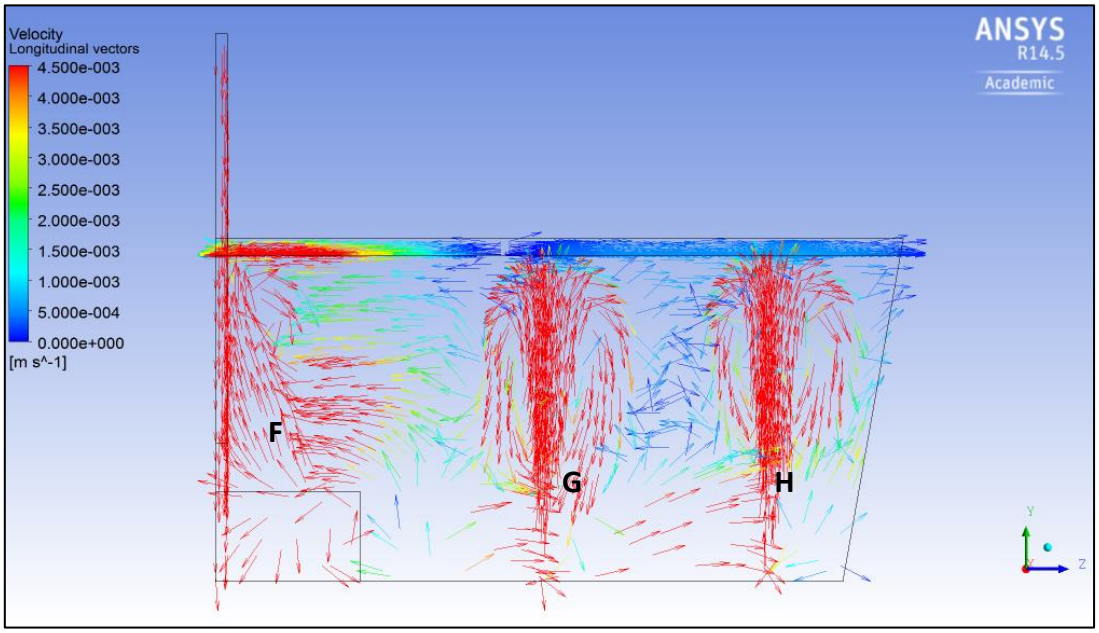

Figure 8-7 Longitudinal view of flow vectors in a tundish FCD

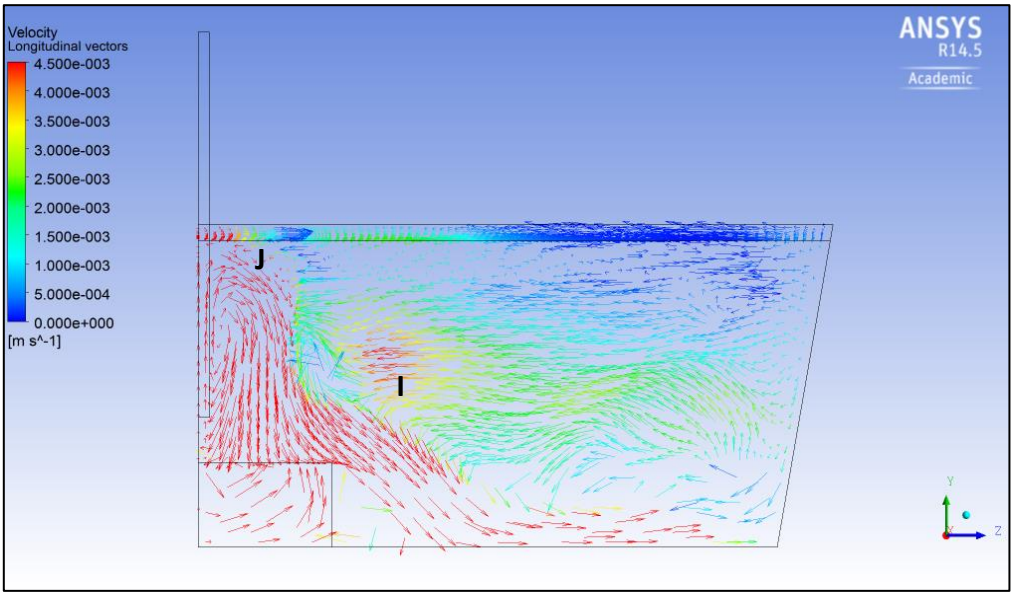

Figure 8-8 Longitudinal view of flow vectors 120 mm away from the centre line

The transverse view (Figure 8-9) shows that most of the flow exiting from the inlet shroud is reflected from the bottom of the tundish and directed to the slag layer, as intended. This flow then impinges on the slag layer where it results in tangential flow to the slag layer (Region J). This tangential flow can even be seen in Figure 8-8. It is quite interesting to note that almost a similar tangential flow in the bare tundish is created by the presence of the FCD, the only difference being that in the FCD case, the flow is from inside going out to the side walls whereas in the bare tundish case it is from the side walls going towards the inlet region. It is possible that the entrainment first takes place in Region J where the flow is tangential to the interface.

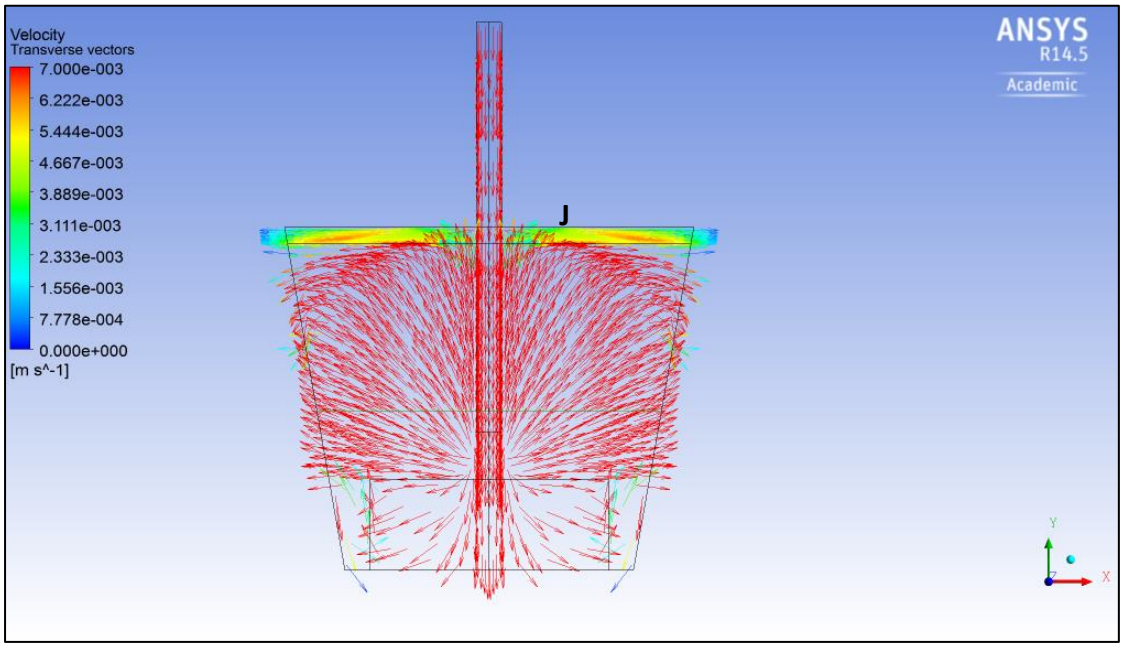

Figure 8-9 Transverse view of flow vectors in a tundish with FCD

Figure 8-10 shows the flow patterns in the vertical plane 120 mm away from the centre line superimposed on the entrained paraffin “slag” concentration at a depth of 220 mm. From this figure it is evident that the entrained “slag” from area J moves with the prevailing flow to accumulate in Region K. Because there is less entrained paraffin in other regions, it can be concluded that the entrainment or shearing takes place at Region J.

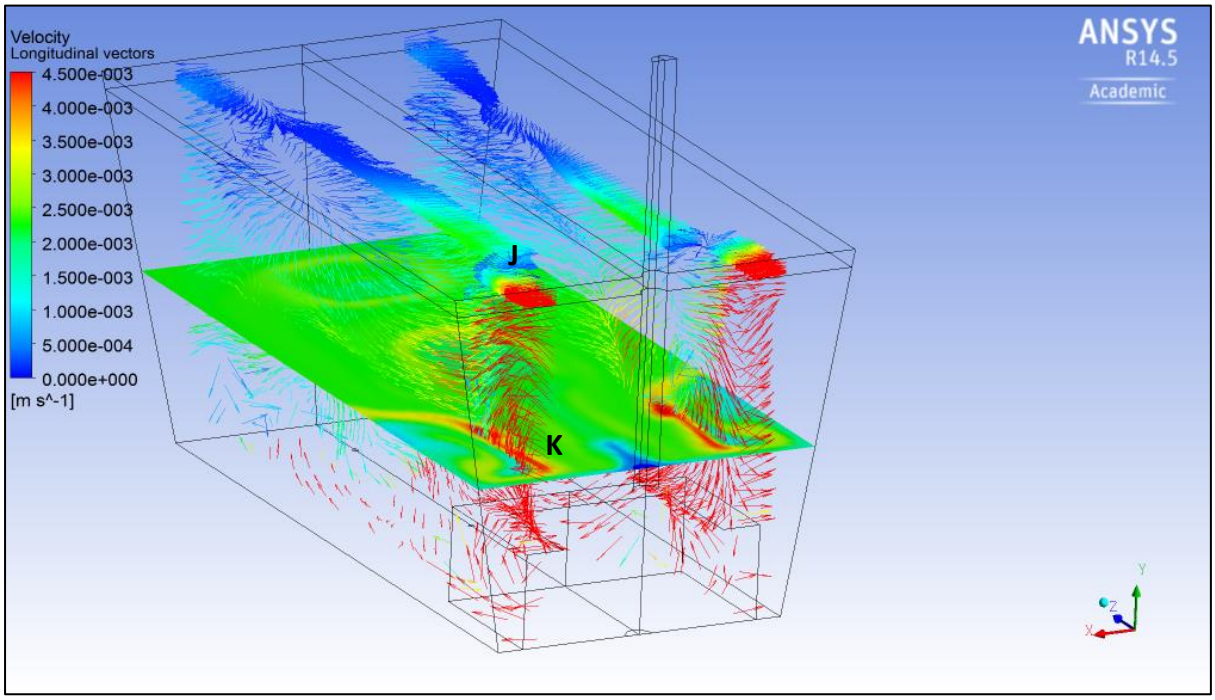

Figure 8-10 Longitudinal flow vectors at 120 mm away from the centre line superimposed on entrained slag concentration at a depth of 220 mm.

8.3 Slag entrainment mechanisms in a bare tundish

To understand the main mechanism behind slag entrainment in tundishes it is important to understand the magnitude of critical velocities at which the slag entrainment takes place and then compare these to the numerical simulated interfacial velocities.

Table 2-11 in the literature review summary showed the various slag entrainment mechanisms, their criteria for entrainment and the calculated critical velocities for the water-paraffin case used in this study. From the table it can be seen that the critical velocities for slag entrainment in the water model range from 1.34 x 10^{-1} to 9.44 x 10^{-1} m/s.

Figure 8-11 to 8-13 show velocity vectors tangential to the water-paraffin interface (steel-slag interface). In Figure 8-11 and Figure 8-12 it can be seen that there are no clear tangential velocities even at 10 mm below the interface, however in Figure 8-13 one can see relatively high velocity vectors tangential to the interface. The highest of these vectors is 3 x 10^{-3} m/s. This is significantly lower than the velocities calculated for macroscopic shearing methods considered in the literature review.

Furthermore, the lack of tangential velocities directly at the interface suggests that the paraffin initially moved by mass transfer across the interface and that shearing only occurs at a depth of 50 mm.

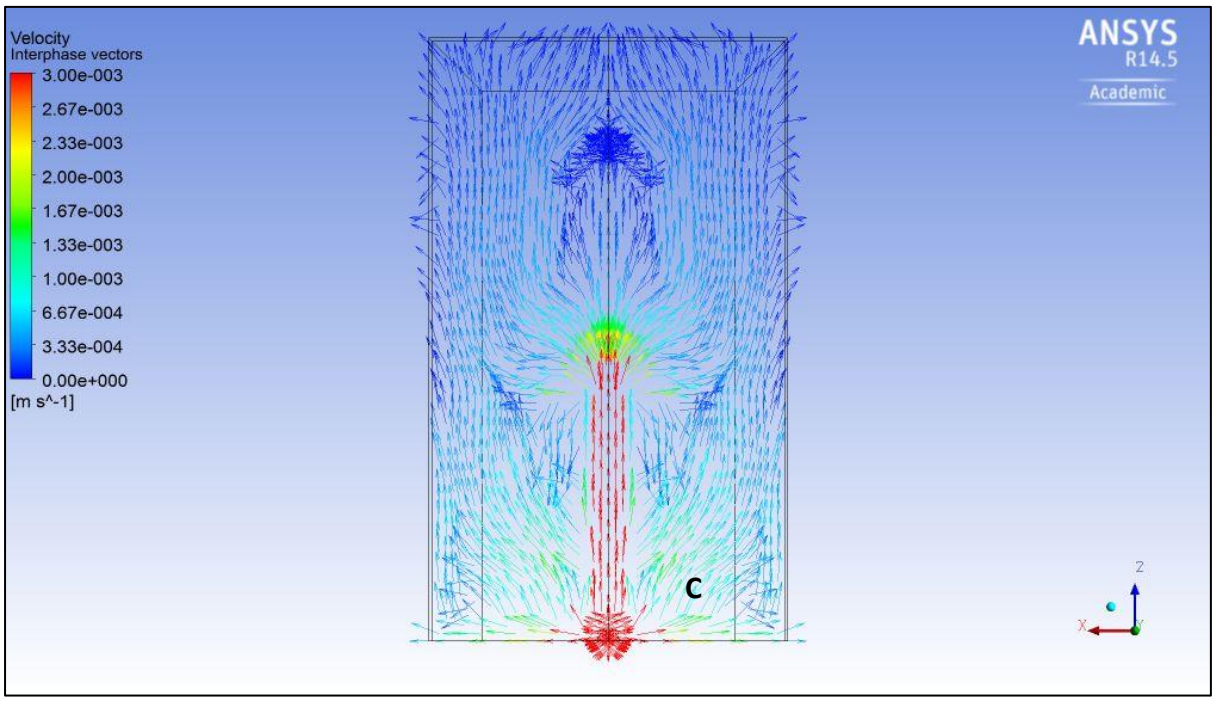

Figure 8-11 Tangential velocity vectors at the water-paraffin (steel-slag) interface in a bare tundish

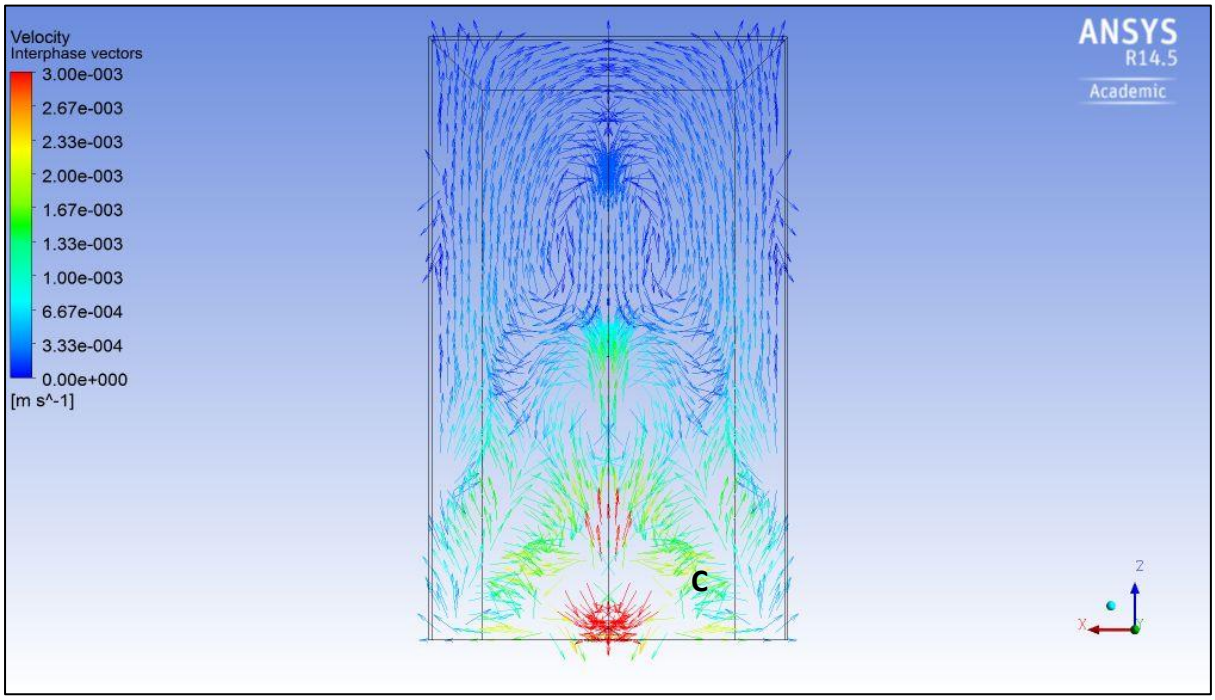

Figure 8-12 Tangential velocity vectors 10 mm below the interface in a bare tundish

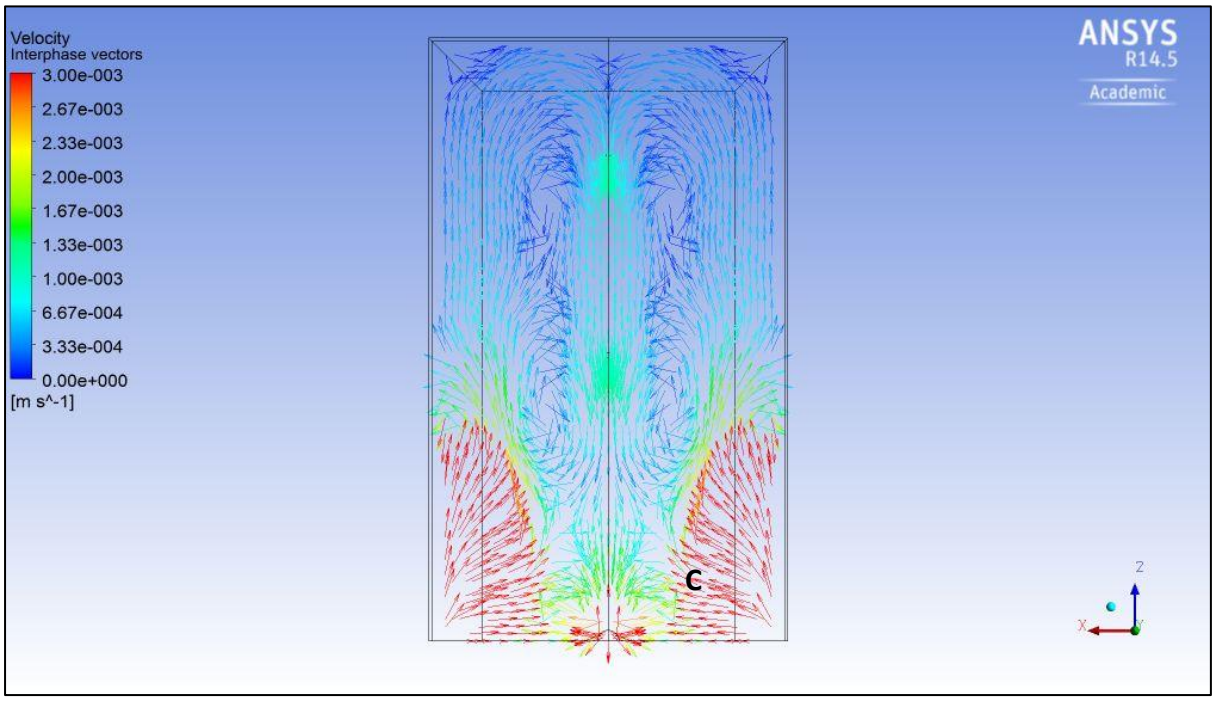

Figure 8-13 Tangential velocity vectors 50 mm below the interface in a bare tundish

8.4 Slag entrainment mechanism in a tundish with a FCD

Figure 8-14 to Figure 8-16 depict tangential velocity vectors to the interface at varying depths. It can be seen from these figures that even at just below the interface, high tangential velocities exist (highest is 6 x10^{-3} m/s). However, none of these velocity vectors pass the threshold of 1.34 x 10^{-1} m/s. This provides proof that the entrainment in a tundish with a FCD also does not take place via the macroscopic methods considered in this study

but perhaps takes place via mass transfer across the interface, assisted by small velocity shearing close to the interface.

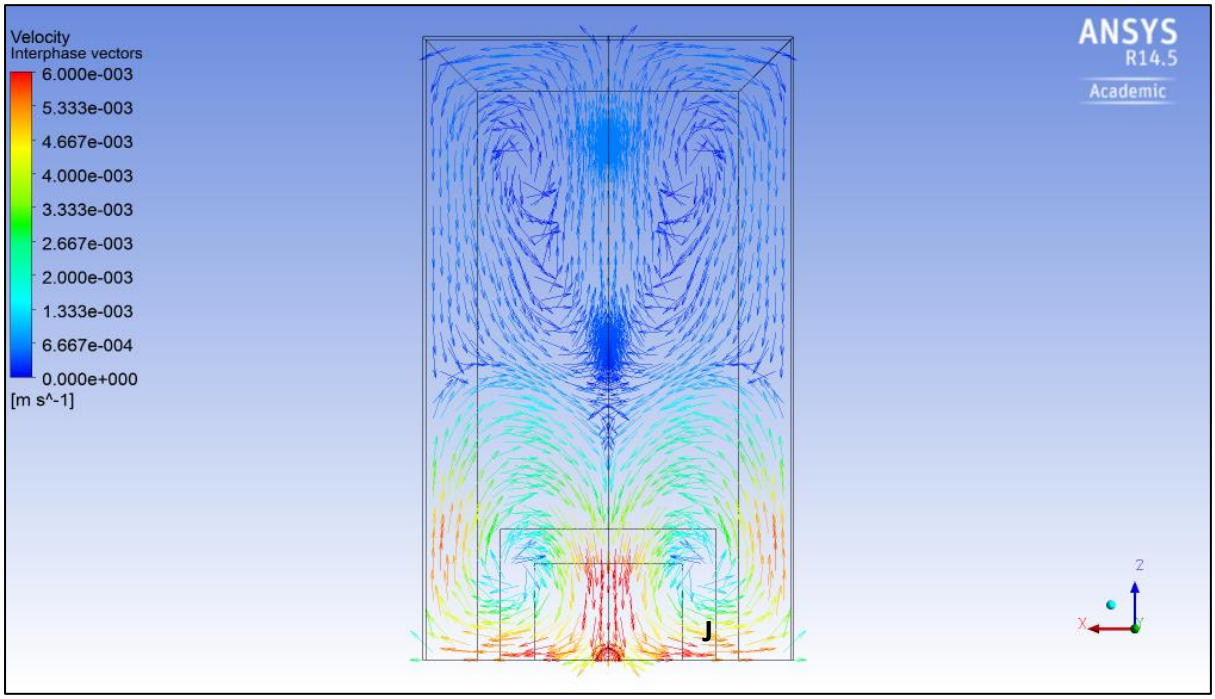

Figure 8-14 Tangential flow to the interface at 0 mm depth in the case of FCD.

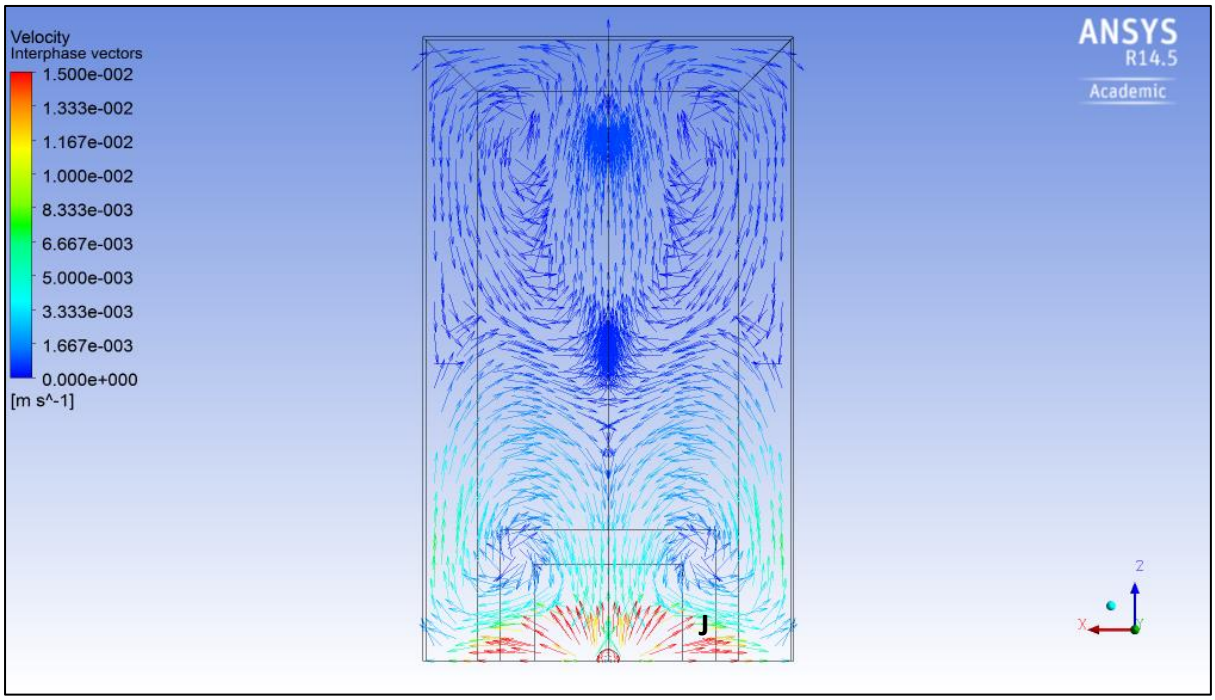

Figure 8-15 Tangential flow to the interface at a depth of 10 mm in the case of FCD

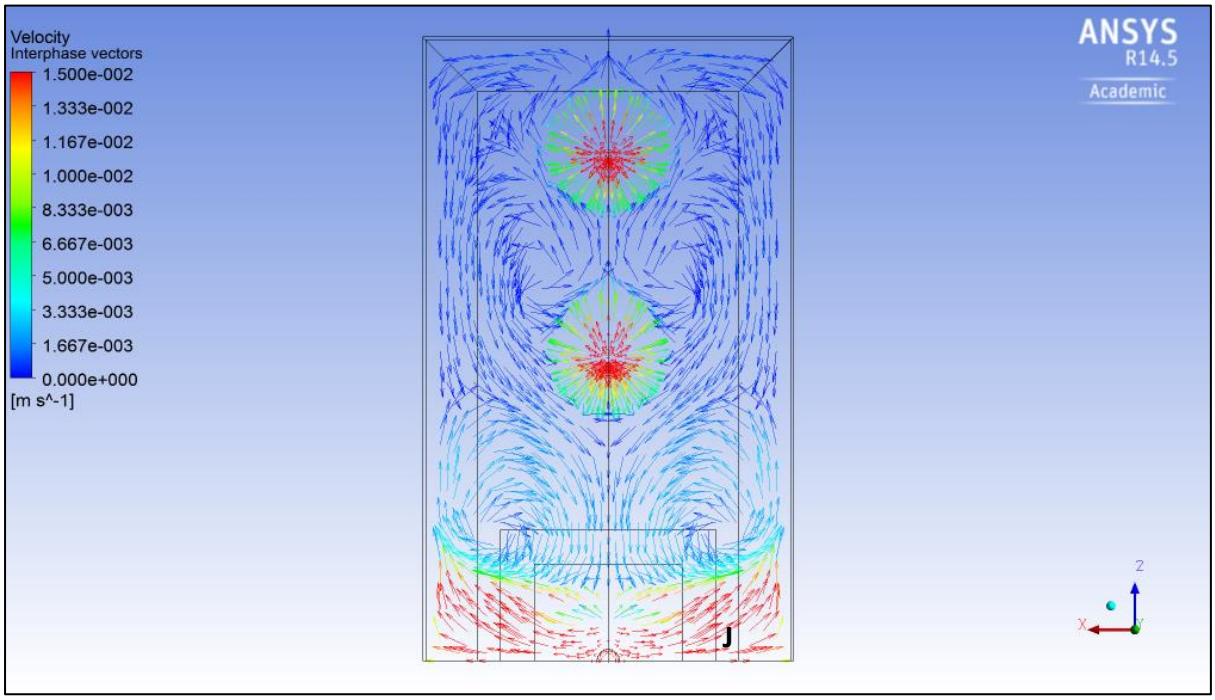

Figure 8-16 Tangential flow to the interface at a depth of 50 mm in the case of FCD.

9. APPLICATION OF RESULTS TO INDUSTRIAL TUNDISHES

In this study a numerical model which can predict tundish slag entrainment in bare tundish and a tundish with FCD was developed. Data was drawn from a water model in both the physical model and in the numerical model. However these results need to be translated back to the prototype tundish. This section outlines the implication of the result found in this study to industrial tundish performance.

9.1 Critical entrainment velocities in the prototype tundish

The critical entrainment velocities calculated in Table 2-11 are related to the water model however by using the scaling factors shown in Table 2-2 the critical slag entrainment velocities in the prototype can be calculated. Table 9-1 below shows such velocities. The lowest of these velocities is 1.90 $x10^{-1}$ m/s. Therefore for research involving the prototype tundish one would seek for tangential velocities at the interface of this magnitude to prove or disprove that slag entrainment takes place via shearing in the prototype as done in this study.

Table 9-1 Critical entrainment velocities for the water model and prototype tudish

Entrainment criteria	Water model (m/s)	Prototype (m/s)
$Ca^* = 3 \times 10^{-6}\left(\frac{\nu_1}{\nu_2}\right) + 2.8 \times 10^{-3}$	$1.34x10^{-1}$	$1.90x10^{-1}$
$Ca = \frac{V_2 \eta_2}{\sigma}$		
$\Delta V_{crit} = \sqrt[4]{4g(\rho_2 - \rho_1)\sigma\left[\frac{1}{\rho_2} + \frac{1}{\rho_1}\right]^2}$	$2.15x10^{-1}$	$3.04x10^{-1}$
$\Delta V_{crit} = \sqrt{g(\rho_2 - \rho_1)\left(\frac{H_2}{\rho_2} + \frac{H_1}{\rho_1}\right)}$	$9.44x10^{-1}$	1.34

9.2 Effect of FCD on tundish slag entrainment

Attempts were made to quantify the concentration of entrained paraffin at the strands in both the bare tundish case and tundish with FCD in the physical model. The method used involved taking volume samples at the outlets as the model was running using a calibrated cylinder and then reading the two fluid heights (water and paraffin) in the calibrated cylinder to calculate the volume fraction of entrained “slag” at the strands. This method was however not successful because the entrained “slag” height in the cylinder was smaller than the quoted accuracy of the calibrated cylinder used and thus could not be read.

However from the numerical model developed one can read the numerical concentration of entrained “slag” at the strands and thus compare the performance of a bare tundish and a tundish with a FCD. Table 9-2 shows such results.

Table 9-2 Numerically determined concentration of entrained "slag"

Entrainment criteria	Inner strand	Outer strand
Bare tundish	0.00189	0.00135
FCD	0.00234	0.00222

From Table 9-2 it can be seen that the concentration of entrained “slag” increases by 23.8 % in the inner strand and by 64.4 % in the outer strand with the use of a FCD. This indicates that the use of the FCD leads to more slag being entrained. This is despite the increase in plug flow volume fraction (68 %) and 19 % decrease in mixing volume fraction. This eludes to the need to incorporate slag entrainment when designing flow control devices.

10. CONCLUSIONS

10.1 Tundish slag behaviour

Observations made whilst the physical model was running showed that the steel-slag interface remains immobile during operation in both the bare tundish and the tundish with a flow control device case.

Sampling of entrained paraffin “slag” at a depth of 220 mm showed that the entrained tundish “slag” both in the case of bare and tundishes with a flow control devices, tended to concentrate behind the inlet shroud. The entrained “slag” concentration tends to decrease towards the tundish end walls.

10.2 Numerical model for slag entrainment and mechanisms for tundish slag entrainment

A numerical model using the Realisable k-ε model with a hexagonal mesh size of 1.4 mm and a time step of 0.125s was developed. The numerically modelled flow patterns and slag behaviour agreed strongly with those of the physical model. Thus a numerical model which can predict tundish slag behaviour was successfully developed in this study.

An analysis of numerically developed tangential velocities below the steel-slag interface (0-50 mm below the interface) showed that in both the bare tundish and tundish with a flow control device case, the tangential velocities are a factor of 10 less than the critical velocities necessary to result in in Kelvin-Helmholtz instability and any other form of macroscopic entrainment.

The existence of relatively high tangential velocity vectors only at levels greater than 10 mm below the steel-slag interface resulting in shearing of the slag layer, suggests that the slag moves across the interface via mass transfer. Then shearing caused by low tangential velocities below the interface is responsible for carrying the slag into the bulk steel phase.

Therefore it can be concluded that slag entrainment in both the bare tundish and the tundish with a flow control device, takes place via two mechanisms; mass transfer across the interface and low velocity shearing.

11. RECOMMENDATIONS

11.1 Incorporate the slag phase in future tundish studies

In this study it was shown that a physical model and a numerical study involving tundish slag can be achieved. It was further shown that incorporating a FCD resulted in an increase concentration of entrained slag at the strand outlets.

It is therefore recommended that future work involving flow control devices must include the slag layer. This will allow researchers to better design flow control devices for not only residence time improvement, but for slag entrainment too. This will help provide more complete solutions that will aid in improving tundish performance.

11.2 Validate both numerical and physical data with experimental work

Although appropriate dimensionless numbers were used in this work, and the results are therefore the same as the prototype results, it is still recommended that the concentration of slag entrained at the depths studied in this work.

Critical tangential velocities at the interface for slag entrainment in the prototype were calculated in this work. Work involving the prototype tundish should further aim at proving or disproving whether tangential at the interface of the magnitude identified in this work exist or not. Such knowledge could be used to support findings of slag entrainment mechanism made in this study.

11.3 Incorporate inclusion modelling (numerical and physical)

In this study the concept of tundish modelling has been taken a step further by including a slag phase, however there is still scope to study the tundish further by including inclusion modelling in the already existing tundish slag model.

Such work will help researchers to gain a complete understanding of how the tundish behaves under the influence of a flow control device. The size and properties of the particles to be used will have to satisfy the requirements of dimensionless number similarities.

REFERENCES

Ahuja, R. & Sahai Y. 1986, "Fluid Flow and Mixing of Melt in Steel making Tundishes", *Ironmaking & Steelmaking,* vol. 13, pp. 241-247.

ANSYS 2011, *ANSYS FLUENT Theory Guide Version 14*, Notes edn, ANSYS, Southpointe.

Bakker, A. 2008, February 3, 2008-last update*, Computational Fluid Dyanamics* [Homepage of Fluent Inc.], [Online]. Available: http://www.bakker.org/ [2014, April/27].

Chattopadhyay, K., Isac, M. & Guthri, R.I.L. 2010, "Physical and Mathematical Modelling of Steelmaking Tundish Operations: A Review of the Last Decade (1999–2009)", *ISIJ International,* vol. 50, no. 3, pp. 331-348.

Cloete, J.H. 2014, *Flow Analysis of a Four-strand Steelmaking Tundish using Physical and Numerical Modelling*, Masters Thesis edn, University of Stellenbosch, South Africa.

Hagemann, R., Rüdiger, S., Heller, H.P. & Scheller, P.R. 2013, "Model Investigations on the Stability of the Steel-Slag Interface in Continuous-Casting Process", *Metallurgical and Materials Transactions,* vol. 44, no. 1, pp. 80-90.

Harman, J.M. & Cramb, A.W. 1996, "A Study on the Effect of Fluid Physical Properties on Droplet Emulsification", *Steelmaking Conference Proceedings,* vol. 79, pp. 773-784.

Hattingh, P.R. 2009, *Physical Modelling of a Peirce-Smith Converter*, Final Year Thesis edn, University of Stellebosch, South Africa.

He, Y. & Sahai, Y. 1987, "The Effect of Tundish Wall Inclination on the Fluid Flow and Mixing: A Model Study", *Metallurgical Transactions,* vol. 18, no. 2, pp. 81-92.

Hibbeler, L.C. & Thomas, B.G. 2010, "Investigation of Mold Flux Entrainment in CC Molds Due to Shear Layer Instability", *AISTech 2010 Steelmaking Conference Proceedings,* vol. 1, pp. 1215-1230.

Iguchi, M., Yoshida, J., Shimizu, T. & Mizuno, Y. 2000, "Model Study on Entrapment of Mold Powder into Molten Steel", *ISIJ International,* vol. 40, no. 7, pp. 658-691.

Jha, P.K., Dash, S.K. & Kumar, S., 2001, "Fluid Flow and Mixing in a Six Strand Billet Caster Tundish: A Parametric Study", *ISIJ International,* vol. 41, no. 12, pp. 1437-1446.

Jha, P.K., Rao, P.S. & Dewan, A. 2008, "Effect of Height and Position of Dams on Inclusion Removal in a Six Strand Tundish", *ISIJ International,* vol. 48, no. 2, pp. 154-160.

Johansen, E.M. 1924, "The Interfacial Tension between Petroleum Products and Water", *Industrial & Engineering Chemistry,* vol. 16, no. 2, pp. 132-135.

Joo, S. & Guthrite, R.I.L. 1991, "Heat Flow and Inclusion Behaviour in a Tundish for Slab Casting ", *Can Metall. Q,* vol. 30, pp. 261-269.

Krishnapisharody, K. & Irons, G.A. 2008, "An Extended Model for Slag Eye Size in Ladle Metallurgy", *ISIJ International,* vol. 48, no. 12, pp. 1807-1809.

Kumar, A., Koria, S.C. & Mazumdar, D. 2007, "Basis for Systematic Hydrodynamic Analysis of a Multi-strand Tundish ", *ISIJ International,* vol. 47, no. 11, pp. 1618-1624.

Kumar, A., Mazumdar, D. & Koria, S.C. 2008, "Modeling of Fluid Flow and Residence Time Distribution in a Four-strand Tundish for Enhancing Inclusion Removal", *ISIJ International,* vol. 48, pp. 38-47.

Luo-fang, G., Yao, W., Hong, L. & Hai-tao, L. 2013, "Floating Properties of Agglomerated Inclusion in Liquid Steel", *Journal of Iron and Steel Research, International,* vol. 20, no. 7, pp. 35-39.

Mazumdar, D. & Guthri, R.I.L. 1999, "The Physical and Mathematical Tundish Systems ", *ISIJ International,* vol. 39, no. 6, pp. 524-547.

Mills, K. 2011, "The Estimation of Slag Properties", *Southern African Pyrometallurgy 2011,* pp. 1-52.

Milne-Thomson, L.M. 1968, *Theoretical Hydrodyanamics,* 5e edn, Macmillan Press, London.

Nagaoka, T., Radot, J.P., Reynolds, T., Vaterlaus, A. & Wolf, M. 1986, "Steelmaking Conference Proceedings", *ISS-AIME,* vol. 69, pp. 799-810.

Reilly, C., Green, N.R., Jolly, M.R. & Gebelin, J. 2013, "The Modelling of Oxide Film Entrainment in Casting Systems Using Computational Modelling", *Applied Mathematical Modelling,* vol. 37, pp. 8451-8466.

Sahai, Y. & Ahuja, R. 1986, "Fluid Flow and Mixing of Melt in Steelmaking Tundishes", *Ironmaking and Steelmaking,* vol. 13, no. 5, pp. 241-247.

Sahai, Y. & Burval, M.D. 1992, "Electric Furnace Conference Proceedings ", *I.S.S Publication,* vol. 50, pp. 469-474.

Sahai, Y. & Emi, T. 2008, *Tundish Technology for Clean Steel Production,* World Scientific Publishing Co. Pte. Ltd, Singapore.

Sahai, Y. & Emi, T. 1996, "Melt Flow Characterization in Continuous Casting Tundishes", *ISIJ International,* vol. 36, no. 6, pp. 667-672.

Schade, J., O'Malley, R.J., Kemeny, F., Sahai, Y. & Zacharias, D. 2003, "Chapter 13: Tundish Operations" in *The Making, Shaping and Treating of Steel*, ed. A.W. Cramb, 11th edn, The AISE Foundation, Pittsburgh, PA, pp. 1-2.

Senguttuvan, A. & Irons, G.A. 2013, "Model Studies on Slag Metal Entrainment in Gas-Stirred Laddles", *AIST Transactions,* vol. 11, no. 1, pp. 230.

Sheng, D.Y., Kim, C.S. & Yon, J.K., Hsiao, T.C. 1998, *ISIJ International,* vol. 38, pp. 843.

Solhed, H. & Jonsson, L. 2003, "An Investigation of Slag Floatation and Entrapment in a Continuous-casting Tundish using Fluid-flow Simulations, Sampling and Physical Metallurgy ", *Scandinavian Journal of Metallurgy,* vol. 32, no. 1, pp. 15-30.

Solhed, H., Jonsson, L. & Jönsson, P. 2008, "Modelling of Steel/Slag Interface in a Continuous Casting Tundishe", *steel research international,* vol. 79, no. 5, pp. 348-357.

Tapia, V.H., Morales, R.D., Camacho, J. & Lugo, G. 1996, "The Influence of the Tundish Powder on Steel Cleanliness and Nozzle Clogging" in *79th Steelmaking Conference proceedings : volume 79, Pittsburgh meeting, March 24 - 27, 1996*, ed. Steelmaking Division, 79th edn, Iron and Steel Soc, Warrendale, Pa, pp. 539.

Tripathi, A. & Ajmani, S.K. 2011, "Effect of Shape and Flow Control Devices on the Fluid Flow Characteristics in Three Different Industrial Six Strand Billet Caster Tundish ", *ISIJ International,* vol. 51, no. 10, pp. 1647–1656.

Tripathi, A. & Ajmani, S.K., 2005, "Numerical Investigation of Fluid Flow Phenomenon in a Curved Shape Tundish of Billet Caster ", *ISIJ International,* vol. 45, no. 11, pp. 1616-1625.

World Steel Association 2015, 28/05/15-last update*, World Steel Association* [Homepage of worldsteel], [Online]. Available: www.worldsteel.org [2015, 05/28].

Zhang, L. & Thomas, B. 2003a, "Inclusion in Continous Casting of Steel", *XXIV National Steelmaking Symposium, Morelia, Mich, Mexico,* pp. 138-183.

Zhang, L. & Thomas, B. 2003b, "State of the Art in Evaluation and Control of steel Cleanliness", *ISIJ International,* vol. 43, no. 3, pp. 271-291.

APPENDIX A: NOMENCLATURE AND ACRONYMYS

A 1: Symbols and units

SYMBOL	MEANING	UNITS
A	Cross sectional area	m^2
a_i	Volume fraction of the i-th phase in the concerned cell volume	-
C	concentration	g/L
$\bar{\theta}_c$	Dimensionless flow time until a cut off time	-
C_1	Constant	-
C_2	Constant	-
Ca	Capillary number	-
Ca*	Critical capillary number	-
c_i	Dimensionless concentration at a specific dimensionless time	-
C_η	Constant	-
d	bubble diameter	m
De	Extent of dispersion	-
D_i	Molecular diffusion of tracer in main fluid	m/s
F_b	Force acting on a fluid element	N
g	Gravity	m/s^2
G_k	Rate of generation of kinetic energy per unit mass	J/kg
h	slag/ melt height	m
I	Turbulence intensity	-
J_i	Effective mass transfer	$kg/m^2.s$
k	Turbulence kinetic energy	J
L_m	Characteristic length of the model	m
L_p	Characteristic length of the model	m
m_{ij}	Mass transfer rate of i-th phase into the j-th phase	$kg/m^2.s$
η	Molecular viscosity	kg/m.s
$N_{Fr,m}$	Model's Froude number	-
$N_{Fr,p}$	Prototype's Froude number	-
$N_{RE,m}$	Model's Reynolds number	-
$N_{RE,p}$	Prototype's Reynolds number	-
η_t	Turbulent viscosity	kg/m.s
P	Pressure	Pa
Q	Total flow through entire vessel	m^3/s
Qa	Flow through active part of a vessel	m^3/s
R_i	Rate of production of the tracer by reaction	$kg/m^2.s$
Sa_i	Rate of generation of the i-th phase	kg/m2.s
Sc_t	Turbulent Schmidt Number	-
S_i	Rate of production of the tracer via addition	$kg/m^2.s$
V	Volume of vessel	m^3
V_i'	Fluctuating velocity component	m/s

V_d	Dead volume	m^3
V_m	Velocity of fluid or inclusion in the model	m/s
V_p	Velocity of fluid or inclusion in the prototype	m/s
$\vec{V}$, v_i	Instantaneous velocity of the fluid in the x-y-z direction	m/s
We	Webber number	-
Y_i	Mass fraction of the tracer in the calculation domain	-
θ	Dimensionless flow time	-
θ_{max}	Largest angle in the hexahedral	^{o}
θ_{min}	Dimensionless time at which first sign of tracer occurs	-
θ_{min}	Smallest angle in the hexahedral	^{o}
θ_{peak}	Dimensionless time at which maximum tracer concentration can be seen at the outlet	-
λ	Scale factor	-
μ	Kinematic viscosity	m^2/s
μ_t	Effective turbulent viscosity	kg/m.s
ρ	Density	kg/m^3
σ	Interfacial tension	N/m
σ_k	Constant	-
σ_ε	Constant	-
τ_m	Mean residence time	s
τ_p	Plug flow volume	m^3
$\bar{v_t}$	Average velocity of the fluid in the x-y-z direction	m/s

A 2: Acronyms

Acronym	**Full version**
BOF	Basic Oxide Furnace
CFD	Computational Fluid Dynamics
Dph_c	Dispersed phase hold up
EAF	Electric Arc Furnace
LCAK	Low Carbon Alumina Killed
FCD	Flow Control Device
MUSCL	Monotone Upstream-Centred Schemes for Conservation Laws
PRESTO!	Pressure Staggering Option
QUICK	Quadratic Upwind Interpolation for Convective Kinetics
VOF	Volume of Fluid

APPENDIX B: ENTRAINED “SLAG” RAW DATA

B 1: Entrained paraffin concentration in bare tundish

Grid No.	Run: paraffin volume fraction					Average volume paraffin
	1	2	3	4	5	
1	0.0206	0.0187	0.0187	0.0187	0.0215	0.0196
2	0.0196	0.0196	0.0187	0.0187	0.0187	0.0191
3	0.0206	0.0225	0.0206	0.0187	0.0187	0.0202
4	0.0215	0.0206	0.0206	0.0196	0.0187	0.0202
5	0.0187	0.0187	0.0187	0.0187	0.0206	0.0191
6	0.0196	0.0215	0.0187	0.0196	0.0177	0.0194
7	0.0159	0.0187	0.0159	0.0159	0.0168	0.0166
8	0.0196	0.0177	0.0187	0.0206	0.0187	0.0191
9	0.0196	0.0196	0.0177	0.0206	0.0187	0.0193
10	0.0215	0.0187	0.0187	0.0177	0.0187	0.0191
11	0.0206	0.0168	0.0206	0.0196	0.0177	0.0191
12	0.0149	0.0159	0.0159	0.0187	0.0159	0.0162
13	0.0177	0.0159	0.0159	0.0140	0.0159	0.0159
14	0.0196	0.0187	0.0177	0.0187	0.0206	0.0191
15	0.0225	0.0187	0.0187	0.0187	0.0196	0.0196
16	0.0215	0.0187	0.0177	0.0196	0.0187	0.0193
17	0.0187	0.0196	0.0187	0.0187	0.0206	0.0193
18	0.0149	0.0168	0.0149	0.0168	0.0159	0.0159
19	0.0168	0.0140	0.0140	0.0159	0.0159	0.0153
20	0.0168	0.0168	0.0168	0.0149	0.0168	0.0164
21	0.0149	0.0168	0.0168	0.0177	0.0149	0.0162
22	0.0159	0.0149	0.0159	0.0168	0.0159	0.0159
23	0.0168	0.0149	0.0168	0.0177	0.0159	0.0164
24	0.0140	0.0159	0.0168	0.0149	0.0140	0.0151
25	0.0121	0.0121	0.0140	0.0140	0.0130	0.0130
26	0.0168	0.0121	0.0149	0.0168	0.0159	0.0153
27	0.0140	0.0149	0.0130	0.0159	0.0159	0.0147
28	0.0159	0.0140	0.0130	0.0140	0.0159	0.0145
29	0.0159	0.0177	0.0159	0.0159	0.0140	0.0159
30	0.0149	0.0121	0.0130	0.0149	0.0140	0.0138
31	0.0159	0.0159	0.0111	0.0121	0.0102	0.0130
32	0.0102	0.0121	0.0130	0.0140	0.0130	0.0125
33	0.0130	0.0111	0.0111	0.0130	0.0130	0.0123
34	0.0111	0.0111	0.0111	0.0130	0.0121	0.0117
35	0.0121	0.0149	0.0140	0.0111	0.0140	0.0132
36	0.0140	0.0111	0.0140	0.0130	0.0130	0.0130
37	0.0121	0.0121	0.0140	0.0130	0.0121	0.0126
38	0.0130	0.0140	0.0130	0.0121	0.0111	0.0126
39	0.0149	0.0140	0.0111	0.0140	0.0121	0.0132
40	0.0130	0.0130	0.0140	0.0140	0.0111	0.0130
41	0.0121	0.0130	0.0121	0.0111	0.0102	0.0117
42	0.0111	0.0121	0.0130	0.0102	0.0111	0.0115

B 2: Entrained paraffin concentration in tundish with FCD

Grid No.	Run: paraffin volume fraction					Average volume paraffin
	1	2	3	4	5	
1	0.0177	0.0177	0.0177	0.0168	0.0187	0.0177
2	0.0187	0.0177	0.0177	0.0187	0.0187	0.0183
3	0.0187	0.0168	0.0177	0.0177	0.0196	0.0181
4	0.0196	0.0187	0.0196	0.0177	0.0187	0.0189
5	0.0196	0.0168	0.0177	0.0187	0.0177	0.0181
6	0.0159	0.0168	0.0177	0.0177	0.0187	0.0174
7	0.0177	0.0168	0.0187	0.0159	0.0177	0.0174
8	0.0168	0.0187	0.0196	0.0215	0.0187	0.0191
9	0.0177	0.0168	0.0187	0.0177	0.0159	0.0174
10	0.0177	0.0168	0.0177	0.0168	0.0177	0.0174
11	0.0177	0.0215	0.0187	0.0187	0.0196	0.0193
12	0.0168	0.0159	0.0168	0.0168	0.0177	0.0168
13	0.0159	0.0177	0.0177	0.0168	0.0187	0.0174
14	0.0215	0.0196	0.0168	0.0187	0.0187	0.0191
15	0.0177	0.0177	0.0159	0.0168	0.0168	0.0170
16	0.0187	0.0159	0.0168	0.0159	0.0177	0.0170
17	0.0215	0.0187	0.0187	0.0187	0.0177	0.0191
18	0.0149	0.0159	0.0168	0.0159	0.0168	0.0160
19	0.0168	0.0159	0.0159	0.0159	0.0149	0.0159
20	0.0187	0.0168	0.0168	0.0168	0.0159	0.0170
21	0.0168	0.0168	0.0177	0.0168	0.0177	0.0172
22	0.0177	0.0159	0.0159	0.0168	0.0159	0.0164
23	0.0168	0.0168	0.0177	0.0159	0.0177	0.0170
24	0.0149	0.0149	0.0168	0.0168	0.0159	0.0159
25	0.0140	0.0159	0.0159	0.0149	0.0159	0.0153
26	0.0159	0.0159	0.0149	0.0159	0.0159	0.0157
27	0.0149	0.0159	0.0149	0.0149	0.0168	0.0155
28	0.0149	0.0140	0.0159	0.0168	0.0159	0.0155
29	0.0149	0.0159	0.0140	0.0168	0.0168	0.0157
30	0.0149	0.0130	0.0140	0.0159	0.0140	0.0143
31	0.0130	0.0140	0.0140	0.0149	0.0140	0.0140
32	0.0149	0.0149	0.0159	0.0130	0.0130	0.0143
33	0.0149	0.0140	0.0130	0.0140	0.0140	0.0140
34	0.0140	0.0121	0.0130	0.0140	0.0159	0.0138
35	0.0130	0.0130	0.0111	0.0149	0.0140	0.0132
36	0.0140	0.0121	0.0130	0.0121	0.0140	0.0130
37	0.0140	0.0149	0.0121	0.0140	0.0149	0.0140
38	0.0130	0.0130	0.0121	0.0140	0.0149	0.0134
39	0.0130	0.0121	0.0121	0.0130	0.0140	0.0128
40	0.0121	0.0130	0.0111	0.0140	0.0140	0.0128
41	0.0111	0.0130	0.0140	0.0149	0.0130	0.0132
42	0.0111	0.0140	0.0140	0.0130	0.0121	0.0128